

PIEZOELECTRIC ULTRAFINE POLYMER AND CERAMIC FIBERS
BY ELECTROSPINNING:
PROCESS DEVELOPMENT AND CHARACTERIZATION

by
ONUR SİNAN YÖRDEM

Submitted to the Graduate School of Engineering and Natural Sciences
in partial fulfillment of
the requirements for the degree of
Master of Science

Sabancı University
Summer 2006

PIEZOELECTRIC ULTRAFINE POLYMER AND CERAMIC FIBERS
BY ELECTROSPINING:
PROCESS DEVELOPMENT AND CHARACTERIZATION

APPROVED BY

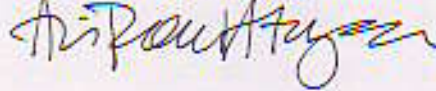
Assist. Prof. Dr. Melih Papila
(Thesis Advisor)



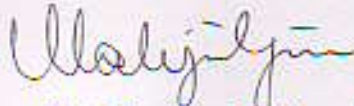
Prof. Dr. Mehmet A. Akgün



Prof. Dr. Ali Rana Atılgan



Assoc. Prof. Dr. Mehmet Ali Gülgün



Assoc. Prof. Dr. Yusuf Z. Menceloğlu



DATE OF APPROVAL: 13/07/2006

© Onur Sinan Yördem 2006

All Rights Reserved

PIEZOELECTRIC ULTRAFINE POLYMER AND CERAMIC FIBERS
BY ELECTROSPINNING:
PROCESS DEVELOPMENT AND CHARACTERIZATION

Onur Sinan YÖRDEM

Materials Science and Engineering, MSc Thesis, 2006

Thesis Supervisor: Assist. Prof. Dr. Melih PAPİLA

Keywords: Electrospinning, Solution Casting, PVDF, ZnO, Fiber, Design of Experiments, Response Surface Methodology, Piezoelectric

Abstract

Piezoelectric polymer and ceramic films and fiber mats that may be considered for actuator and sensor needs were fabricated. Solution casting and electrospinning were utilized for Poly(vinylidene fluoride) (PVDF) films and fiber mats, respectively, while zinc oxide (ZnO) fiber mats were fabricated by electrospinning process followed by calcination. Morphology, crystalline structure and mechanical properties of the piezoelectric films and fiber mats were examined and characterized for experiment-based process optimization.

Traditional solution casting process produces uniform PVDF films yet with non-polar crystallinity. Stretching of the solution cast films were carried out to increase the polar crystal phase of PVDF. Stretched and un-stretched PVDF films were characterized according to their polar crystallite contents, and stretching was shown to be vital for β -phase formation in favor of piezoelectricity.

Electrospinning process produces mats of ultrafine fibers with diameter ranging from a hundred nanometers to a couple of micrometers, by applying an electrical force to polymer solution. The effects of solvent type, solvent mixture together with applied voltage and collector distance were investigated leading to process parameter ranges to produce planar mats composed of uniform fibers only. All of the parameters were found to have vital roles in the fabrication of fiber mats regarding their morphology and applicability without self-folding and fiber uniformity. In addition, crystallinity, morphology, mechanical property and potential piezoelectric effect of solution cast and electrospun films were analyzed and compared. Electrospun fiber mats were found to be advantageous as in-situ β -phase formation was observed.

Nano-scale zinc oxide fibers were also produced by electrospinning, but followed by calcination. Processing conditions such as solution content and heat treatment schemes were optimized in order to obtain uniform ZnO nanofibers. Zinc concentration and the substrate that the sample is placed on were found to be significant towards the uniformity and continuity of the ceramic fibers. Heating rate during calcination was also shown to be effective in fiber morphology and geometry. Fibers of ZnO with ~ 140 nm diameter were produced. In addition, micron-scale ZnO whiskers and rods were also formed during the calcination process.

ELEKTRODOKUMA YÖNTEMİ İLE ÜRETİLEN PİEZOELEKTRİK
POLİMER VE SERAMİK FİBERLER:
SÜREÇ GELİŞTİRME VE KARAKTERİZASYON

Onur Sinan YÖRDEM

Malzeme Bilimi ve Mühendisliği, Yüksek Lisans Tezi, 2006

Tez Danışmanı: Yrd. Doç. Melih PAPİLA

Anahtar Kelimeler: Elektrodokuma, Çözelti Döküm, PVDF, Çinko Oksit, Fiber,
Deneysel Tasarım, Süreç Eniyileme, Piezoelektrik

ÖZET

Eyleyici ve duyurga uygulamalarında kullanılacak piezoelektrik polimer ve seramik bazlı film ve fiber ağlar üretilmiştir. Poly(vinyldene fluoride) (PVDF) filmleri ve fiber ağları, sırasıyla, çözelti dökümü ve elektrodokuma teknikleri ile üretilirken, çinko oksit fiber ağları elektrodokuma tekniğini takiben yapılan sinterleme işlemi ile üretilmiştir. Üretilen filmlerin ve fiber ağlarının yüzey morfolojileri, kristal yapıları ve mukavemetleri incelenmiş, ve deneysel tasarım tekniği kullanılarak karakterize edilmiştir.

Sıkça kullanılan çözelti dökümü tekniği, muntazam ancak kutbi olmayan kristallerden oluşan PVDF filmleri üretmektedir. Filmleri uzatarak kutbi kristallerin miktarı arttırılmıştır. Uzatma işlemine tabi olan ve hiç uzatılmayan filmler ayrı ayrı karakterize edilmiş ve kutbi kristal yapıları incelenmiştir. Uzatma işleminin piezoelektrik etkiyi arttıran kutbi kristal faz, β -faz, miktarını arttırdığı görülmüştür.

Elektrodokuma metodu ile polimer çözeltilisine verilen yüksek voltaj sayesinde, nano-ölçekten mikro-ölçeğe kadar uzanan geniş bir çap spektrumunda fiberler üretilmiştir. Çözücü tipi, çözücü karışım oranı, uygulanan voltaj ve toplayıcı yüzey uzaklığının, fiber ağı üretimi ve fiber kalitesine etkileri incelenmiştir. Bu etkenlerin fiber ağı yüzey morfolojilerinde ve uygulanabilirliğinde önemli ölçüde etkili olduğu görülmüştür. Üretilen fiber ağlarının kristal yapıları, morfolojileri ve mukavemetleri çözelti dökümü tekniği ile üretilen filmlerle karşılaştırılmıştır. Elektrodokuma süreci ile üretilen fiber ağlarının β -fazı oluşumunda faydalı olduğu saptanmıştır.

İlave olarak, elektrodokuma tekniğini takip eden sinterleme süreci ile nano-ölçekte çinko oksit fiberleri üretilmiştir. Muntazam fiber üretimi için çözelti konsantrasyonu ve ısıtım işlem süreci etkenleri eniyileme çalışması yapılmıştır. Çinko konsantrasyonunun ve sinterleme yapılan zemin pürüzlülüğünün seramik fiber kalitesinde ve sürekliliğinde etkisi olduğu saptanmıştır. Sinterleme sürecinde uygulanan ısıtım işleminin fiber morfolojisi ve geometrisinde etkili olduğu görülmüştür. Ortalama 140 nanometre çapında çinko oksit fiberler üretilmiştir. Buna ek olarak, micron-ölçekte çinko oksit iğneciklerinin ve çubuklarının oluştuğu bulunmuştur.

Aileme...

ACKNOWLEDGEMENTS

I would like to express my veneration, appreciation and greatest admiration to my Thesis Advisor, Dr. Melih Papila. I would not be able to accomplish any bit of this study without his never-ending countenance and endorsement. I have always been motivated by his enthusiasm and ingenious remarks through out my work. His willingness to share his deep knowledge and invaluable time helped me develop myself both professionally and personally.

I would also like to thank Dr. Yusuf Mencelođlu for his endless and invaluable efforts to teach me science of polymers. I really appreciate every support he ensured through my thesis and every single answer he gave to my endless chemistry questions.

I must express my gratitude to Dr. Mehmet Ali Glgn for motivating me since my sophomore year towards studying materials science. He broadened my professional perspective and helped visioning my career.

I would also like to thank the members of my advisory committee, Dr. Ali Rana Atılgan and Dr. Mehmet A. Akgn for reviewing my Masters work and providing me their invaluable comments.

I also express my gratitude to TBTAK for granting our project: (Grant Number:105M031). The materials and the set-ups used through out the study were provided by this grant.

I should also thank to Baran İnceođlu and his colleagues in Rotopak-ALCAN Packaging for sharing their time with me at the tensile testing machine.

.I must express my deepest sympathies to my lab-colleagues Burak Birkan and Funda İnceođlu. I appreciate their answers to every one of my meaningless chemistry questions. I learned a lot from both you.

I also appreciate every help of the Papila Research Team: Erdem Öđüt, Mert Güllerođlu, Cihan Pirimođlu, Ceren Özaydın, and Özlem Kocabaş.

I would like to express my feelings for the “The Synergie Group”: Kerem Gören, Osman Burak Okan, Irmak Sirer, Eren Şimşek, and Deniz Turgut. These two years would not be so fun without you guys. I really feel that I am lucky to knowing each one of you. No second of these two years would have a meaning without you. Thanks for everything.

To my other half, Burcu... We have been the two separate pieces of the whole... You were my inspiration and always will be. I can only hope that we would share every moment of our lives together.

Finally, this work would not be completed without the inspiration and motivation that my family gave to me. I express my deepest esteem to my family for supporting the every step I take through my ideals. My only hope is to share every blissful moment of my life with you. *Last, I really appreciate every single facility you provided Babacıđım, nothing is a whole as it would be with you...*

TABLE OF CONTENTS

ABSTRACT	iv
ÖZET	vi
ACKNOWLEDGEMENTS	ix
TABLE OF CONTENTS	xi
LIST OF TABLES	xiv
LIST OF FIGURES	xvi
LIST OF SYMBOLS AND ABBREVIATIONS.....	xx
1. INTRODUCTION	1
1.1 Focus	1
1.2 Approach.....	2
1.3 Objectives of the Study.....	3
2. LITERATURE SURVEY.....	4
2.1 Poly(vinylidene fluoride): A Sensor and An Actuator	4
2.2 Zinc Oxide: A Promising Electronic Material.....	10
2.3 Electroactive Composite Materials.....	12
3. PIEZOELECTRIC MATERIALS SYSTEMS OF INTEREST	14
3.1 Piezoelectric Polymer: PVDF	14
3.2 Piezoelectric Ceramic: ZnO.....	17
4. PVDF FILMS	20
4.1 Process: Polymer Film Production by Solution Casting.....	20
4.2 Characterization Tools.....	21
4.3 Results and Discussions.....	23
4.3.1 Pristine Solution Cast PVDF Films	23
4.3.1.1 FT-IR and NMR Measurements.....	23
4.3.1.2 XRD Measurements	27
4.3.1.3 DSC Measurements.....	29
4.3.1.4 Mechanical Properties	31

4.3.2	Stretched Solution Cast Films.....	33
4.3.2.1	XRD Measurements	33
4.3.2.2	DSC Measurements.....	35
4.3.2.3	Mechanical Characterization.....	37
4.3.3	Comparison Between Stretched and Un-stretched Solution Cast PVDF Films	39
4.3.3.1	XRD Measurements	40
4.3.3.2	DSC Measurements.....	40
4.3.3.3	Mechanical Strength.....	41
5.	PVDF FIBER MATS.....	43
5.1	Process: Electrospinning of Polymer Solutions.....	43
5.2	Process Optimization via Response Surface Methodology	45
5.2.1	Linear Regression	45
5.2.2	Method of Least Squares	47
5.2.3	Experimental Design.....	47
5.3	Characterization Tools.....	51
5.4	Results and Discussions.....	51
5.4.1	Design of Experiments for Applicability.....	51
5.4.1.1	Results for the Visual Applicability Test.....	56
5.4.2	Prediction of Fiber Diameter via Response Surface Methodology	58
5.4.2.1	Prediction of experiment settings for targeted response	58
5.4.2.2	Results for the Fiber Diameter	59
5.4.3	Characterization of As-Spun PVDF Mats	68
5.4.3.1	XRD.....	68
5.4.3.2	DSC Measurements.....	70
5.4.3.3	Mechanical Tests.....	72
5.4.4	Characterization of Stretched Electrospun Mats	73
5.4.4.1	XRD Results.....	73
5.4.4.2	DSC Results	74
6.	ZINC OXIDE FIBER MATS	76
6.1	Process: Electrospinning of Organo-Metallic Precursor Solutions	76
6.2	Characterization Tools.....	79
6.3	Results and Discussions.....	80
6.3.1	Precursor Solution Concentration.....	80

6.3.2	Calcined Zinc Oxide Mats	80
6.3.2.1	EDXS Measurements	84
6.3.2.2	XRD Measurements	85
6.3.3	ZnO Whisker and Rod Formation	85
7.	SUGGESTIONS AND FUTURE WORK.....	88
8.	CONCLUDING REMARKS.....	90
	REFERENCES.....	92
	APPENDICES.....	101
	Appendix A: Preparatory Information on Electro-mechanical Activity and Electroactive Materials	102
	Appendix B: Response Surface Methodology	111
	Appendix C: Effects of Electrospinning Parameters on Polyacrylonitrile Nanofiber Diameter: An Investigation by Response Surface Methodology	Error!

Bookmark not defined.

LIST OF TABLES

Table 1 Physical properties of zinc oxide structures. Courtesy of Fan et al. [59]	19
Table 2 Casting temperature and duration exerted on the PVDF solution	21
Table 3 DSC results	30
Table 4 Tensile test results of the pristine solution cast PVDF films.....	31
Table 5 DSC data for the stretched solution cast PVDF films.	35
Table 6 Mechanical properties of stretched solution cast PVDF films.	37
Table 7 Experiment points in the region of interest.....	52
Table 8 3-level factorial design constructed for the electrospinning of PVDF	55
Table 9 Fiber diameter measurements obtained from the DMF Only samples. As given in the graph, some samples do not have fiber structures hence it is not feasible to count them as fiber data.	60
Table 10 Fiber diameter measurements obtained from the Acetone DMF mixture with a ratio of 0.25. These sample also included some non-fiber structures, yet, measurement could be obtained.....	61
Table 11 Fiber diameter measurements obtained from the Acetone and DMF with 50% mixing ratio.....	62
Table 12 Statistical results for the quadratic fit on the 25% Acetone/DMF sample.	64
Table 13 Statistical results for the quadratic fit on the 50% Acetone/DMF sample.	64
Table 14 Residuals and percent errors in the quadratic model for the 25% sample.....	65
Table 15 Residuals and percent errors of the 50% Acetone/DMF solution sample.	65
Table 16 Parameter estimates and p-value statistics for the quadratic model fitted over 9 data.....	68
Table 17 Tensile test results of the electrospun samples obtained at the 50% DMF/Acetone experimental design space.	72
Table 18 Precursor solution and calcination parameters that were employed for the fabrication of ZnO fibers	77

Table 19 Comparison of properties of three active materials EAPs, SMAs, EACs (adapted from [6]).....	104
Table 20 Examples of piezoelectric devices and their applications (adapted and extended from [105] and [113]).....	107

LIST OF FIGURES

Figure 1 Schematic representation of crystallites in amorphous phase of PVDF. (a) melt cast film (b) mechanically stretched melt cast film (c) poled melt cast film. Courtesy of NASA [28].	6
Figure 2 Nanostructures developed from ZnO. Courtesy of Wang et al. [51]	11
Figure 3 α -Phase structural conformation, adapted from [29]	15
Figure 4 Space-filling model of the α -phase PVDF, adapted from [29]	16
Figure 5 β -Phase structural conformation, adapted from [29]	16
Figure 6 Space-filling model of the β -phase PVDF, adapted from [29]	17
Figure 7 Zinc oxide crystal wurtzite structure	18
Figure 8 MTS Synergie 200 tensile testing apparatus with pneumatic rubber clamps (In courtesy of Rotopak-Alcan Packaging)	22
Figure 9 Homemade stretching set-up to elongate films for orienting the chains and thus dipoles to enhance polarity.	23
Figure 10 β -phase crystallinity modification due to a change in temperature (a) and duration (b).	25
Figure 11 NMR measurement obtained from a stack of different temperatures: 40-45-55-65-70 ⁰ C. One can observe the shift of the spectrum moving towards left.	26
Figure 12 A deeper investigation between 93 - 95 ppm reveals a change in the curve, that is, the curve slants left as the temperature is increased.	27
Figure 13 XRD data representing the crystalline peaks of the PVDF films.	28
Figure 14 XRD data representing the crystalline peaks of the PVDF films between the 2θ values of 10 – 30.	29
Figure 15 Melting point and % crystallinity values obtained from the DSC measurements.	30
Figure 16 Ultimate Stress and the Elastic Modulus of the un-stretched solution cast films were plotted versus the process variable, casting temperature.	32

Figure 17 Correlation between percent crystallinity and Youngs modulus of the un-stretched solution cast films.....	33
Figure 18 XRD Results ofthe streched solution cast films.....	34
Figure 19 XRD data for the stretched solution cast films in the 2θ region 10 - 30.....	34
Figure 20 DSC results of the stretched solution cast films. Melting point values are lower than that of the pristine samples.	36
Figure 21 Melting point and percent crystallinity values after mechanically stretching the cast films.....	37
Figure 22 Ultimate stress observed on the stretched solution cast PVDF films.....	38
Figure 23 Relation between percent crystallinity and the ultimate stress exerted on the stretched films is plotted.....	39
Figure 24 Comparison between stretched and un-stretched solution cast films.....	40
Figure 25 Comparison of DSC results of stretched and un-stretched solution cast films.....	41
Figure 26 A representative tensile strength graphs to monitor modification through stretching the samples.....	42
Figure 27 Schematic representation of the computer controlled electrospinning setup. Up to 100 syringe pumps can be independently controlled via one unit.....	44
Figure 28 Linear regression fitted on the 17 sample data.....	46
Figure 29 Schematic representation of an experimental process. Adapted from [100]	48
Figure 30 2 Level Factorial design for the change in fiber diameter. Voltage and Concentration are the two different factors experimented at two levels.....	49
Figure 31 A representative plot of an RSM example. Baking temperature and duration are the factors affecting the adhesion (response) of the material.....	50
Figure 32 Eperimental design region for three different solution ratios. 9 experiments were conducted at each solution mixture design space.....	52
Figure 33 Two-variable 3-level factorial design. Applied voltage and the collector distance are the parameters of interest. This factorial design is applied at all solfvent mixing ratios.....	55
Figure 34 Image electrospun samples with non-applicable (left) and applicable mat morphologies (right).....	57
Figure 35 SEM images of the non-applicable (left) and applicable fiber mats (right)...	57
Figure 36 Fibers spun on an MAV skeletal strusture made up of Carbon/Epoxy composite. The polymer fibers in micrometer scale are spun on this wing and	

perfectly kept the skeleton in shape (wing skeleton was adopted from Ifju et al. [103]).	58
Figure 37 DMF only sample composed of beads and droplets, and very few fibers. Bar corresponds to 10 μ m.	59
Figure 38 25% Acetone/DMF mixture sample. The mat is composed of fibers and beads, with few droplets. Bar corresponds to 10 μ m.	61
Figure 39 A detailed road-map of micrometer fiber fabrication scheme for 50% Acetone/DMF ratio mixture, PVDF solution.	63
Figure 40 3D response surface plot generated via 441 data points calculated by the prediction formula given in Equation (5.6).	66
Figure 41 Same 3D surface plot given in Figure 40 with a view from opposite side of the surface plot.	67
Figure 42 XRD measurement results of an electrospun sample. Sample ID: Acetone/DMF:0.5 22.5cm 10kV)	69
Figure 43 Effect of electrical force applied on the fiber crystal structure.	70
Figure 44 DSC results of un-stretched electrospun sample (Sample ID: ES_0.5_22.5cm12kVunstr) and its comparison with stretched solution cast sample (Sample ID: SC_45str).	71
Figure 45 Correlation between elastic modulus and fiber diameter, and ultimate force and fiber diameter are plotted.	73
Figure 46 XRD result of pristine and stretched electrospun sample focusing at the critical region of interest (Sample ID: ES_22.5cm12kV).	74
Figure 47 Stretched and pristine electrospun samples (Sample ID: ES_0.5_22.5cm12kV).	75
Figure 48 Schematic representation of sample preparation for calcination process.	78
Figure 49 Heating scheme for the calcination of polymer/acetate precursor fibers to produce ZnO fibers.	79
Figure 50 TGA measurement results of the precursor fiber mat.	80
Figure 51 <i>ID_090306_24%Zn</i> is the precursor solution with the lowest zinc content. Although the precursor fibers are uniform and continuous (a), zinc oxide particles cannot always form continuous fibers, they mostly break into pieces due to small amount of zinc content (b).	81

Figure 52 ID_270306_50%Zn is the precursor solution with the highest zinc content. As it is seen in these SEM images, excess amount of zinc precipitates over both the precursor fibers (a) and the ZnO fiber itself after calcination (b).....	82
Figure 53 Optimized zinc content revealed uniform ZnO fibers.....	82
Figure 54 ZnO sample imaged by 200K magnified. Grains with an average diameter of 20nm can be easily seen on the fiber structure.	83
Figure 55 EDXS result showing the zinc and oxygen content of the fiber mat.	84
Figure 56 XRD data obtained from ZnO samples. The peaks are similar to the characteristic peaks of the wurtzite structure.....	85
Figure 57 ZnO whisker formation during calcination.	86
Figure 58 ZnO rod formation.....	87
Figure 59 Schematically representation of electromechanical response of an electroactive material.....	102
Figure 60 Heckman diagram showing the interrelationship among the mechanical, electrical, and thermal properties of materials. Coupled properties such as piezoelectric, pyroelectric, and thermal expansion are also given. Adapted from [105].....	103
Figure 61 Typical mechanical deformations of poled piezoelectric plates when subjected to an electric field (a) thickness and length; (b) radial; (c) thickness shear; and (d) bender (e.g. bimorph structures). Adapted from [105].	108
Figure 62 Schematically representation of microstructural changes during poling and after removal of poling.	109

LIST OF SYMBOLS AND ABBREVIATIONS

α -phase	alpha
β -phase	beta
δ	delta
γ	gamma
CFRP	Carbon fiber reinforced polymer
CNT	Carbon nanotubes
DMAc	Dimethylacetamide
DMF	Dimethylformamide
DoE	Design of Experiments
DSC	Differential Scanning Calorimeter
EAP	Electroactive Polymer
EDXS	Energy Dispersive X-Ray Spectrometer
eV	electronvolt
ϵ_b	Strain at break
E	Youngs (Elastic) Modulus
F_u	Ultimate force
$F(\beta)$	beta-phase fraction
$^{19}\text{F-NMR}$	Fluorine NMR
FT-IR	Fourier Transform Infra Red
μm	micrometer
nm	nanometer
cm	centimeter
mm	milimeter
kV	kilo Volts
$^{\circ}\text{C}$	degrees Celcius
MAV	Micro Aerial Vehicle

MPa	megapascal
NMR	Nuclear Magnetic Resonance
pCN ⁻¹	pico-coulomb per Newton
ppm	parts per million
PVA	Poly(vinyl alcohol)
PVDF	Poly(vinylidene fluoride)
PZT	Lead-zirconium-titanate
(PVDF-TrFE)	Poly(vinylidene fluoride)-(trifluoroethylene)
RSM	Response Surface Methodology
σ_b	Stress at break
SEM	Scanning Electron Microscopy
SSE	Sum of square errors
TGA	Thermogravimetric Analysis
UV	ultraviolet
w/w	weight by weight ratio
XRD	X-Ray Diffractometer
ZnO	Zinc Oxide

1. INTRODUCTION

Correct selection of materials is crucial since there is practically no engineering without materials. Often times, challenging engineering designs and applications necessitate custom-made material systems which call for intensive material characterization and process optimization.

1.1 Focus

Electroactive materials are significant in the use of many devices such as shape controllers and motors. Polymers and ceramics, and composites of these materials are used in the fabrication of these devices.

A polymeric material poly(vinylidene fluoride) (PVDF) is known to have polar characteristics and piezoelectric properties. Hence, PVDF films have been widely considered in sensor and actuator applications. Different processing techniques for PVDF films such as spin coating and solution casting were introduced by Benz et al. [1] and it was shown that production method of PVDF films is vital in terms of its piezoelectric activity. Therefore, optimization of process conditions and characterization of the end products are crucial to screen and enhance the desired properties of the films.

Ceramic materials such as lead-zirconium-titanates (PZT) are most frequently used in piezoelectric devices due to their remarkable electroactivity. Yet there has always been a motivation to discover novel materials with original structures; hence zinc oxide (ZnO) has been attracting attention in the last decade. It is not only an optically appealing material but also shows striking electronic properties. Different processing conditions of ZnO were introduced in 2.2. Among several fabrication

methods electrospinning is also used to produce ceramic nano-scale fiber mats. These fiber mats have the potential in the use of electroactive systems.

The inspiration of this study arises from constructing a smart composite materials system for actuator and sensor applications. With this inspiration in mind, the focus of this thesis is shaped towards optimizing the process conditions and characterizing the crystal structure of the two potential ingredient electroactive materials, poly(vinylidene fluoride) and zinc oxide, to exhibit their potential piezoelectric effects.

1.2 Approach

Optimization of PVDF film production technique is crucial in terms of the electroactive characteristics of the films. Solution casting and electrospinning were chosen for processing the PVDF films. Design of Experiments approach was utilized to monitor and to achieve desired electroactive and geometric properties such as polar crystalline formation, film morphology and uniformity. Individual effects and interaction of process parameters were observed to determine the optimum process conditions.

Crystallinity and polar crystal phase formation in PVDF films are critical when electroactivity is investigated. Following the PVDF film production, further mechanical treatment, especially stretching, are applied to the films to increase the β -phase crystallite portion. The polar β -phase in stretched and un-stretched PVDF films was explored to predict the potential electroactive behavior of the films.

Crystallinity and morphology of ZnO structures are also important. Fabrication of these structures should be optimized to produce desired material structures. To this end, electrospinning of ZnO fibers were investigated and fibers thus produced were characterized towards the need of electroactive ZnO crystals.

1.3 Objectives of the Study

The core of this study arises from the inspiration towards production and characterization of piezoelectric material systems for actuator and sensor applications such as a smart wing of a Micro Aerial Vehicle. Poly(vinylidene fluoride) and Zinc Oxide were selected as electroactive piezoelectric materials and studied under three primary objectives:

- to process PVDF films via solution casting and optimize the PVDF crystal structure in order to attain the highest efficiency in the piezoelectric response
- to process PVDF based polymeric solution via electrospinning for fibrous mats and investigate crystalline structure and potential piezoelectric response
- to process Poly(vinyl alcohol) and Zinc Acetate based precursor solution via electrospinning and calcining to form ZnO ceramic fibers

Chapter 2 present the literature survey to summarize the studies done so far related to these three objectives. Chapter 3 explains the materials of interest. Chapters 4 to 6 covers the 3 parts of this thesis work as PVDF Films, PVDF Fiber Mats and ZnO Fiber Mats, respectively. Experimental methods, collected data and results are discussed in these chapters. Suggestions for future studies are given in Chapter 7. Concluding remarks are finally listed in Chapter 8.

2. LITERATURE SURVEY

2.1 Poly(vinylidene fluoride): A Sensor and An Actuator

Among the electroactive polymers (EAPs), PVDF and its copolymers such as Poly(vinylidene fluoride)-(trifluoro ethylene) (PVDF-TrFE) have been increasingly applied as piezoelectric actuator and sensor. They have been acting as the non-brittle alternatives to electro-ceramics, yet, with a lower level of performance [2]. Thus, they are also called to be a new class of flexible actuators that can convert electrical energy to mechanical energy. PVDF, for instance, was used in space environments like in shape control of inflatable structures with complex 3-dimensional geometries [3, 4]. Another term used for EAPs is “artificial muscles” since they have similar deeds to biological muscles. They have mass, cost, power consumption and fatigue characteristics with applicable actuation displacement over conventional actuators such as PZTs or bariumtitanates. EAPs have a wide range of applicability in medical industry as artificial muscles, synthetic limbs and prostheses; also in civil or military disciplines as robotic arms, miniature insect-like robots and micro air vehicles [5-11].

Poly(vinylidene fluoride) has been synthesized since the 1940s yet its ferroelectric property was discovered in late 1960s. PVDF copolymers have been materials of interest since 1990s with the ignition of artificial muscle industry [6]. PVDF is generally used in structural health monitoring systems as pressure and volume displacement sensors [12-17] due to its exceptional chemical stability and mechanical flexibility which can be easily conformed to complex surfaces. Moreover, its biocompatibility makes PVDF sensor a desirable candidate to be used in biological environments [18]. Besides its sensing capability, PVDF is also applied in the actuation mechanisms that can be thermally [19], optically [20] or electrically [21] stimulated.

Discovery of piezoelectrical properties of PVDF date back to 1969 when Kawai demonstrated that thin poled films of PVDF revealed a large piezoelectric coefficient, $6 - 7\text{pCN}^{-1}$, a value which is about ten times larger than had been observed in any other polymer. This led the scientists to consider PVDF actuator and sensor applications [22]. Sunar and Rao gave a thorough literature survey on vibration sensing and control of flexible structures using piezoelectric materials. It is observed from that study that the use of PVDF films as sensor and actuator is well recognized and utilized [23]. Lee et al., for instance, developed monomorph and bimorph multifunctional actuators with $45\mu\text{m}$ thick PVDF commercial films (Kureha Inc). Application of a mechanical vibration to the actuator generated a maximum output voltage of 0.2V under 10mm tip displacement [24]. Gao et al., likewise, developed an active actuation and control of suspension structures by utilizing PVDF films in Hard Disk Drives, in which PVDF is finally found to be an effective actuator and sensor. They observed a maximum deflection of 1310nm in a cantilever geometry, when an input voltage of 22.5V was applied [25]. Moreover, Lee et al. developed a smart beam structure with four layers of PVDF to actively control the shape of the beam [26].

Piezoelectric actuation and sensing capability of PVDF results from four key structural facets that also exist for most electrically stimulated polymers. Broadhurst and Davis summarized these critical elements as i) the presence of permanent dipoles, ii) the ability to orient or align the molecular dipoles, iii) the ability to uphold this dipole alignment for long periods of time, and iv) the ability of the material to undergo large strains under mechanical stress [27]. These elements are necessary for semicrystalline or amorphous polymers that have piezoelectric property.

In order to render a semicrystalline polymer piezoelectric, it must have a polar crystalline phase. These crystallites are dispersed within the amorphous region of the polymer as represented in Figure 1 [28]. The crystallinity of the polymers significantly depends on the process conditions and thermal history of the polymer.

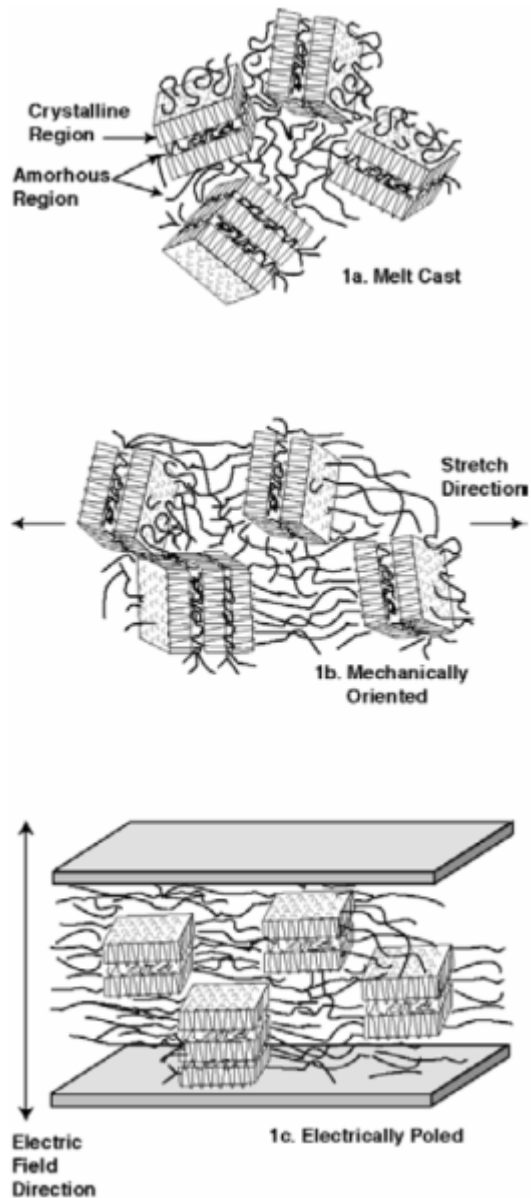


Figure 1 Schematic representation of crystallites in amorphous phase of PVDF. (a) melt cast film (b) mechanically stretched melt cast film (c) poled melt cast film. Courtesy of NASA [28].

The eminent crystallographic property and piezoelectric activity of PVDF comes from its spatially symmetrical disposition of the hydrogen and fluorine atoms along the polymer chain. This gives rise to unique polarity effects that influence the electromechanical response, solubility, and crystal morphology. Furthermore, it yields an unusually high dielectric constant among the other polymers. The amorphous phase in PVDF has a glass transition temperature that is well below room temperature (-35°C), hence the material is quite flexible and readily strained at room temperature. PVDF is

typically 50 to 60% crystalline [29] depending on thermal history and process conditions and has many crystal phases. The four of them are well-known, α , β , γ , and δ , of which at least the three are polar [28]. Details of the crystal phases and their properties are given further in Section 03.1.

It is important to characterize the PVDF films according to their crystalline structures, so that the process conditions are optimized to achieve a desired physical property, in this thesis the piezoelectricity. There have been a considerable amount of interest on the optimized piezoelectric response and the characterization of PVDF. Gregorio and Cestari studied the effect of crystallization temperature of PVDF on its crystalline phase content and morphology [30]. Melt and solution cast films were prepared and exposed to a varying temperature and time scale between 25⁰C to 185⁰C and 10min to 15hr, respectively. The content of the crystalline phases were determined by Differential Scanning Calorimeter (DSC) measurements and relative amount of the phases were calculated from the Fourier Transform-Infrared (FT-IR) spectroscopy intensities of the characteristic phase peaks. Emphasis was given to α - and β -phases and the percent of β -phase content was introduced. Morphology of the cast films was also analyzed to determine the quality of crystallinity at different temperatures. Benz and Euler analyzed the effect of different preparation conditions on the crystalline phase of PVDF [1]. They investigated the dissimilarity between solution cast and spin coated films together with the effect of annealing temperature of films similar to the study of Nakamura et al. [31]. The samples were characterized via FT-IR and DSC. Quantitative analysis was done by FT-IR, again by using the characteristic peaks of different crystal phases. Matsushige et al. approached from a mechanical behavior point of view and introduced the crystal transformation mechanism of PVDF under tensile and compressional stresses [32]. Crystal transformation of PVDF is monitored via an X-Ray measuring system while the films were drawn and uniaxially compressed. Crystal content of the mechanically deformed films was further characterized by IR spectroscopy. Davis et al. examined the effect of electric field on the phase changes of PVDF films [33]. They utilized a poling scheme on two types of PVDF films; one unoriented and the other oriented. The results exhibit the α - to β -phase transformation under applied electric field. Bodhane and Shirodkar investigated the effect of thermal evaporation technique on the crystal modification and physical properties of the

prepared PVDF films [34]. X-Ray Diffractometer (XRD) and FT-IR measurements revealed the quantification and form of the introduced phases during this process.

There are several polymer film process techniques such as solution casting, melt casting, melt press, and spin coating. Many of the researchers focused on the solution casting to observe PVDF film properties due to its simplicity in production and affinity to large scale film manufacture. Thus, many of the researchers focused on this process to observe PVDF film properties. One of the latest studies is performed by Salimi and Yousefi who concentrated only on the solution casting process and the effect of process parameters on the crystalline phase formation [35]. They chose temperature and solvent type as the process parameters and directed their attention on these effects. They analyzed the effects extensively via utilizing several characterization tools and equipments. They not only performed the investigation in the solid state of polymer, but also investigated the solution properties and chain conformational changes in the solution prior to casting. Solid state measurements were done by FT-IR only to quantify the relative phase amounts; whereas the conformational changes due to temperature modification in the solution was observed via ^{19}F Fluorine Nuclear Magnetic Resonance (^{19}F NMR) spectroscopy. Similar to previously mentioned scientists, Salimi and Yousefi also obtained the relative crystallinity amount of β -phase films processed at different temperatures. Quantified analysis was performed by FT-IR measurements with a wave number range of $400 - 1000\text{cm}^{-1}$. They also utilized the ^{19}F NMR on PVDF solutions prepared with Dimethylacetamide (DMAc) and cyclohexane to observe the temperature effect. Observed peak shifts at different temperatures revealed the change in the chain conformations. Effect of mechanical stretching was also inspected and the phase contents were also analyzed and quantified.

Another simple and efficient polymer film-like production technique is electrospinning [36-45] for which the details are presented in 5.1. Mats of sub-micron scale fibers of natural or synthetic polymers can be produced via the electrospinning process. Electrospinning of PVDF also attracted attention. Zhao et al., for instance, carried out electrospinning of PVDF to be used for various applications including reinforcing components, biomedical scaffolds and tissue regeneration [46]. Major research interest was the effect of alternative DMF/Acetone solvent mixture ratios on the fiber geometry and morphology. Moreover, they investigated the effects of acetone

amount, polymer concentration and collector distance on the membrane morphology and fiber diameter. They produced PVDF fiber mats of $\sim 45\mu\text{m}$ thick with 50nm to 300nm fiber diameter. Another recent study was employed by Nasir and his colleagues [47]. They analyzed the influence of polymer concentration, collector distance, flow rate of polymer solution, and applied voltage on the structure, morphology and geometry of fibers and mats. They also paid attention to the crystal structure of the electrospun mats, and characterized the mats via DSC, FT-IR, and XRD to qualitatively and quantitatively analyze the relative β -phase content.

In addition to morphology and structural characterization of electrospun PVDF mats, Choi and his coworkers put emphasis on polymer electrolyte application of electrospun PVDF fiber webs [48]. They inspired from the application of PVDF and its copolymer in the production of rechargeable batteries. They relied on the nano-porous structure of PVDF fiber mats that these structures have great potential towards electrolyte or separator in batteries. Kim et al. discussed a similar approach regarding the electrolyte application and investigated the effects of electrospinning of PVDF solutions with different polymer contents [49].

Electrospinning of PVDF was also utilized in making the composite fibers with introduction of carbon nanotubes (CNT). Seoul et al. investigated the electrospinning of PVDF/DMF solutions with carbon nanotubes as a mechanical, electrical and optical reinforcement [50]. They analyzed the effect of different CNT ratios to optimize the percolation threshold and made electrical characterization of composite fibers to further monitor the effect of introduced CNT.

Although the piezoelectric activity of PVDF has been widely known for long time, to the author's knowledge, electrospun PVDF fibers were not investigated until Pawlowski and his co-workers [43]. They produced and optimized PVDF fibers via modifying the solution properties to achieve desired crystalline phases. They further applied the optimum set of fibers onto a micro air vehicle wing to actively control its spatial dimensions.

2.2 Zinc Oxide: A Promising Electronic Material

Zinc oxide (ZnO) has generated great interest in the last few years due to its abundant availability in earth crust and its promising electronic and optical properties to be applied in the photonics industry. It is unique due to its semi-conducting and piezoelectric dual properties. Its semi-conducting property comes from its direct band gap of $\sim 3.37\text{eV}$ and large excitation binding energy (60meV). It further exhibits near-ultraviolet (UV) emission and transparent conductivity. Its piezo-activity relies on its non-centrosymmetric symmetry which is vital in building electro-mechanical coupled sensors and transducers. In addition, ZnO is bio-safe and bio-compatible, and can be used for biomedical applications without coating. With these exclusive benefits, ZnO has become one of the most important nanomaterials for integration with micro-systems and biotechnology [51]. Furthermore, the complex growth process of ZnO produces various nano-structures which nominate ZnO a potential material for nano-machines.

Zinc oxide has been under investigation generally due to its possible great potential for sensing [52], catalysis [53], optical emission [54, 55], piezoelectric transduction and actuation [56] properties. Viswanathamurthi and Xu, for instance, presented photoluminescence and field emission characteristics of the ZnO structures to emphasize the significance of the ZnO nanofibres in nanoscale optoelectronic applications used as light emitting devices [54, 55]. Zhao et al. on the other hand characterized an individual ZnO nanobelt via a piezoresponse force microscope which gave promising results for the future of ZnO in nano-sensors and nano-actuators industry [57].

There have been several studies on the processing of complex ZnO nanostructures [54, 58-61] (Figure 2), such as nanowires [62-64], nanorings [65, 66], nanonails [64], nanotetrapods [51], nanohelices [51], nanorods [67-71], and nanofibers [72-75]. However, the fabrication of these nano-structures with controlled crystallinity and morphology and characterizing them appear to be significant challenge in nano-science that motivates further investigations on developing controlled structures of ZnO.

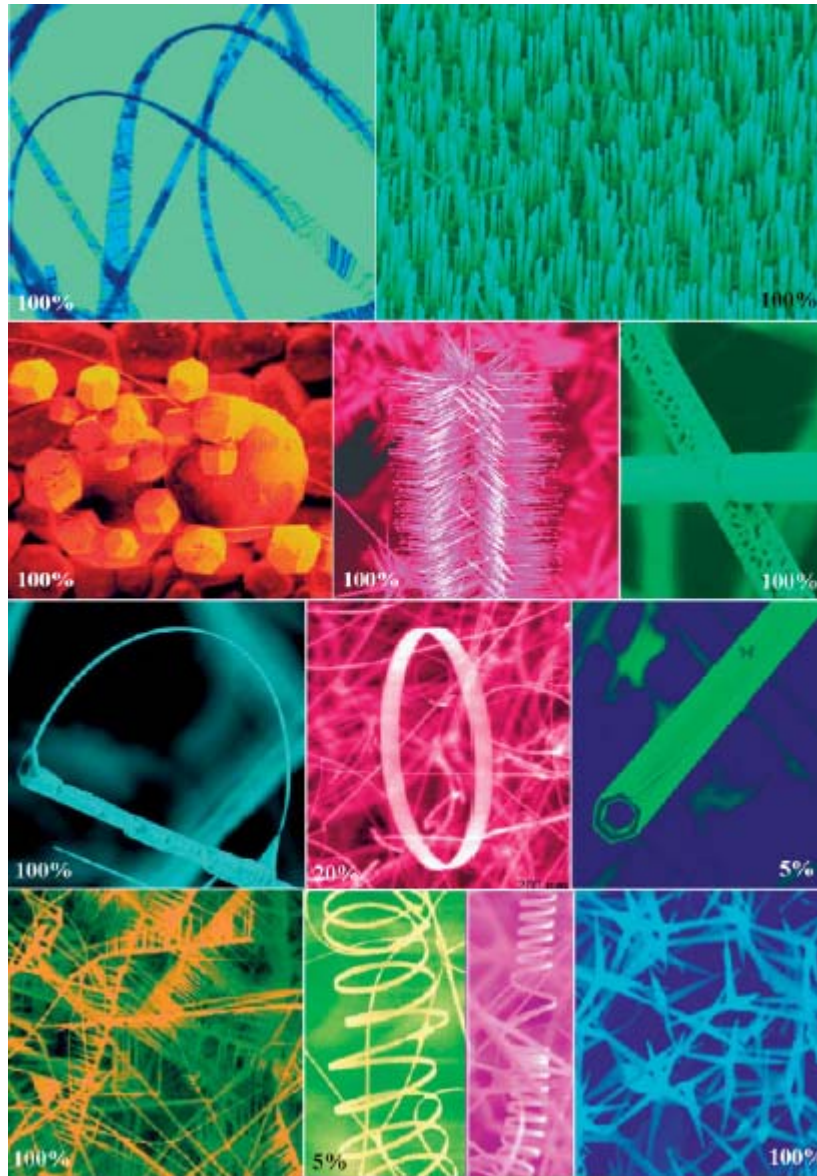


Figure 2 Nanostructures developed from ZnO. Courtesy of Wang et al. [51]

There are various fabrication methodologies to produce ZnO structures such as chemical vapor deposition [52], solid vapor phase process [58], thermal evaporation [76], electrodeposition [77, 78], and sputtering techniques. Different types of nanostructures ranging from nanorings to nanorods can be generated by each of these methods at different process conditions. The problem structural control still holds for each of these fabrication methods.

Another additional manufacturing technique is electrospinning and annealing by which nano-scale fibers of ZnO are produced [72, 74, 75, 79, 80]. Contrary to other

production schemes, the fibers constructed via electrospinning are continuous. Besides, it is easier to control the electrospun fiber geometry since it depends on the electrospinning parameters where the effect of the parameters has been well understood. Yang and his co-workers introduced the electrospinning of ZnO fibers and characterized them [81]. Wu and Pan on the other hand concentrated on the change in fiber diameter due to the varying calcination time [80].

2.3 Electroactive Composite Materials

Considering the written studies so far, electroactive composite materials can be divided into two groups: i) electroactive materials integrated into a composite material system, and ii) a hybrid system with active and inactive parts. Although hybrid materials are not composites by definition, they are accepted to be involved in this group due to the similarity in the end-use and the composition of the ultimate structure.

There are various types of ingredients used in the fabrication of composite materials. A preliminary material, as polymer film, can be reinforced by different material types and geometries. The reinforcement may be utilized via a fine dispersion of small particles, chopped fibers/rods/tubes, or continuous fibers/rods/tubes such as carbon nanotubes, ceramic rods, and the like. The dispersion quality is another effect that alters the quality of the composite material. The reinforcement can be employed either with randomly distributed or perfectly aligned particles. These different dispersion types incorporate distinct reinforcement schemes, thus modifies the final properties as the spatial properties of the dispersion is controlled..

Regarding the first classification of electroactive composite materials, there are some works in the electroactive part integrated composite material systems which are generally used in the in-situ health monitoring of structural systems as ultrasonic transducers or acoustic emission sensors [15, 82-86]. The difference between the conventional structural health monitoring systems and these in-situ monitoring systems is that the active polymeric layers are embedded into the composite structure; hence the material system works as a whole. However, traditional health monitoring systems include sensors attached to the surface of the structure. Kwon and Dzenis, for instance,

embedded PVDF films of tens of microns thick into the graphite/epoxy (CFRP) composite laminates to monitor the tensile failure of unidirectional CFRP laminates [15].

Second class of composite actuators embrace hybrid systems in which two distinct materials are included in one system but they are not merged into one structure. It can be stated like the hybrid systems are “heterogeneous”; one can identify and see the two different materials, yet, the composites are “homogeneous”; the materials are perfectly merged into one another forming a single body. Hybrid actuation systems, hence, utilize the contributions of the actuation elements courteously. As Su and his colleagues developed a polymer-ceramic hybrid system which derives a larger strain, hence a better efficiency, due to the individual contribution of the elements [87]. Nevertheless, the polymer part can not adhere to the ceramic part thus one cannot provide a cooperative –mutual- property from the hybrid structure.

3. PIEZOELECTRIC MATERIALS SYSTEMS OF INTEREST

3.1 Piezoelectric Polymer: PVDF

Poly(vinylidene fluoride), PVDF, is a highly non-reactive and pure thermoplastic fluoropolymer possessing ferroelectric, chemically resistive and mechanically favorable properties. It has been a research interest particularly after its ferroelectric properties were discovered in 1940s.

The chemistry of PVDF is quite simple. The monomer unit consists of two hydrogen and two fluorine atoms bonded to two carbons. Although the structure is simple, different form of bonding of monomers in the polymer chain creates head-to-head or tail-to-tail defects, which are common defects in many polymer structures.

In its solid state, PVDF is a semi-crystalline material with approximately 50% crystallinity. There are several polymorphs of this polymer, yet, four of them are well understood and described in literature: α , β , γ , and δ , or phases II, I, III, IV respectively.

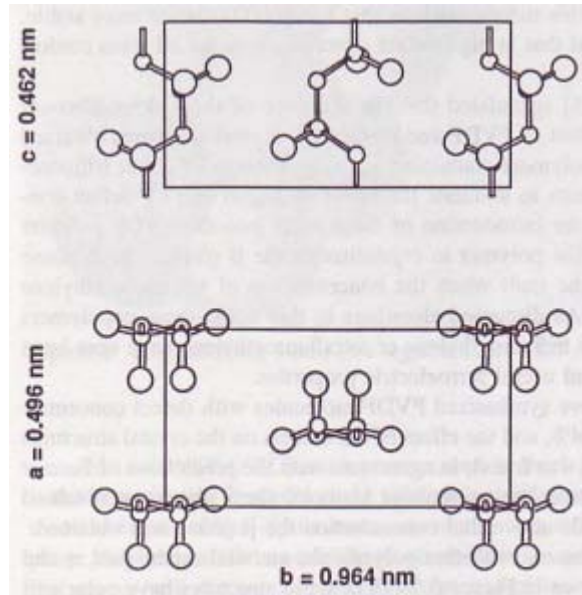


Figure 3 α -Phase structural conformation, adapted from [29]

After cooling PVDF from its melt state, the polymer forms the crystalline but non-polar phase, α -Phase, as it has the lowest energy molecular conformation. The crystal structure of the α -phase is shown below in Figure 3. Molecules in the α -phase are in a trans-gauche-trans-gauche' ($TGT\bar{G}$) conformation which is a distorted structure due to the steric hindrance between the fluorine atoms. There is a large dipole moment associated with the carbon-fluorine bond and the space-filling model in Figure 4 shows that the net dipole moment is perpendicular to the chain axis. There are two chains in each unit cell (Figure 3), and the dipole moments of these two unit cells are directed in opposite directions [29].

The β -phase has been more attractive to researchers as it brings the ferroelectricity. The polymer chain represented in Figure 5 is in a distorted, planar zigzag, and all-trans (TT) conformation. As the space filling model in Figure 6 suggests, β -phase has a polar unit cell with a large dipole moment.

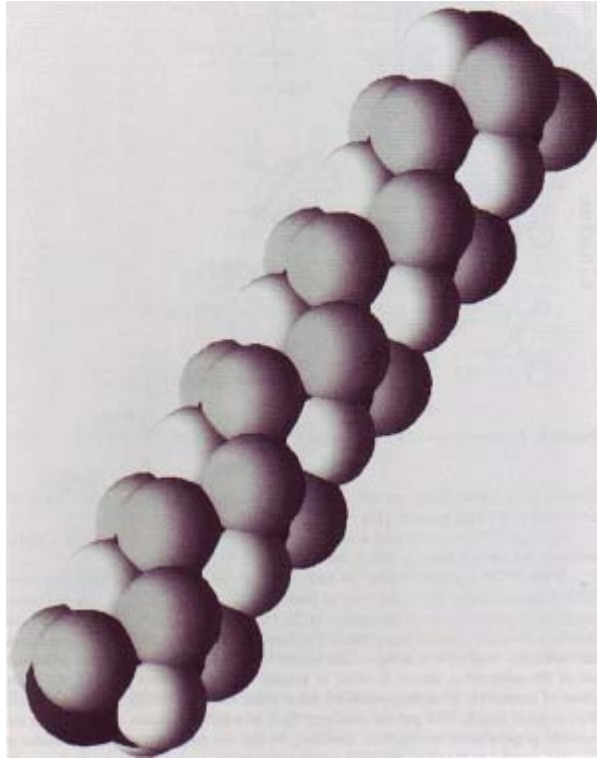


Figure 4 Space-filling model of the α -phase PVDF, adapted from [29]

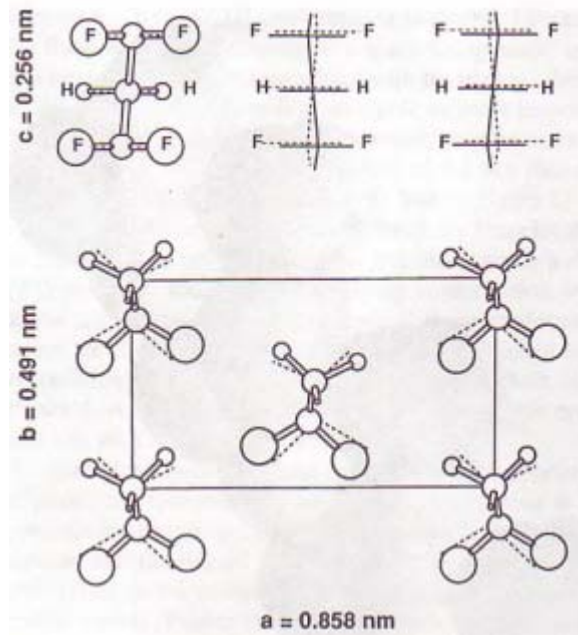


Figure 5 β -Phase structural conformation, adapted from [29]

In addition to α - and β -phases, γ - and δ -phases are also reported [29]. Both of these polymorphs have polar unit cells, yet, the dipole moments are smaller than that of β -phase. Hence, α - and β -phases are attracting more attention.

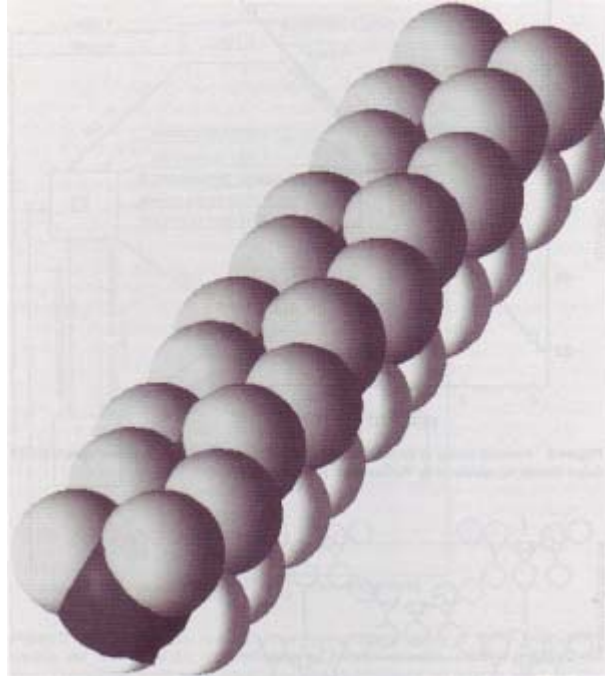


Figure 6 Space-filling model of the β -phase PVDF, adapted from [29]

3.2 Piezoelectric Ceramic: ZnO

Zinc oxide (ZnO) is a chemical compound that commonly exists in white hexagonal crystals in a stable wurtzite crystal with lattice constants $a = 0.325nm$ and $c = 0.521nm$. The crystal structure is hexagonal close pack structure, analog of the zincblende (ZnS) structure, where the atoms are stacked together in the ABABAB... sequence as represented in Figure 7.

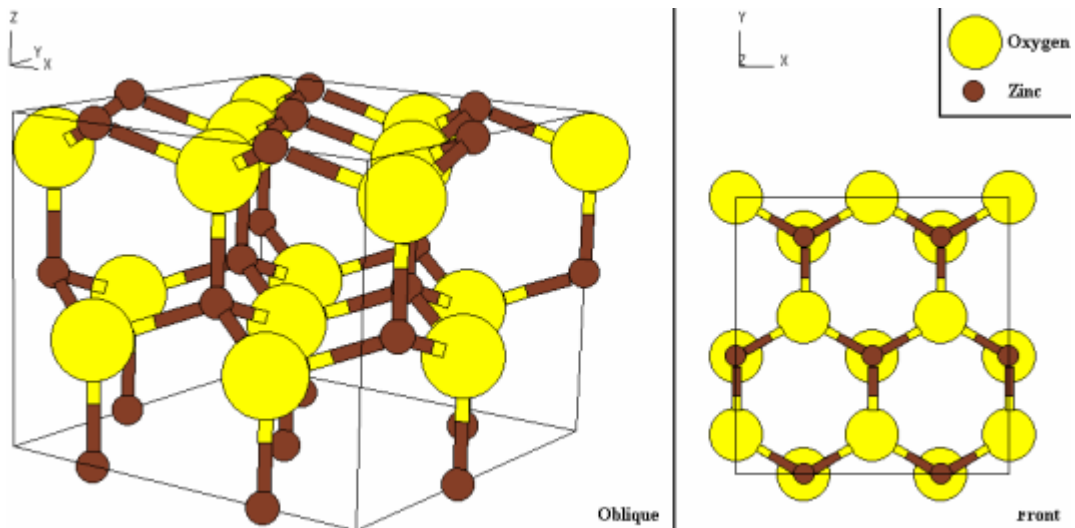


Figure 7 Zinc oxide crystal wurtzite structure¹

The compound keeps its white color unless heated. At elevated temperatures the crystal becomes yellowish, which represents the luminescent property of the ZnO. When the structure is cooled down, it returns back to its white color. It is a II-IV type semiconductor with a direct band gap of ~ 3.2 eV (387 nm, deep violet/borderline UV) [59, 88] and suitable for electronics applications.

Physical properties of ZnO given in Table 1 make it attractive in various disciplines. One of the common applications of zinc oxide is the gas sensors since bulk and thin films of ZnO have demonstrated high sensitivity for toxic gases. Since 2003, it has been employed in recent research to construct blue LEDs and invisible thin film transistors. Thin-film solar cells, liquid crystal and flat panel displays are other typical applications of this material. Zinc oxide is transparent and conductive, and can therefore be used as a transparent electrode, usually used in microelectronic applications. It has also been considered for spintronics applications, theoretically, due to its ferroelectric property at room temperature, however this property of ZnO has not been fully understood yet and is still under investigation.

A variety of zinc oxide structures are produced via several methods as explained in 2.2. All methods allow the growth of a rough layer in several different geometries.

¹ Adapted from <http://cst-www.nrl.navy.mil/lattice/struk.picts/b4.s.png>.

One of the novel and simple method to produce zinc oxide fiber-like nanostructures, nano-rods and nano-whiskers is electrospinning. It is relatively new and still under investigation for growing fibers with controlled nano geometries.

Table 1 Physical properties of zinc oxide structures. Courtesy of Fan et al. [59]

Properties	Value
Lattice constant, a_0	0.32469 nm
Lattice constant, c_0	0.52069 nm
Density	5.606 g/cm ³
Melting point	2248 K
Relative dielectric constant	8.66
Gap energy	3.2 eV (direct)
Intrinsic carrier concentration	$< 10^6$ cm ⁻³
Exciton binding energy	60 meV
Electron effective mass	0.24
Electron mobility (300 K)	200 cm ² /Vs
Hole effective mass	0.59
Hole mobility (300 K)	5 – 50 cm ² /Vs

4. PVDF FILMS

4.1 Process: Polymer Film Production by Solution Casting

Solution casting is straightforward method to produce polymeric films and can easily be used in characterization and preliminary observation of the structures in the laboratory environment. In comparison to other film production methods, such as extrusion method or calender method, melting temperature of the resin (dissolution temperature for solution casting method) is lower (max. 110⁰C)--resulting in less heating requirement. It requires less amount of thermal stabilizer or other expensive additives (UV absorber, and the like).

The procedure is simple: a dilute homogenous polymer solution is prepared with an appropriate solvent. Then the solution is slowly poured onto a smooth substrate - commonly glass - and left for solvent to evaporate for a couple of hours. Temperature and duration of the evaporation vital for the physical properties of the polymeric film; especially the crystallinity of a semi-crystalline polymer is affected significantly.

The principle aim of this part is to observe the crystallinity induced due to different process conditions and stretching the films in order to compare with electrospun samples.

Poly(vinylidene fluoride) (Alfa Aesar) solution in 10% w/w was prepared with DMF (Merck) at room temperature. Note that Acetone was not considered in solution casting as the accelerated evaporation is not favorable unlike in the case of electrospinning. Then the solution is elevated to the desired casting temperature leading the polymer chains to have a conformational change towards the thermodynamically stable crystal structure at that temperature. The 72mm³ (1.056g solution) of PVDF solution is then slowly poured on the glass substrate, which was heated to the casting

temperature beforehand pouring the solution. The solutions were kept in the oven, at the desired temperature for different durations. Temperature ranges were from 40⁰C to 100⁰C increased by 10⁰C steps for each different sample so that the effect of temperature on the crystallinity of PVDF may be detected. Each sample was also kept at the desired temperature for 1 hour to 12 hours to observe the duration effect on the crystallinity of PVDF. The levels for temperatures and casting durations in Table 2 were experimented in a combinatorial fashion and approximately 50 to 60 μ m thick films were produced for each combination.

Table 2 Casting temperature and duration exerted on the PVDF solution

Casting Temperature (⁰ C)	Casting Duration (hour)
40	1
50	2
60	4
70	8
80	12
90	
100	

After taking the films out of the oven, each produced film was directly put into the freezer at -25⁰C in order not to let the polymer chains alternate their chain conformation. Each film was then characterized for its three different physical properties: crystallinity, morphology and mechanical property.

4.2 Characterization Tools

Two different crystallinity properties, percent crystallinity and crystal phase formation, of the PVDF films were characterized. Fourier Transform Infra Red (FT-IR) Spectroscopy (Bruker Equinox 55) and X-Ray Diffraction (XRD) (Bruker AXS D8) were utilized to observe the distinct crystal phases and their relative amounts. Differential Scanning Calorimeter (DSC) (Netzsch DSC 204 Phoenix) was used both for the crystal phase investigation and percent crystallinity determination of the films.

Moreover, Nuclear Magnetic Resonance (NMR) (500MHz Varian Inova) was used to observe the conformational change in the PVDF solutions due to the thermal modifications in the solutions.

Mechanical properties of PVDF films were determined by the MTS Synergie 200 Tensile Testing Machine located at Rotopak / Alcan Packaging (Figure 8). The tensile tester has pneumatic clamps, which are crucial for our films because they are very sensitive to clamping and can easily be torn by metal and roughened clamp surfaces. 100N load cell with 0.1N resolution was used to stretch all films. Maximum load, stress at break, strain at break, and Young's Modulus of the films were assessed.



Figure 8 MTS Synergie 200 tensile testing apparatus with pneumatic rubber clamps (In courtesy of Rotopak-Alcan Packaging)

Piezoelectric characteristics of PVDF films are the major interest in this study. To measure the piezoelectric property of the PVDF films, the films first need to have the necessary crystallographic phase, the β -phase. In order to generate or increase the composition of β -phase in the PVDF films, the films were stretched to 4 times of their original lengths using the ZWICK Z100 Universal Testing Machine with its 10kN load cell. Strain rate for the elongation was 5mm/min and the films were heated to about 80⁰C by two heating guns placed near the clamps during the stretching process (Figure 9). Temperature at the test section was monitored by using two thermocouples one at

each side of the film. Stretched films were then characterized in order to observe their crystallographic structure.

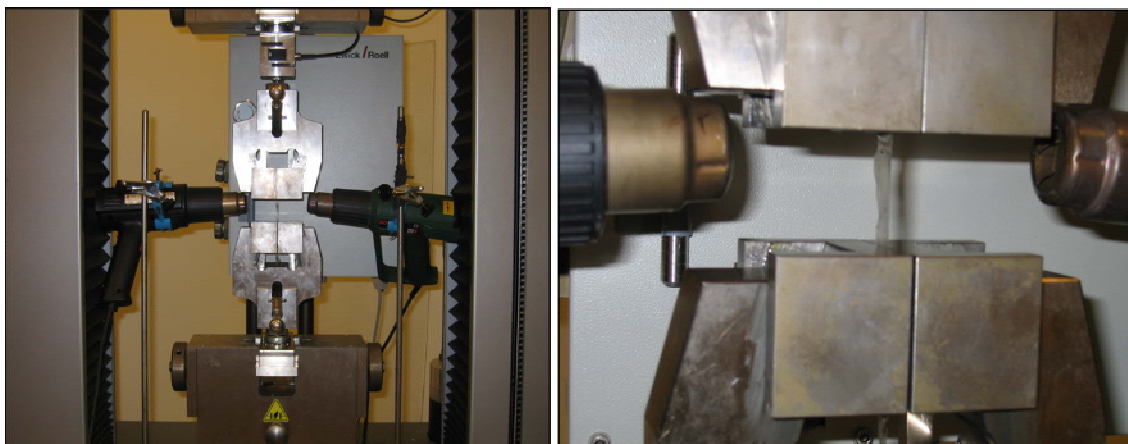


Figure 9 Homemade stretching set-up to elongate films for orienting the chains and thus dipoles to enhance polarity.

4.3 Results and Discussions

4.3.1 Pristine Solution Cast PVDF Films

One of the film fabrication methods employed in this study was solution casting. PVDF / DMF solutions of 10% by weight were prepared and stirred until a homogenous solution was obtained at the targeted casting temperature. Films were then cast at different temperature regimes as given in Table 2. The purpose of casting at this temperature and duration regime was to observe the optimum casting temperature and duration in order to attain the highest level of β -phase crystalline formation. The optimum region was sought via ^{19}F -NMR and FT-IR. The objective of this part of the study was to construct a reference on the traditional solution cast films and to compare the results of later section for electrospun samples with the reference.

4.3.1.1 FT-IR and NMR Measurements

^{19}F -NMR was used to monitor the temperature at which the chain conformational change occurs. It is thus a semi-quantitative analysis in obtaining the optimum

temperature range. FT-IR measurements, on the other hand, reveal the characteristic peaks of α - and β -phase of PVDF films. The intensities gained from these measurements can be used to clarify the relative amount of crystalline phases.

In order to determine the fraction of the β -phase present in each sample, IR absorption bands at 764 and 840 cm^{-1} , characteristic bands of α - and β -phases, respectively, were chosen and a procedure similar to Salimi and Yousefi [35] was utilized. Although this approach is not precise, once used consistently throughout the work it is thought to be useful for making comparisons on fraction of β -phase. Based on the Beer–Lambert law and the absorption coefficients of $K_\alpha = 6.1 \times 10^4$ and $K_\beta = 7.7 \times 10^4 \text{ cm}^2/\text{mol}$ at 764 and 840 cm^{-1} , the fraction of β -phase, $F(\beta)$, was calculated using the following Equation (4.1) [35]:

$$F(\beta) = \frac{X_\beta}{X_\alpha + X_\beta} = \frac{A_\beta}{1.26A_\alpha + A_\beta} \quad (4.1)$$

where, X_α and X_β are crystalline mass fraction of α - and β -phases and the A_α and A_β are their absorption bands at 764 and 840 cm^{-1} , respectively. β -phase fraction of the cast films were calculated from the FT-IR absorption bands above and the relative ratios are attained as given in Figure 10.

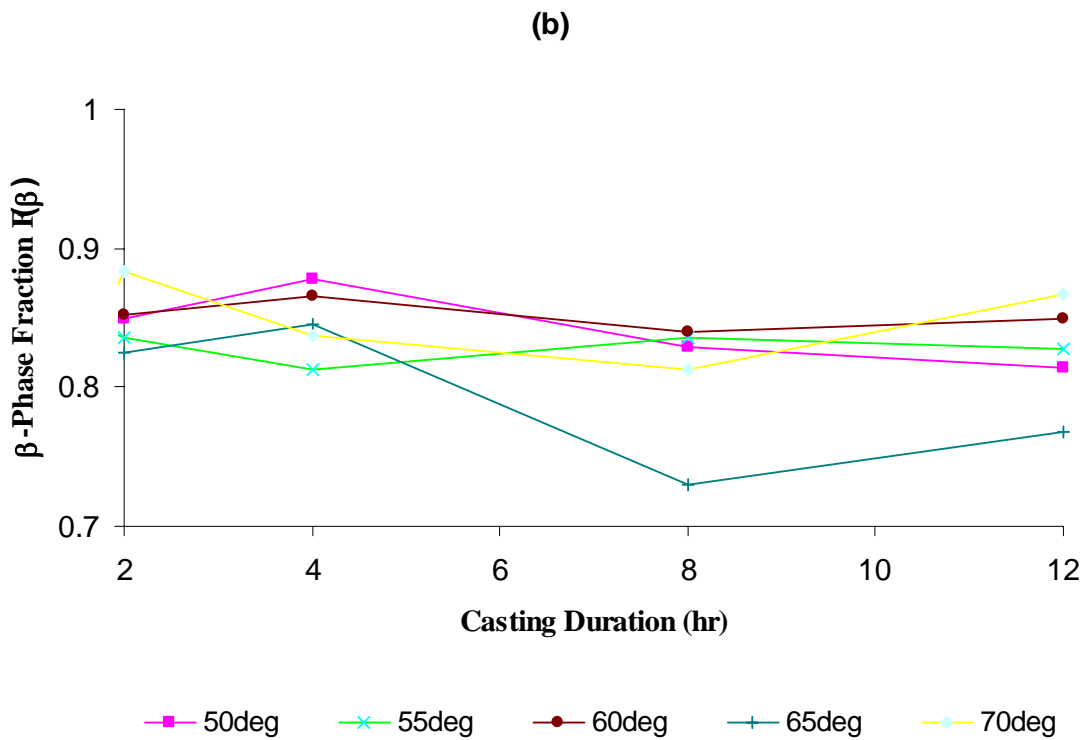
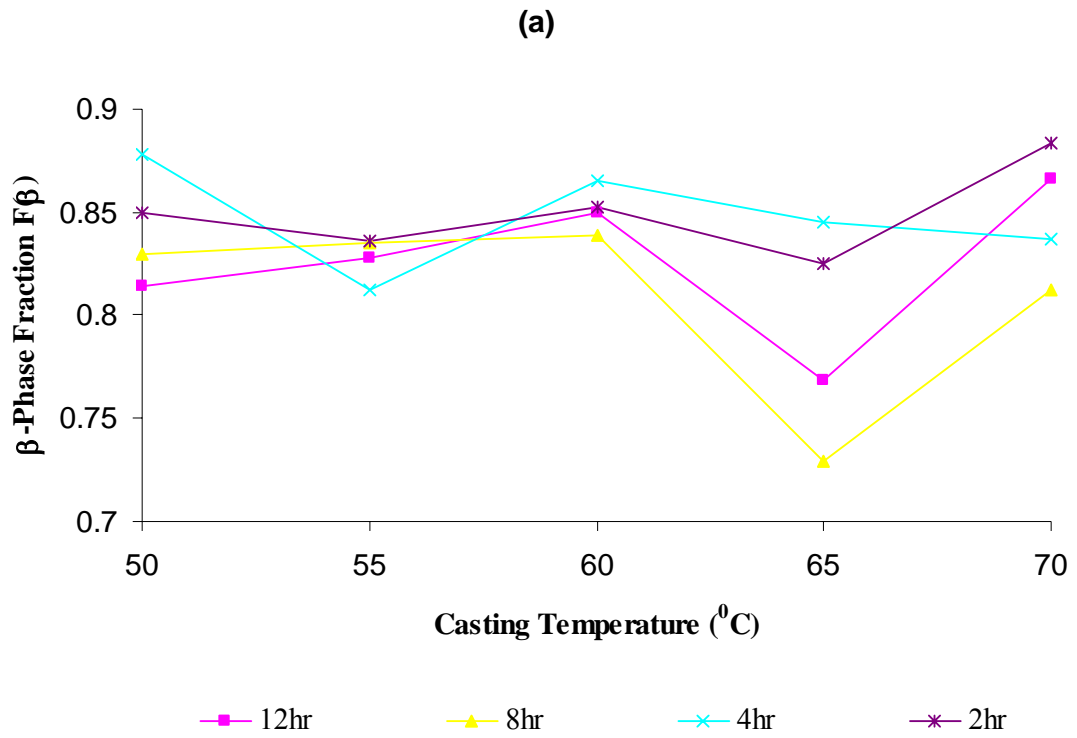


Figure 10 β -phase crystallinity modification due to a change in temperature (a) and duration (b).

From the figure above, temperature range for the optimum β -phase increment is not possible to determine. However, the casting duration should not exceed 4 hours, since the optimum limit is lost beyond that point.

Effect of casting temperature was further analyzed via NMR and the solution properties revealed an optimum temperature for the phase transformation. The temperature of the solution was elevated to 40, 45, 55, 65, and 70°C, and kept at that temperature for 10 minutes to allow a change in the polymer chain conformation.

Figure 11 presents a shift towards left at higher temperatures, which suggests that the CF_2 groups in the polymer chain are getting closer as in the all-trans (TTT) β -phase conformation: staging a typical representation of β -phase transformation. In addition, as seen in Figure 12, there are two peaks superposed into one composite wider peak. As the temperature was elevated from 40 to 65°C, right peak lost its intensity, while the left one gained. In other words, the peak of the 40°C sample is slanted right where that of 70°C is slanted left. Considering either of the cases, it is apparent that a chain transformation occurs from 45°C to 65°C. The transformation of the two peaks in this one heterogeneous peak is assumed to be a representation of the chain conformation in the polymer solution, which is happening due to a temperature change.

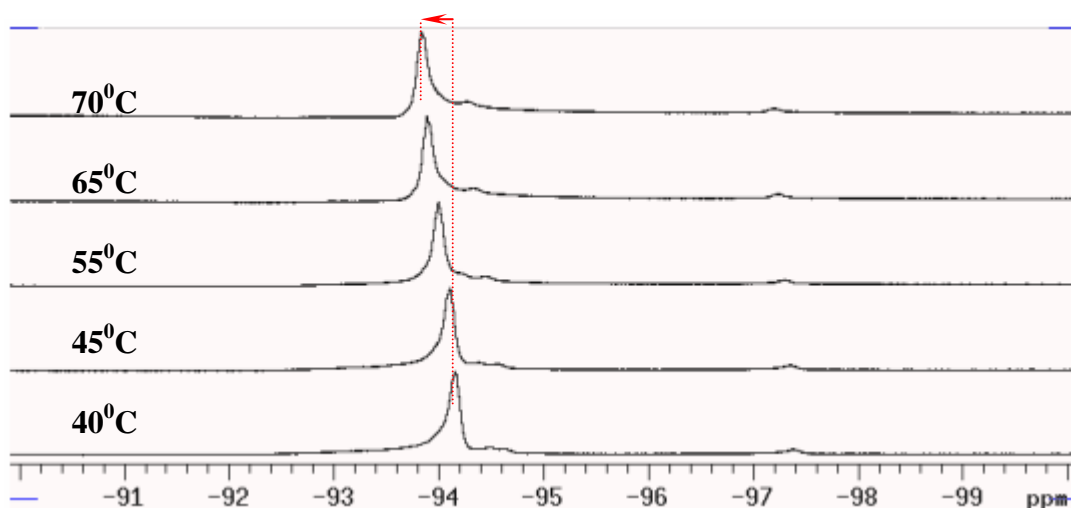


Figure 11 NMR measurement obtained from a stack of different temperatures: 40-45-55-65-70°C. One can observe the shift of the spectrum moving towards left.

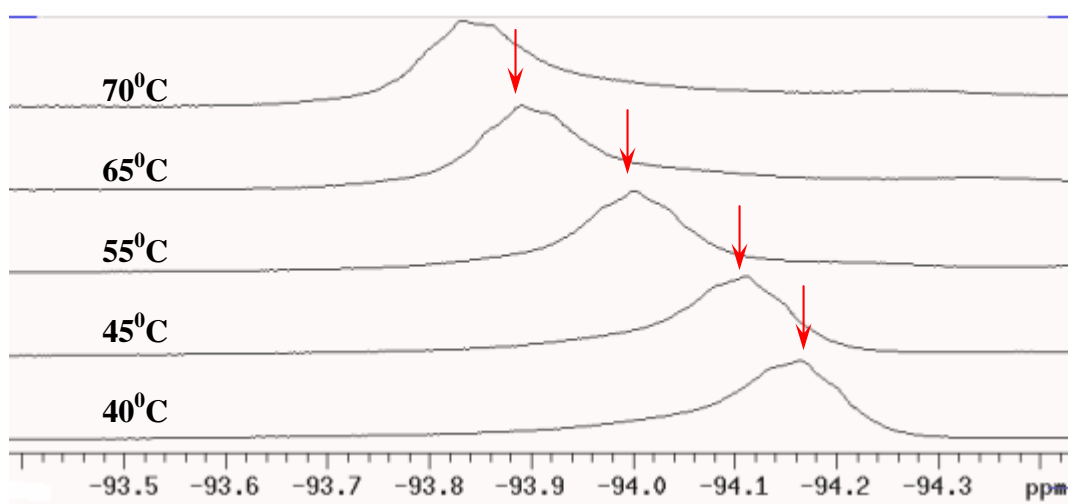


Figure 12 A deeper investigation between 93 - 95 ppm reveals a change in the curve, that is, the curve slants left as the temperature is increased.

Besides, the calculation of β -phase fraction from FT-IR results was not a precise quantitative analysis due to the measurement limit of the available FT-IR equipment. The absorption range for Equinox 55 is between 600cm^{-1} and 4000cm^{-1} . However, major characteristic peaks for β -phase and α -phase crystallites remain below 550, 510 and 532, respectively. Thus, the results are not satisfactory and not reliable. Hence, remaining crystallinity characterizations were employed with XRD and DSC.

4.3.1.2 XRD Measurements

According to the FT-IR and NMR results, a wide optimum range was chosen and decided as to be between $45 - 65^{\circ}\text{C}$. The crystallinity of the cast films were then analyzed via XRD to better view the crystal planes of different phases. The XRD measurements are also significant tools in the following chapters, when stretching of PVDF films is introduced.

As the XRD measurements illustrate in Figure 13 and Figure 14, α -phase is dominant over the other phases. This is mainly due to the surface characteristic of the PVDF films. α -phase tends to form its crystallites on the surface of the film when a temperature change is introduced. When the films are cast at different temperatures and taken out of the oven, all of them are quenched at -25°C . Formation of α -phase at the

surface of the film could not be avoided due to quenching and crystallites on the surface, hence, prefer to exist in the α -phase [30]. Yet, the samples should be quenched to avoid α - to β -phase transformation due to change in temperature in the whole film.

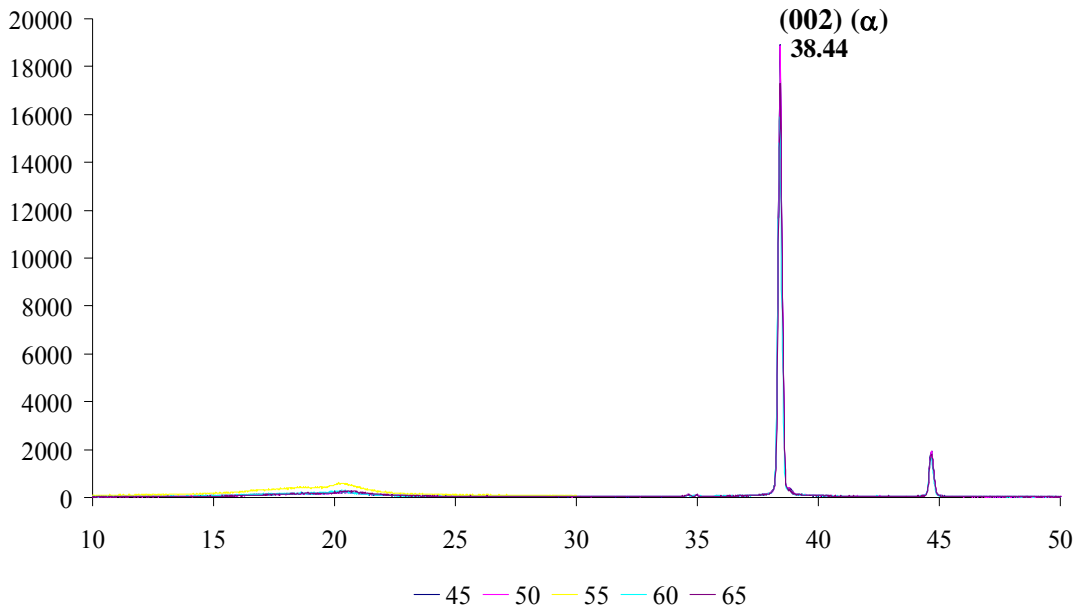


Figure 13 XRD data representing the crystalline peaks of the PVDF films.

As also stated by Priya and Jog [89], predominant presence of the α -phase was evidenced by the characteristic peaks at 2θ values of 18.6 (110) and 38.4 (002). Figure 14 illustrates the enlarged portion between 2θ values of 10 – 30. As followed from the figure, there are two distinct peaks typical to individual phases. This portion is critical in terms of the stretching of PVDF films, since it includes the characteristic β -phase peak. The existence of and the modification in the β -phase can be monitored from this critical region of interest. The presence of the β form of PVDF in these films is noteworthy because it is the form with required polarization state. The details of this portion will be given in the following chapters.

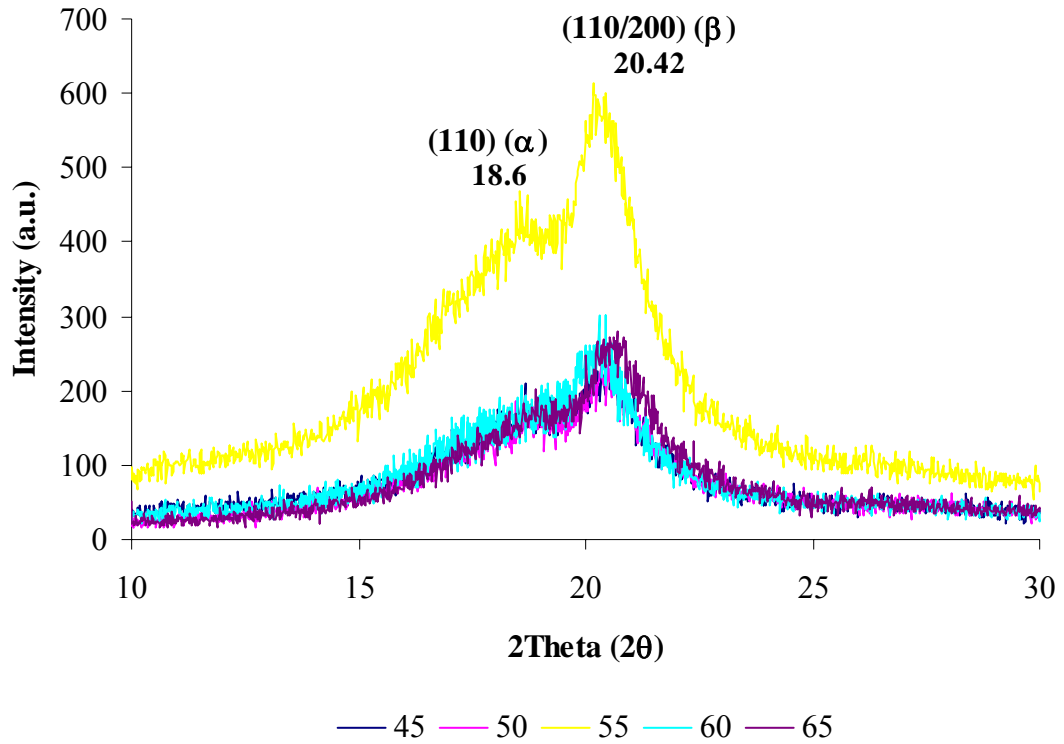


Figure 14 XRD data representing the crystalline peaks of the PVDF films between the 2θ values of 10 – 30.

4.3.1.3 DSC Measurements

Solution cast PVDF films were also characterized via DSC in order to determine their percent crystallinity and their melting points. It was previously shown that the melting point of the PVDF films exhibit a shift when their crystal phases are modified from α - to β -phase; hence the melting point determination becomes significant for each film produced via different process conditions [30].

Table 3 DSC results

Casting Temperature	Melting Point, T_m ($^{\circ}\text{C}$)	Area Under T_m ($\mu\text{Vs}/\text{mg}$)	Area Under T_m (Joule/g)	% Crystallinity
45	163.9	158.92	49.799	47.427
50	164.5	190.91	60.127	57.273
55	163.3	194.27	61.195	58.281
60	164.7	189.77	59.776	56.929
65	164.1	180.62	56.895	54.186

The melting points of the samples do not vary much when the standard deviation of the sampling is considered. One can fit almost a linear line on the melting point curve. Besides, it is significant to mention that these samples have a melting point of 164.1°C on the average.

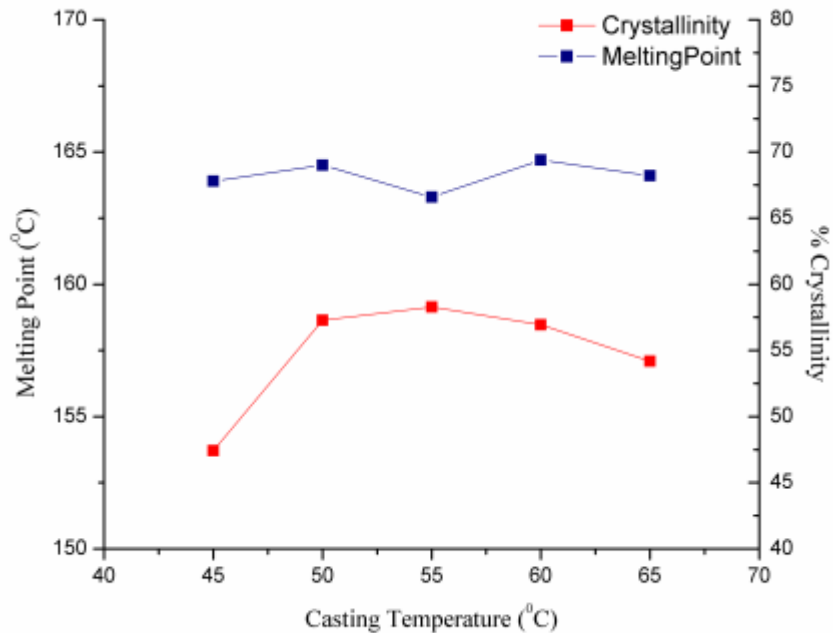


Figure 15 Melting point and % crystallinity values obtained from the DSC measurements.

In addition to the melting points, percent crystallinity values of the samples are also important in terms of polarization of the samples. The quality of the piezoelectric activity of the semi-crystalline PVDF films significantly depends on their crystallinity because the polarization is both a crystallinity and crystal phase dependent property. Since the polarization and the percent crystallinity are correlated, it is eminent to have samples with higher crystallite contents. In order to calculate the percent crystallinity of the samples, DSC data for 100% crystalline PVDF film is needed. It is previously mentioned that heat of fusion value for 100% crystalline PVDF is 105 J/g [1, 90]. By rationalizing the heat of fusion values, percent of crystallinity of each sample is calculated and given in Table 3. To monitor the effect of casting temperature on the crystallinity and melting point of samples Figure 15 is plotted. As the graph suggests, there is a slight decrease in the percent crystallinity of the samples with increasing casting temperature. Based on the data collected the peak value seems to exist at the 55^oC cast sample.

4.3.1.4 Mechanical Properties

Mechanical tests of the PVDF films were utilized in ALCAN Packaging, as mentioned previously. Measurements were obtained from three specimens for each casting temperature, so that an average value is examined. Table 4 tabulates the mechanical results as, ultimate stress (σ_u), stress at break (σ_b), strain at break (ϵ_b), and Youngs Modulus (E).

Table 4 Tensile test results of the pristine solution cast PVDF films.

Casting Temperature	σ_u (MPa)	σ_b (MPa)	ϵ_b (%)	E (MPa)
45	30.71±1.73	22.21	112.69	560.10±70.7
50	35.24±2.89	20.43	134.30	717.85±29.8
55	40.77±2.94	11.80	15.61	837.68±96.2
60	36.06±2.08	17.06	36.34	617.88±49.3
65	37.65±0.58	9.04	17.74	622.8±25.6

Figure 16 reveals that the casting temperature causes a slender decrease in the Youngs modulus of the sample; whereas there exists a slight increment in the ultimate stress values. Yet, 55⁰C sample also seems to possess better mechanical properties over the other samples. In addition to the sole mechanical properties, when the percent crystallinity versus maximum strain is plotted for these samples, it is observed in Figure 17 that the elastic modulus of the sample increases with the increasing percent crystallinity. This result is expected since fully crystalline materials exhibit higher elastic modulus than amorphous or semi-crystalline materials.

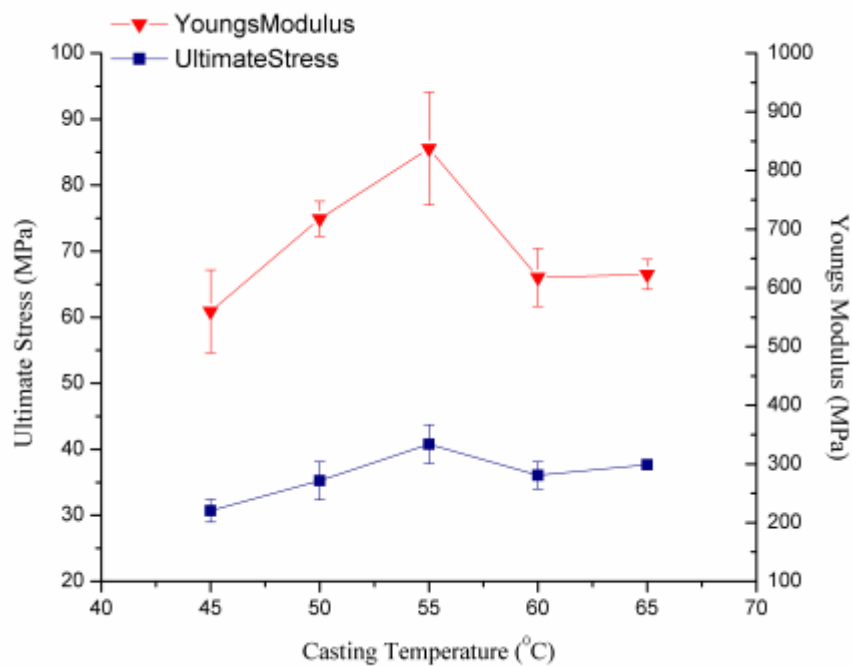


Figure 16 Ultimate Stress and the Elastic Modulus of the un-stretched solution cast films were plotted versus the process variable, casting temperature.

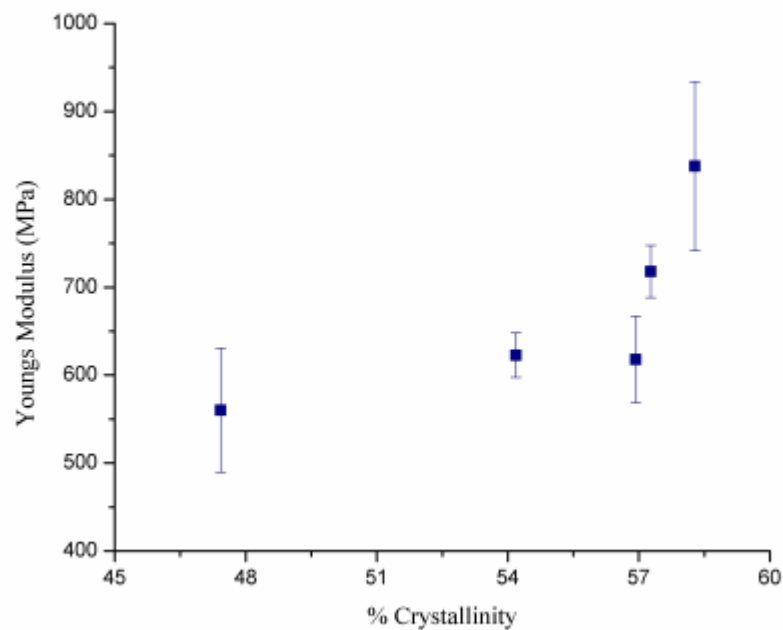


Figure 17 Correlation between percent crystallinity and Youngs modulus of the un-stretched solution cast films.

4.3.2 Stretched Solution Cast Films

Each pristine solution cast PVDF film is subjected to controlled elongation from its original length to 4 times of it. Stretching is utilized via the UTM at a control extension rate of 5mm/min and at a temperature of 80⁰C.

4.3.2.1 XRD Measurements

Each stretched film is characterized by XRD under same measurement condition with that of pristine films. Although there is a significant decrease in the α -phase crystallites, surface characteristics of the films did not alter much, thus we still observe the characteristic α -phase peaks in Figure 18.

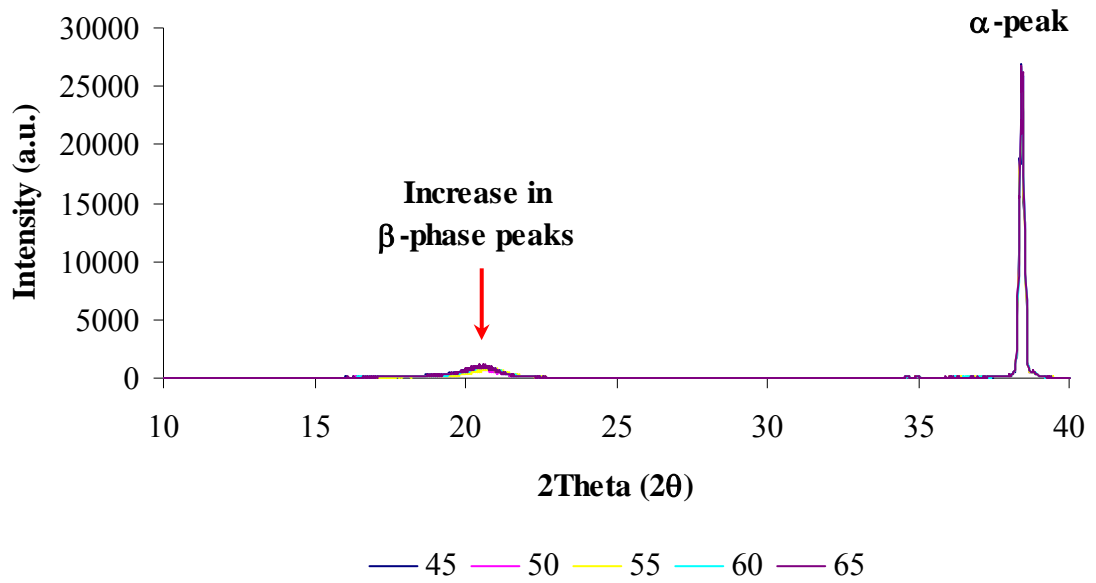


Figure 18 XRD Results of the stretched solution cast films

Rise in the intensity of the β -phase peaks are better observed between the 2θ region 10 – 30. Figure 19 monitors the diminishment of the α -phase peaks at this region. The results are similar to that of Pawlowski and Salimi et al. since they also mentioned the dominance of β -phase and non-existence of α -phase upon stretching the PVDF films [35, 90].

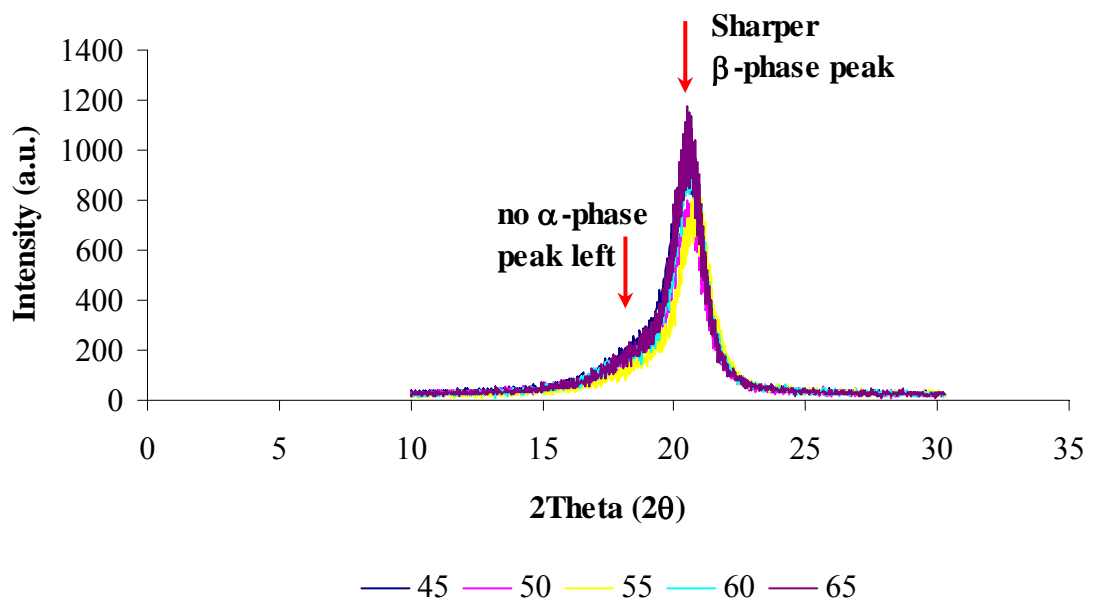


Figure 19 XRD data for the stretched solution cast films in the 2θ region 10 - 30.

Although the casting temperatures of the films are different, they all behave similar to each other and observe the phase change due to mechanical stretching. Figure 19 reveals an expected significant outcome that mechanical stretching introduces the α -phase to β -phase transformation. In short, when the films were elongated to 4 times of their original lengths under the given conditions in 4.2, β -phase content of the films increases.

4.3.2.2 DSC Measurements

Increase in β -phase formation in the elongated solution cast films was monitored from the XRD measurements. Yet, DSC analysis is significant in terms of exhibiting the molecular details regarding the crystallinity and melting point of the films.

DSC data corresponding to stretched films is given in Table 5 and Figure 20. Percent crystallinity values given in Table 5

Table 5 are relatively higher than that of un-stretched ones. There is an increase in the crystallinity of the samples on the average of $\sim 3\%$ with a maximum increase of $\sim 12\%$.

Table 5 DSC data for the stretched solution cast PVDF films.

Casting Temperature	Melting Point, T_m	Area Under T_m (μ Vs/mg)	Area Under T_m (Joule/g)	% Crystallinity
45	159.5	176.21	55.51	52.863
50	158.1	208.78	65.77	62.635
55	158.2	189.02	59.54	56.705
60	158.1	183.58	57.83	55.073
65	157.6	183.35	57.76	55.006

Furthermore, the melting point of the samples given in Figure 20 exhibited lower values than that of the un-stretched films shown in Figure 15. This verifies the formation and dominance of β -phase as previously observed by Benz et al. [1]. The average reduction in the melting points is approximately 5.8°C . This reduction proves the β -phase formation and the data attained from DSC verifies the XRD results and precisely reveals the increase in the β -phase crystallites.

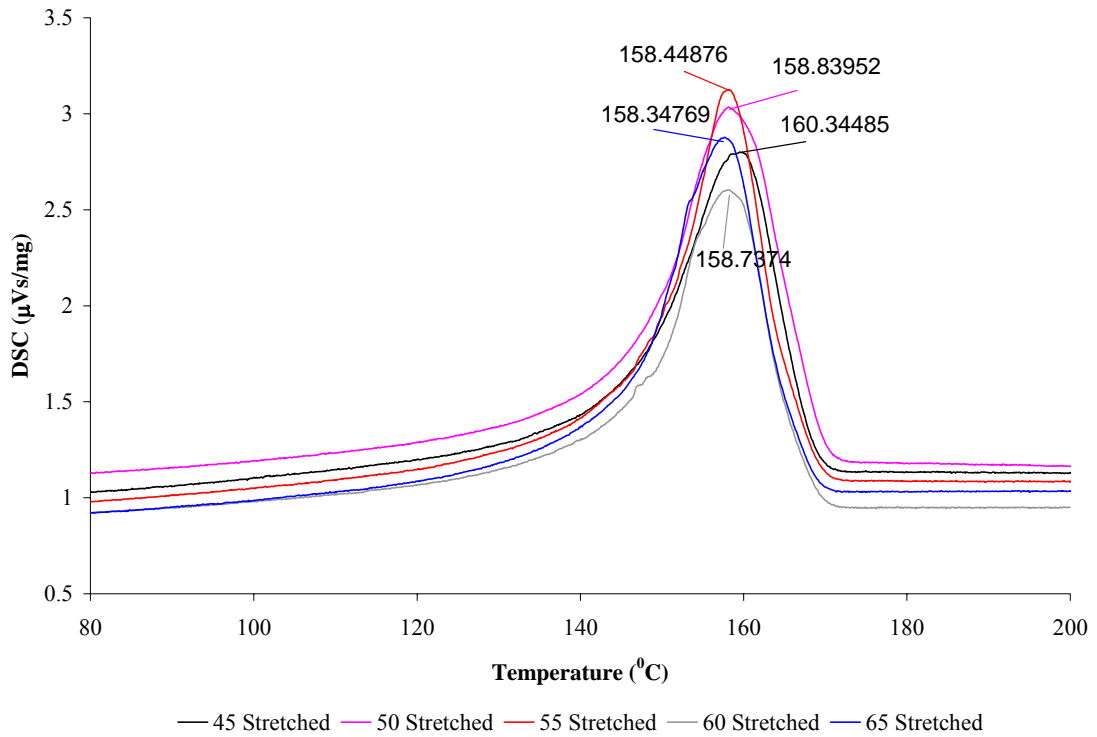


Figure 20 DSC results of the stretched solution cast films. Melting point values are lower than that of the pristine samples.

Effect of the casting temperature is lower in these samples since the major contribution to the melting points and crystallinity comes from mechanical stretching of the films. As the films were stretched higher crystallinity and modulus values are attained.

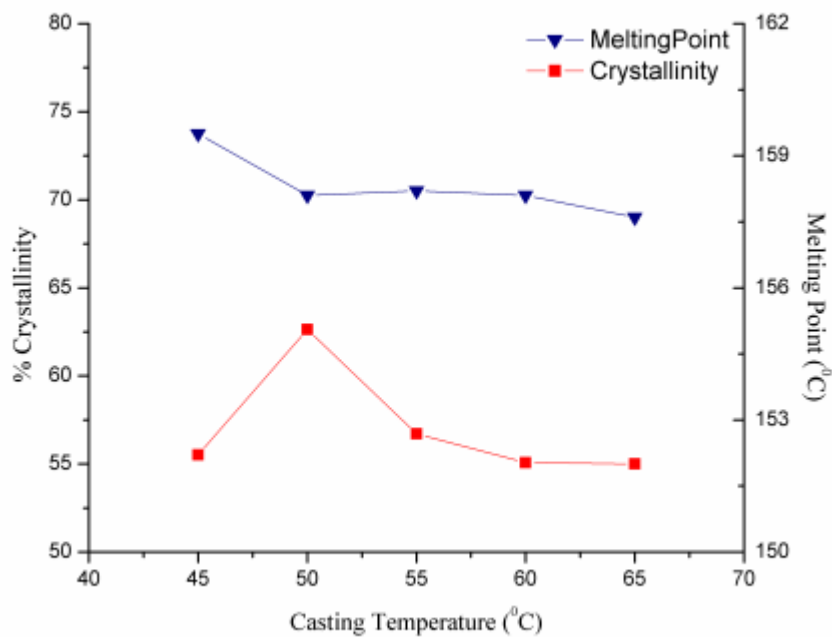


Figure 21 Melting point and percent crystallinity values after mechanically stretching the cast films.

4.3.2.3 Mechanical Characterization

Pre-stressing or pre-tension introduced systems carry higher loads than their original structures; therefore, ultimate strengths of the stretched samples are increased, as expected. Yet, they lost their elongation capability and exhibit very low strains.

Table 6 Mechanical properties of stretched solution cast PVDF films.

Casting Temperature (°C)	σ_u (MPa)	σ_b (MPa)	ϵ_b (%)	E (MPa)
45	81.14±10.45	38.65	50.86	397.15
50	86.49±7.30	43.27	53.27	408.28
55	67.08±25.31	25.05	34.44	344.35
60	71.23±5.24	48.40	24.37	323.40
65	66.82±8.57	14.62	14.50	372.18

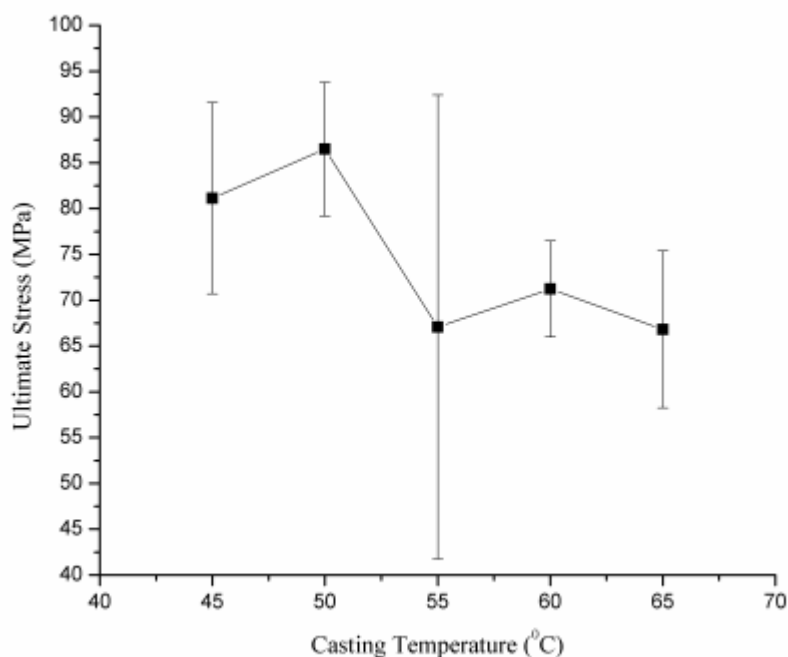


Figure 22 Ultimate stress observed on the stretched solution cast PVDF films.

As Figure 22 suggests, the standard deviations in the tests of the samples are very high; and not appear to be suitable to draw conclusions. The variance in the results is assumed to be due to the defects in the films that led to non-uniform thickness while exposed to high amount of permanent deformation at elevated temperature. In other words, when the films were produced by solution casting, there may be thinner points along the film thickness which may work as defects. After stretching the films, these thin regions are likely to become thinner and cause the film to resist lower stresses. Hence, this non-uniformity in film thickness is thought to be the major cause of this odd effect in Figure 23. Besides the ultimate stress values, it is also significant to point out the relation between strain values and percent crystallinity. Strain values do not follow the crystallinity values, which is also attributed to non-uniform defect growth in the film –which should be analyzed as a future work.

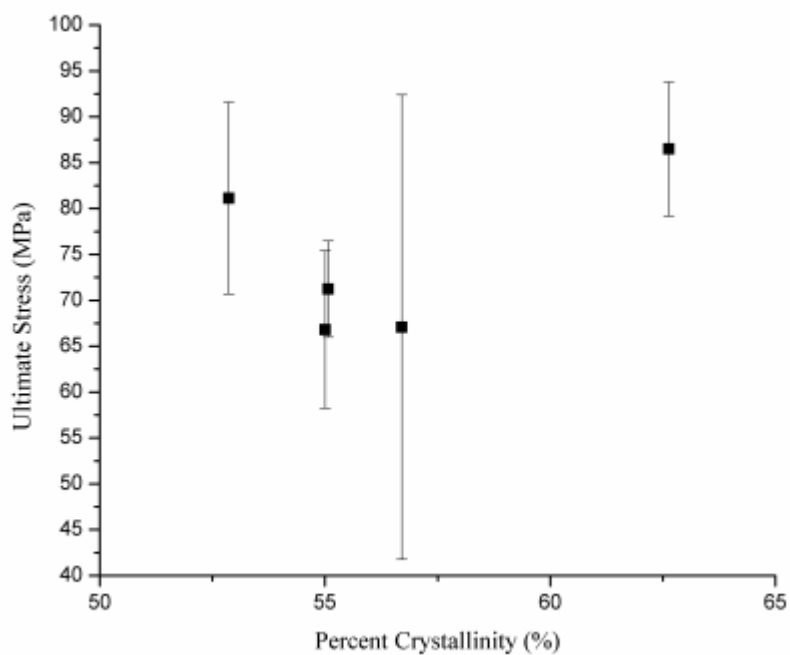


Figure 23 Relation between percent crystallinity and the ultimate stress exerted on the stretched films is plotted.

4.3.3 Comparison Between Stretched and Un-stretched Solution Cast PVDF Films

Stretched and un-stretched films should be compared in terms of the β -phase content in their crystal structure so that the effect of and necessity of stretching the samples can be emphasized.

4.3.3.1 XRD Measurements

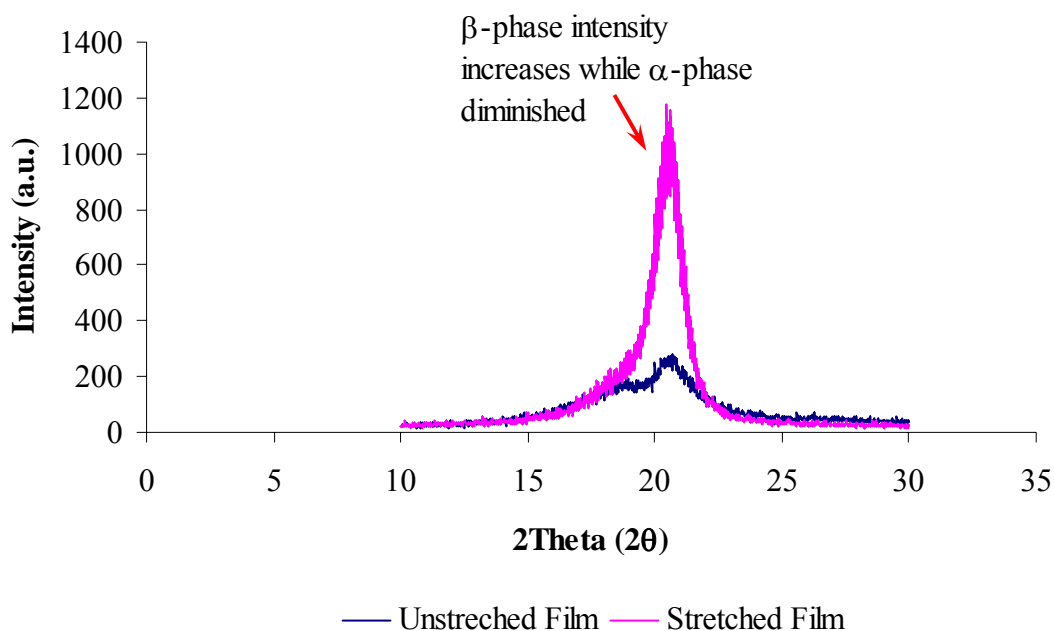


Figure 24 Comparison between stretched and un-stretched solution cast films

As it is given in Figure 24, there exists both an amorphous to β -phase and α -phase to β -phase transformation, which is also verified by the increase in the percent crystallinity of the films. In short, stretching introduces an increase in the β -phase intensity due to the transformation of crystallites and amorphous region

4.3.3.2 DSC Measurements

Melting points of the stretched films are lower than that of the un-stretched ones, which is consistent with the previous studies. This shift ensues due to the change in the crystallites towards the all-trans β -phase. The β -phase crystals have a lower density; therefore, an increase in the content of β -phase –due to stretching- drops the melting point of the polymer.

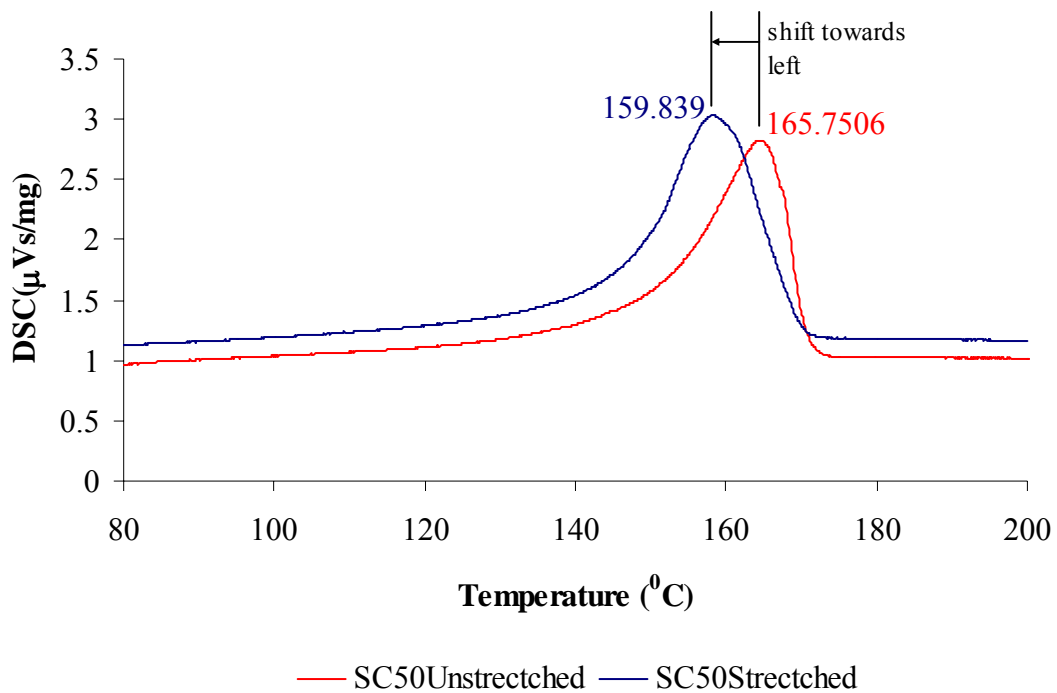


Figure 25 Comparison of DSC results of stretched and un-stretched solution cast films.

4.3.3.3 Mechanical Strength

Mechanical strength of the two stretched and un-stretched film systems is significantly affected by the elongation amount of the films. As the strain induced into a film is increased, amount of polymer chains that are aligned also increases. Thus, the film carries higher loads with a lower strain, which is called strain hardening. Yet, the film loses its ductility and becomes brittle. On the other hand, for more conclusive comparisons in the mechanical behavior, need for a casting procedure or equipment that ensures the uniformity of the films should be noted.

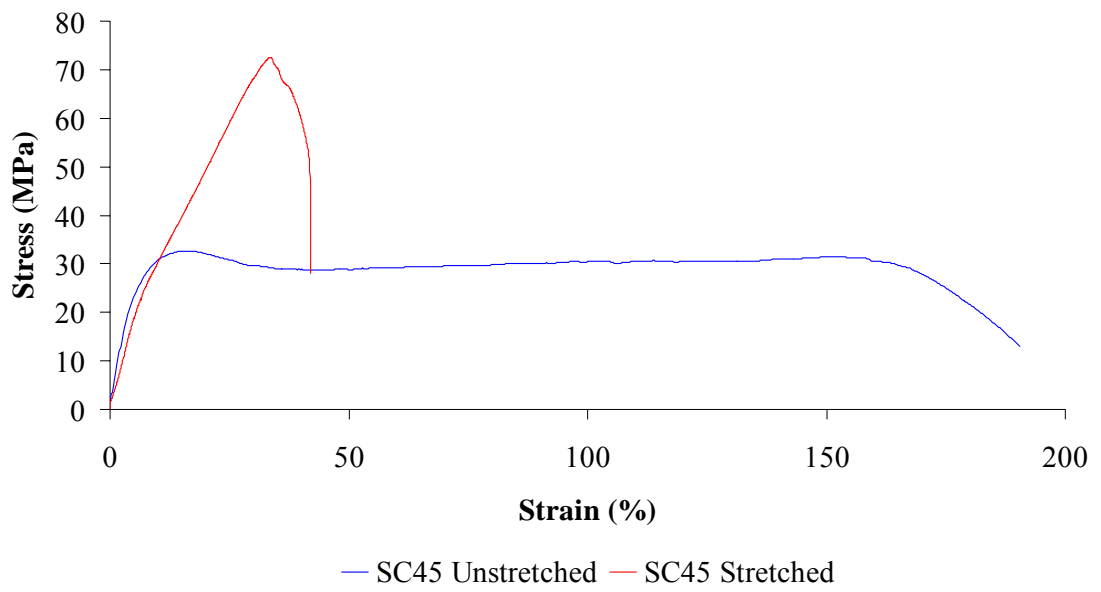


Figure 26 A representative tensile strength graphs to monitor modification through stretching the samples.

5. PVDF FIBER MATS

5.1 Process: Electrospinning of Polymer Solutions

Electrospinning (also called electrostatic fiber spinning) is a process to produce continuous nano- or micro-scale fibers from both synthetic and natural polymers. Electric forces are used to form fibers from material solutions or melts in the electrospinning process. Studies on electrically driven liquid jets were initially started in 19th century, and electrospinning of polymer fibers was first patented by Formhals in 1934 [91]. The main principle in electrospinning as defined by Doshi and Reneker is to generate a charged jet of polymeric solution by applying an electric field [36, 39]. As the jet travels in the air, the solvent evaporates and a charged fiber is left behind which can be collected on a grounded plate (collector). Through this process, mostly mats of randomly oriented fibers with large surface to volume ratio as well as various fiber morphologies and geometries are fabricated from several polymer solutions, as noted in Deitzel et al. [92]. The goal of this part of the work is to determine if the electrospinning process has a promise to improve the electromechanical performance of PVDF in the future application of interest, MAV wing.

In home-made electrospinning set-up, as depicted in Figure 27, a polymer solution is placed into a syringe that has a millimeter size nozzle and the nozzle is subjected to an electric field of several kilovolts between 5 to 15kV. The syringe is placed in a syringe pump (Univentor 801 Syringe Pump and New Era NE-1000 Syringe Pump) by which the rate of the polymer flow is continuously controlled without disturbing the set-up, via an RS232 unit attached to both the set-up and a computer. Under the applied electric field, the polymer solution is ejected from the nozzle to the collector due to high electrical force apparent on the polymer droplet at the tip of the nozzle. As the polymer jet travels in air the fiber diameter reduces significantly due to loss of the solvent in air and the stretching on the fine fiber as a result of the electrical force. The randomly

oriented ultra fine fibers collected on the screen produce an unexpectedly high surface area to volume ratio and are of interest for many application ranging from textile to composite reinforcement, sensors, actuators, biomaterials, filter and membrane technology [38].

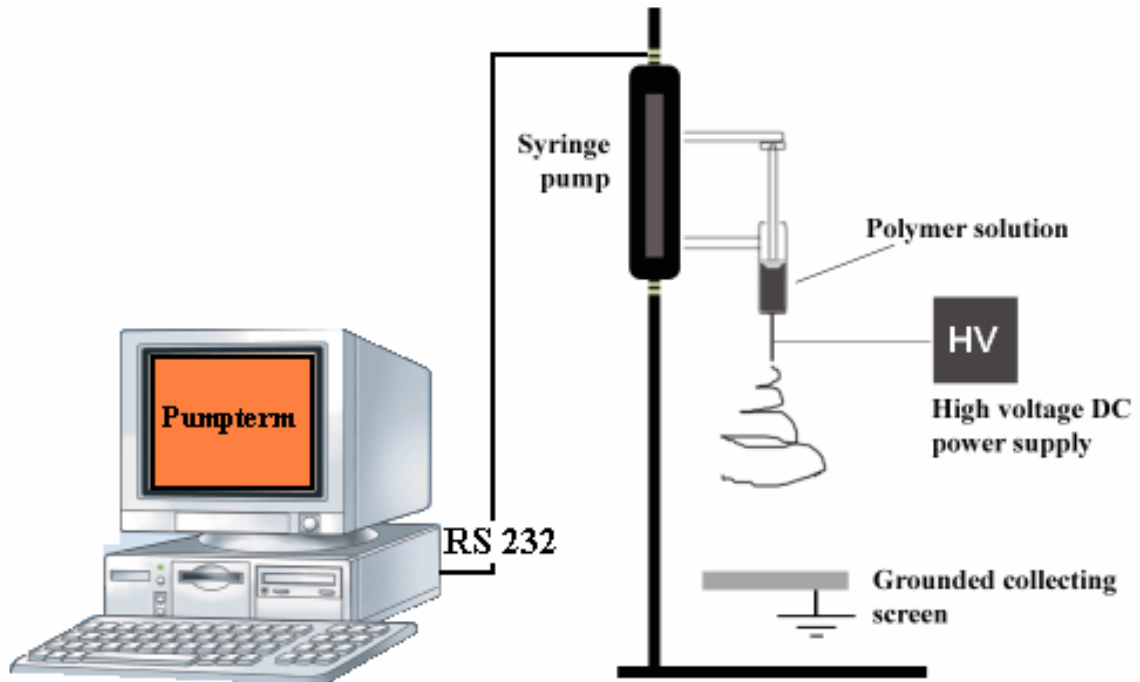


Figure 27 Schematic representation of the computer controlled electrospinning setup.

Up to 100 syringe pumps can be independently controlled via one unit

One of the advantages of the electrospinning process is that it can be performed on polymers both in solution and in the melt. In the previous works, Baumgarten formed microfibers by using the acrylic resins dissolved in Dimethylformamide [37]. Larrondo and Manley produced polyethylene fibers [93]. Moreover, Zacharides and Porter obtained high modulus fibers from both Kevlar and poly(p-phenylene terephthalamide) [94]. Kattamuri and Sung observed polycarbonate fibers to via this process [95]. Bombyx-mori silk fibers are produced by Sukigara et al. for textile applications [96]. Mo and his colleagues produced P(LLA-CL) nanofibers to be used in muscle cells and endothelial cell proliferation [97]. Poly(vinylidene fluoride) fibers were electrospun to be utilized as a micro air vehicle wing material [98].

The electrospinning setup used in the formation of PVDF fibers is given in Figure 27. It is composed of a GAMMA high voltage power supply, PUMPTERM Z100 syringe pump, and a homemade conductive collector screen. The PVDF solution prepared with different solvent ratios is placed in a syringe and a range of 8 to 12kV voltage is applied to the polymer solution to produce PVDF fiber mats. The details will be provided in the following sections. Next, is to introduce the methodology employed in the process development and optimization.

5.2 Process Optimization via Response Surface Methodology

5.2.1 Linear Regression

In practice, engineers are interested to solve problems involving sets of variables when it is known that there exists some inherent relationship among the variables. It may be of interest to develop a method of prediction, that is, a procedure for estimating the value of a response for various levels of the variables affecting that response. For instance, the tar content in a chemical process is related to the inlet temperature of that process. However, it may not be the only effective variable on the tar content. The tar content in this example is a natural *dependent variable* or *response* of that system. Besides, the inlet temperature is the natural *independent variable* or *regressor* of the same system. A reasonable and simple relationship between these two variables can be a linear relation,

$$Y = A + Bx \tag{5.1}$$

yet, this linear relationship may not be deterministic (exact), that is, a given value of x does not always give the same value of Y . The concept of regression analysis deals with finding the best relationship between Y and x , quantifying the strength of that relationship, and the use of methods for prediction of the response values to the given values of the regressor x .

The analysis of relation between x and Y in an experimental setting typically requires the statement of a statistical model. A model is often used by a statistician as a

representation of an ideal that essentially defines how we perceive that the data were generated by the system in question. The model must include the set of data involving n pairs of (x,y) values. Since the relationship is not deterministic, one must bear in mind that the value y_i depends on x_i via a linear structure that has a random component involved. The basis of the statistical model is to relate the value of the random variable Y with the move of the x and the random component, which can be given as,

$$Y = A + Bx + \varepsilon \tag{5.2}$$

where, ε is often called the random error, or random disturbance. It must be kept in mind that A and B are unknowns and they must be estimated by the observed data. Consequently, ε values are never observed actually and thus the true regression line can never be drawn. Only the estimated line of the system is drawn (Figure 28) [99-101].

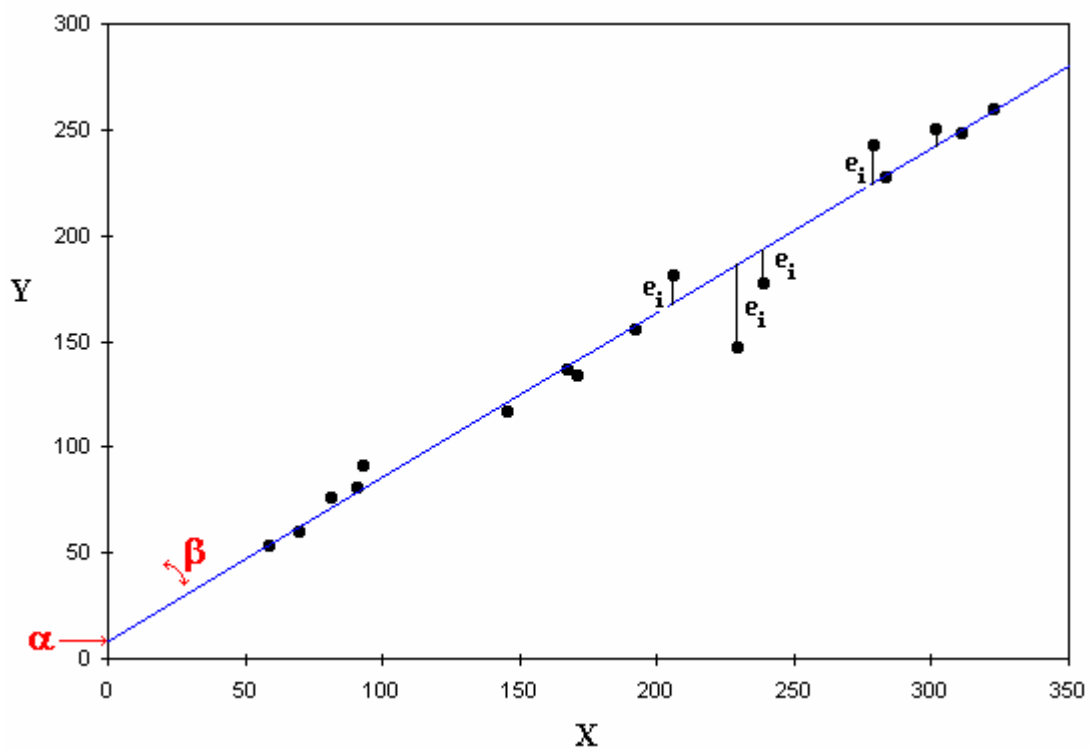


Figure 28 Linear regression fitted on the 17 sample data.

5.2.2 Method of Least Squares

Before getting an insight of the method of least squares, the concept of residual should be defined. A residual is the error in the fit of the model $\hat{y} = a + bx$ where a and b are estimates of A and B , respectively. When a set of data is given and a model is fitted, $\hat{y}_i = a + bx_i$, i^{th} residual, e_i , is given as $e_i = y_i - \hat{y}_i$ for each measured data and the corresponding value in the fitted model (Figure 28).

The Least Squares is a mathematical optimization technique to fit an empirical formula/function approximating the given series of measured data. The A and B coefficients in the fitted model function should be estimated as a and b such that the sum of squares of the residuals is a minimum. The residual sum of squares is often called the sum of squares of errors (SSE) about the regression line and simply denoted by SSE. The least squares method constructs a line that minimizes the SSE of vertical deviations from the points to the fitted line [99-101].

5.2.3 Experimental Design

An experimental work is usually constructed to investigate the performance or outcome of a process and can schematically be represented in Figure 29. There is an input to the experiment and a single or several outputs from that system. Some of the process variables are controllable, whereas some are not. For instance in this study, the humidity of the laboratory environment can not be controlled, whereas, the applied voltage in the electrospinning setup can be controlled. Thus, the objective of the defined experiment is to monitor the effect of these independent factors.

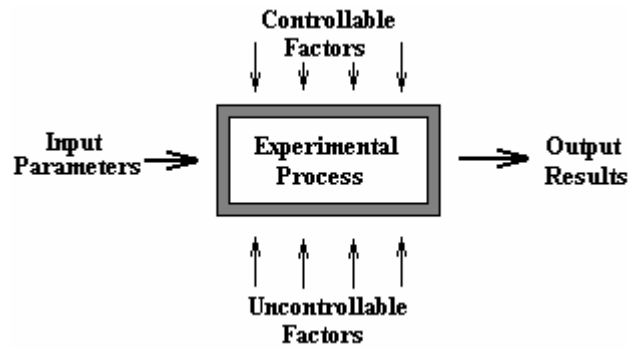


Figure 29 Schematic representation of an experimental process. Adapted from [100]

There are several methods to observe the effect of process parameters. One of the most frequent ones among the engineers and scientists is the one-at-a-time approach. This approach includes the observation of the effect of each factor separately and hence is not able to reveal the interaction and combined effect of the parameters on the analyzed response [101].

Another method is called the best-guess-approach in which the experimenter guesses each data point randomly to reach a targeted value. Although this approach is very common, it is risky in terms of the initial guesses, that is, if the initial guesses are at the far end of the desired experimental space, it will take longer time and effort to reach the optimum response value. Additionally, suppose the guesses directed the scientist towards a reasonable result, yet, it cannot be said that it is the optimum one in that experiment range [101].

Constructing a factorial experiment is a systematic approach to deal with multiple factors. In this method, experiments are carried out within a combinatorial matrix of the levels of all parameters; allowing to monitor both the individual effects and the interaction between different parameters on the targeted response. For instance, consider the diameter of the electrospun fibers as the response, and voltage and concentration as the two factors affecting the fiber diameter. In the simplest factorial design, 2-level factorial design, the experimenter constructs a cuboidal domain (a square in a two-variable case) as represented in Figure 30 and tests the black dotted data. After experimenting only at the vertices of the domain, the data represents the trends of outcome over the design space and an Analysis of Variance (ANOVA) may be applied in order to judge the individual and interactive effects of variables or parameters.

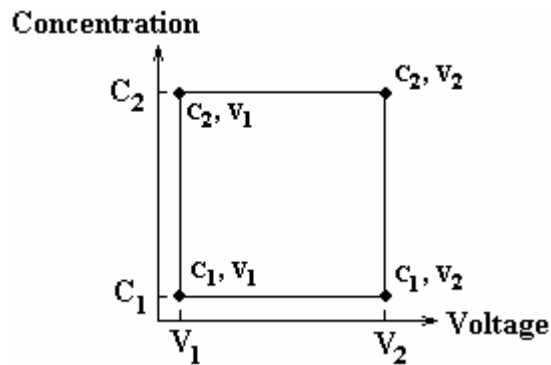


Figure 30 2 Level Factorial design for the change in fiber diameter. Voltage and Concentration are the two different factors experimented at two levels.

As noted above, the particular type of factorial design given in Figure 30 is the two level factorial design, 2^2 factorial design, at which two factors are tested at two different levels, for instance, lower level and upper level. If a tertiary level, say the mid-level, is inserted in the design domain, then the design becomes a three level factorial design, and represented as 2^3 factorial design for two variable case.

Response Surface Methodology (RSM) is a useful and extended application of design of experiments that also employs regression. Briefly, experimental design is used to characterize or optimize a process with the predictive response surface obtained by the regression analysis. Screening experiments is a general method in characterizing a process, by which the critical process parameters are identified, generally by factorial experimental designs. In addition, RSM is one of the common tools in the experiment-based optimization. To locate an optimum point of any process, typically experimental designs more involved than 2-level factorial design should be constructed so that curvature of the response is gathered. Face-centered Central Composite Design (FCCD) for instance is a commonly used experimental design that can also characterize curvature. Once the optimum point is achieved, an empirical model of the process should be formed to attain a precise estimate of the optimum process conditions. This approach of process optimization is referred as Response Surface Methodology.

As mentioned earlier, Response Surface Methodology is a set of mathematical and statistical techniques that are useful for the modeling and analysis of problems in which

a response of interest is influenced by several variables and the objective is to optimize this response. If the experimental outcome is denoted as

$$y = f(x_1, x_2) + \varepsilon \quad (5.3)$$

where ε represents the error observed in the response y and the expected response is denoted by $E(y) = f(x_1, x_2) = \eta$, in other words, the true response function is the true mean response represented as

$$\eta = f(x_1, x_2) \quad (5.4)$$

The response surfaces which approximates the true response function or true mean are usually represented by plotting either a contour plot or a 3D surface of the response variable over the design domain, as given in Figure 31 if the problem is in two variables. The response surface functions are either linear first-order-model functions or higher-order-polynomials, e.g. second-order-model. The model with the best statistical results and most reasonable to the experimenter's experiences is chosen as the RS model and plotted (Figure 31).

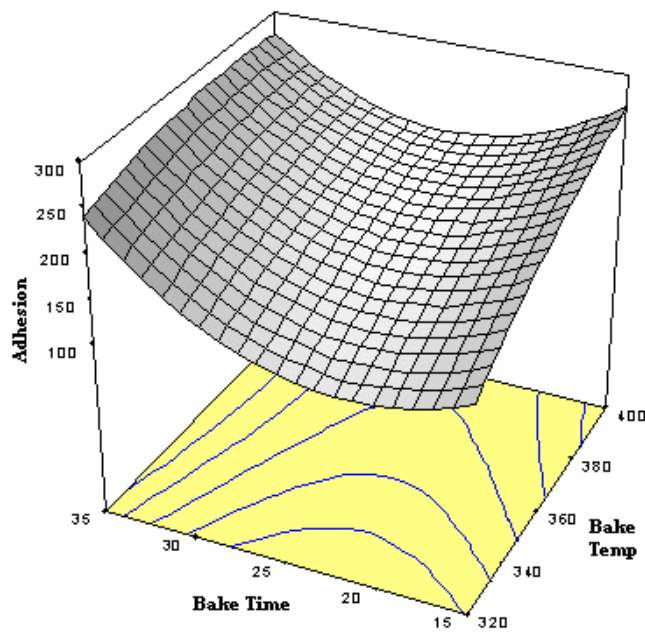


Figure 31 A representative plot of an RSM example. Baking temperature and duration are the factors affecting the adhesion (response) of the material.

5.3 Characterization Tools

Similar characterization methods with the solution cast PVDF films were employed. XRD, DSC and mechanical tests were utilized to determine the crystallinity and strength of the fiber mats. NMR and FT-IR measurements were not taken into account since no temperature modification in the solutions and samples were exploited.

5.4 Results and Discussions

5.4.1 Design of Experiments for Applicability

Poly(vinylidene fluoride) obtained from Alfa Aesar has a molecular weight above 500kg/mol, and a melt viscosity of 23500-29500 poise (230°, 100/sec). N,N-Dimethylformamide (DMF) and Acetone are obtained from Merck Chemicals. According to trial experiments and verifying them with literature, PVDF and DMF solutions were prepared in 20% concentrations weight by weight (w/w) solutions to produce PVDF fibers in the desired homogeneity and geometry. It is also observed from the previous studies that electrospinning of PVDF is rather complex than some other extensively electrospun polymers such as Polyacrylonitrile. The complexity and difficulty to produce uniform PVDF fibers comes from its solvent. DMF has a low solvent volatility, which typically leads to the formation of wet fibers and droplets on the collector screen. Since the acceptable fiber quality described as dry fibers with uniform geometries, a modification in the solvent type should be sought. The solutions were then further prepared by two solvents introducing opposite effects on PVDF: DMF, dissolves PVDF, and, Acetone, precipitates the PVDF. On the other hand, acetone has a very high volatility which speeds the evaporation of the solvent thus results in more uniform mats. Three different solutions were prepared in different Acetone/DMF ratios: 0%, 25%, and 50%. Yet, the solution concentration was kept constant in 20% w/w, PVDF/(Total PVDF+Solvent Mixture).

The electrospinning parameters for the PVDF fiber formation were determined according to previous works on PVDF and general polymer systems and the preliminary study in the Sabanci University Polymer Synthesis Laboratory [102]. Applied voltage

range is decided between 8 – 12kV and the collector screen distance is kept between 15 and 30cm. Then, a three level factorial experimental design is constructed to utilize the minimum number of experiments in the desired parameter range to observe the PVDF fiber geometries and morphologies. The experiment points in the desired region are given in Table 7.

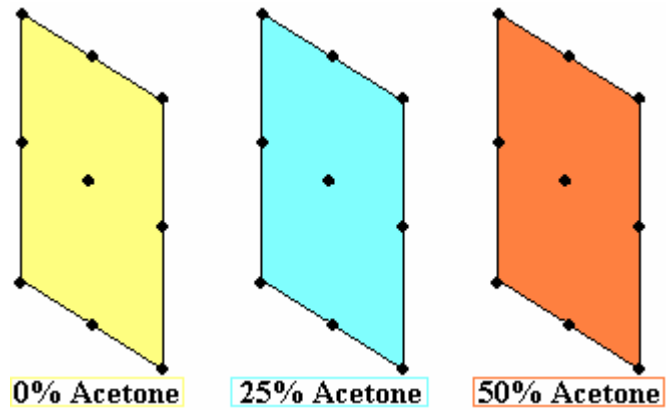


Figure 32 Experimental design region for three different solution ratios. 9 experiments were conducted at each solution mixture design space.

Table 7 Experiment points in the region of interest

Sample Number	Applied Voltage	Collector Distance
1	8	15
2	8	22.5
3	8	30
4	10	15
5	10	22.5
6	10	30
7	12	15
8	12	22.5
9	12	30

Each solution is experimented in these 9 points as represented in Figure 32 and each sample at each data point is imaged by LEO SUPRA 35VP Scanning Electron Microscopy (SEM). SEM images exhibit the uniformity and homogeneity of the PVDF fiber mats. Each point is expected to reveal different fiber and mat structure.

The electrospun PVDF fiber mats are imaged under SEM and a normal digital camera to monitor the fiber and droplet effect on the macroscopic structure of the mats. Some of the mats were expected to be more uniform and homogenous than others, say the “good” mats, and their processing conditions are of particular interest for further applications. Each of these *good* mats of PVDF fibers were characterized to observe their fiber diameter, crystallinity, and mechanical strength. The relationship between the electrospinning parameters and fiber diameters, crystallinity, and mechanical behavior are the outcomes of this part of the study.

Electrospinning of PVDF is a difficult process due to the solubility characteristic and ferroelectricity of the polymer. When a high electric field is applied onto PVDF the dipoles in the polymer structure is altered and the viscosity of the polymer changes. In addition, solvents that can dissolve PVDF have high boiling points; hence, evaporation during spinning of the polymer needs more time or distance. If the polymer is not spun in a correct range of electrospinning parameters the solvent evaporates on the collector screen instead of during spinning while the solution jet travels in the air. This appears to cause additional stresses onto the as spun mat and the mat folds onto itself due to the change in its crystal structure while the solvent is evaporating. These electrical induced deviations and structural change properties of PVDF make it a difficult polymer to process with electrospinning. An accurate range of material and process conditions should be achieved in order to attain physically applicable polymer mats.

Our initial trials showed that the viscosity of the PVDF/DMF solutions significantly affect the morphology of the mats. No working/production region of concentration below 20% by weight was found to successfully electrospin PVDF fiber mats. Solution concentration below 15% produced droplets and beads. However, when the polymer concentration was increased above 18%, fibers were begun to form, yet, with non-uniform geometries and 500nm in diameter on the average. Finer diameters of polymer fibers are attractive for scientists; yet, handling is a major problem for these fine fibers. Besides, micron-scale fibers are expected to be favorable to ease in handling in future application of interest, MAV wing. Moreover, higher concentration samples than 20% are difficult to work with due the evaporation problem at the tip of the syringe during electrospinning. Higher concentration solutions dry at the tip and abolish the spinning process.

These justify the choice of 20% concentration by weight throughout this study. There still exists a critical problem, uniformity despite the micron size fibers. Hence, Design of Experiments within the context of response surface methodology was decided to be used as an approach to monitor the morphology and geometry of the fibers.

There are several other factors affecting the electrospinning of PVDF solutions such as solvent type, applied voltage, current of the power supply, collector distance, temperature and humidity of the environment. From these factors, several that thought to be the more critical ones were chosen to observe their effects on the PVDF mats. Solution concentration was kept constant at 20% because no finer than micron scale fibers were targeted and a higher concentration has a very high viscosity which complicates the solution characteristics as mentioned previously. The environmental conditions are difficult to control but the fabrication was made at the same laboratory with the same apparatus. Three critical parameters to test were decided as the solvent type and mixing ratio of the solution as the material-based parameter, applied voltage and collector distance as the process-based factors. A three level factorial design as schematically represented in Figure 33 was considered in order to test these three experimental factors in a broader range with more precision. Since it was difficult to observe the effects of the parameters in a fourth dimension; we utilized three two-variables 3-level factorial designs each with voltage and collector distance as the two base factors. Each of those designs is dedicated to a different solvent mixture ratio as represented in Table 8 and Figure 33.

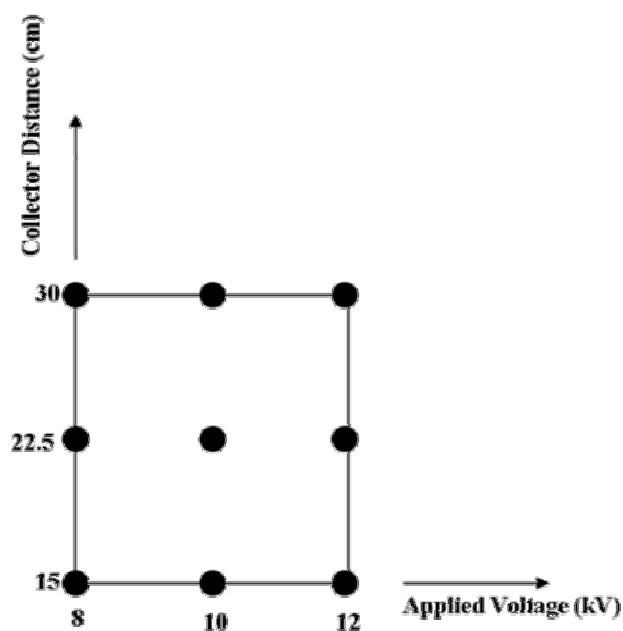


Figure 33 Two-variable 3-level factorial design. Applied voltage and the collector distance are the parameters of interest. This factorial design is applied at all solvent mixing ratios.

Table 8 3-level factorial design constructed for the electrospinning of PVDF

Solvent Mix 1		Solvent Mix 1		Solvent Mix 1	
Acetone/DMF: 0		Acetone/DMF: 0.25		Acetone/DMF: 0.5	
Voltage (kV)	Distance (cm)	Voltage (kV)	Distance (cm)	Voltage (kV)	Distance (cm)
8	15	8	15	8	15
8	22.5	8	22.5	8	22.5
8	30	8	30	8	30
10	15	10	15	10	15
10	22.5	10	22.5	10	22.5
10	30	10	30	10	30
12	15	12	15	12	15
12	22.5	12	22.5	12	22.5
12	30	12	30	12	30

5.4.1.1 Results for the Visual Applicability Test

The uniformity of the fiber mats is vital in terms of applying the mats on a specific surface. The mats should be flat and stress-free to keep their as-spun shapes, and the shape of the mats should be checked. Hence, the mats were imaged by a digital camera to ensure their uniformity and this inspection was defined as the *Visual Applicability Test*. As defined, the mats should be uniform and flat, having no buckling or folding over them indicating the solvent evaporates uniformly and the mats have no residual stress, thus keeps their spatial geometries and dimensions.

The samples given in Figure 34 depict the two types of mats produced. Mats on the left hand side are from the DMF only and 25% Acetone/DMF mixture samples, where as the mats one the right are 50% Acetone/DMF mixture samples. As the figure suggests, right samples are much more uniform, therefore the samples on the right are possible candidates to be applied on a specific surface; and these possible candidates are defined as *applicable mats*. Besides the standard camera images, it is also significant to observe the fiber quality in the *applicable mats*, which was tested via SEM imaging of the mats. As the Figure 35 suggest, applicable mats are composed of uniform fibers instead of beads and droplets like in the *non-applicable mats* given on the left hand side of Figure 35. Since the applicable mats are composed of uniform fibers, it is possible to coat any skeletal structure with these fibers as once tested with an MAV skeletal structure shown in Figure 36. Polymer fiber spun on this wing skeleton perfectly kept the shape of the wing. When a flight test was conducted by throwing the wing from the second floor, it smoothly flew over a long distance.

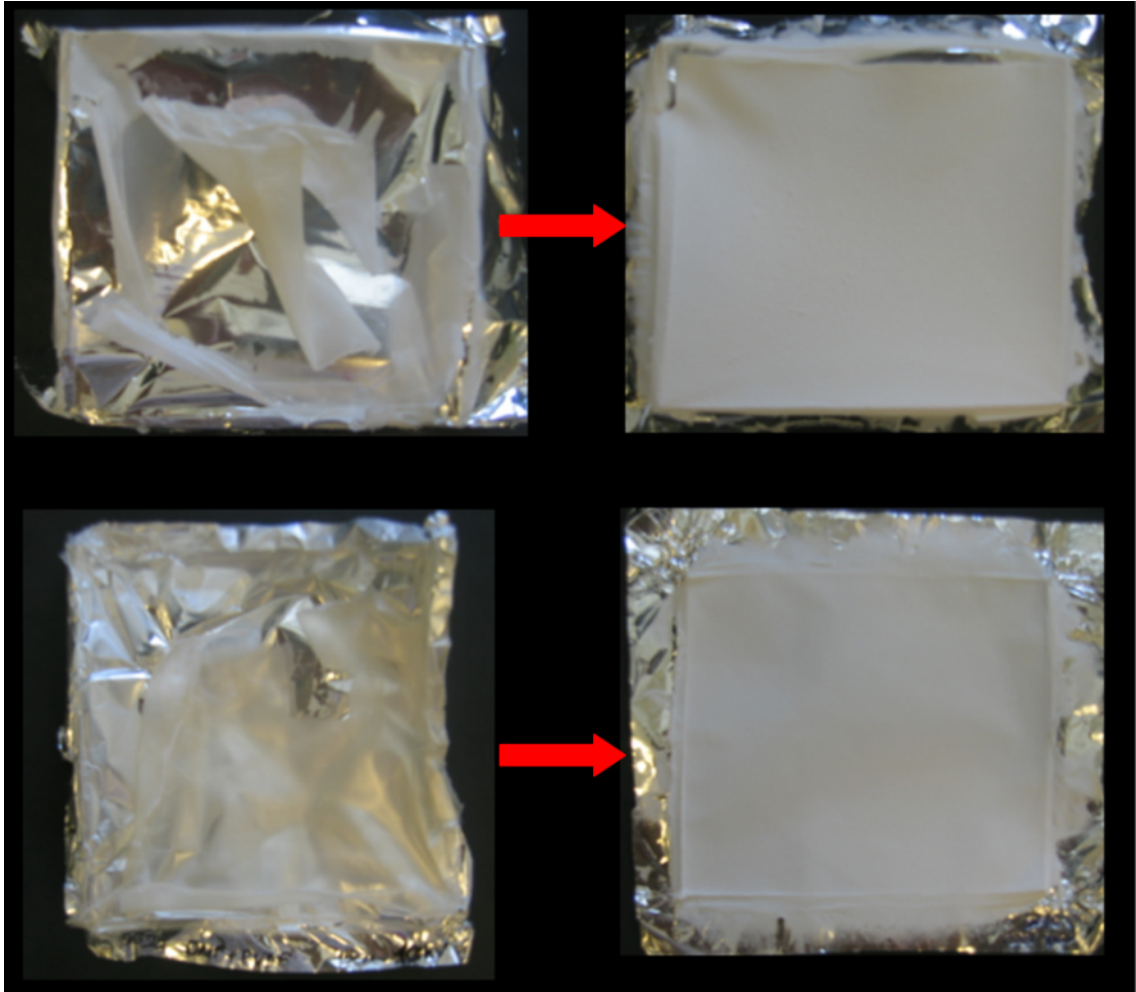


Figure 34 Image electrospun samples with non-applicable (left) and applicable mat morphologies (right).

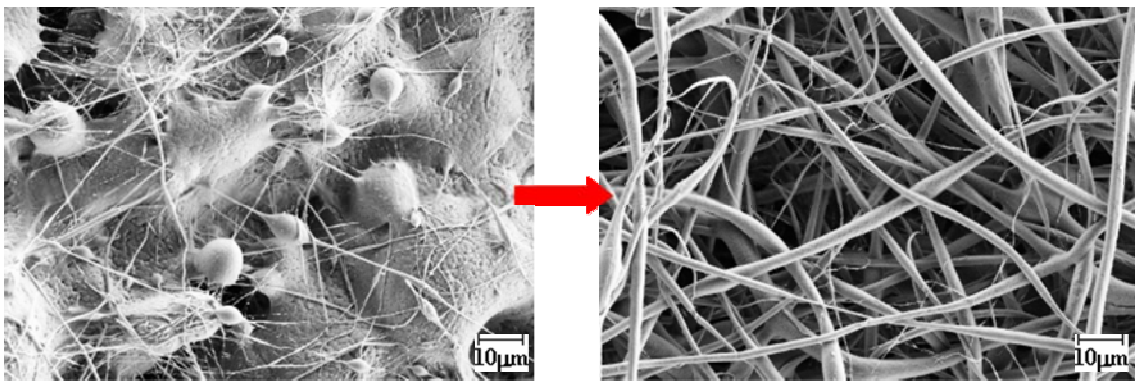


Figure 35 SEM images of the non-applicable (left) and applicable fiber mats (right).

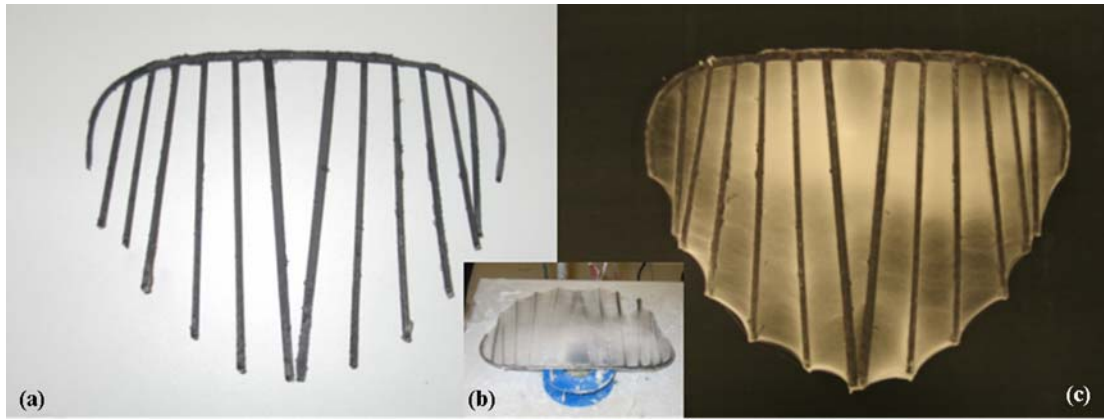


Figure 36 Fibers spun on an MAV skeletal structure made up of Carbon/Epoxy composite. The polymer fibers in micrometer scale are spun on this wing and perfectly kept the skeleton in shape (wing skeleton was adopted from Ifju et al. [103]).

5.4.2 Prediction of Fiber Diameter via Response Surface Methodology

Investigation of the electrospinning process and their effects on the PVDF fiber morphology, mat applicability and fiber diameter require a number of experiments defined in the previous section. The planning and analysis of these experiments were performed within the context of Response Surface methodology. Response surfaces (RS) are in fact to approximate numerical or physical experimental data by an analytical expression that is usually a low-order polynomial. Determining a mathematical approximation model that best fits the data which is collected/generated from the set of experiment points of the crucial step of Design of Experiments. The mathematical details of the next step, for the least squares fitting procedure can be found as an Appendix A. The regression analysis was performed using statistical software JMP IN 5.1 by SAS Institute. The software also conducts appropriate statistical test of hypotheses (see in Appendix) concerning the parameters in the mathematical model.

5.4.2.1 Prediction of experiment settings for targeted response

Common applications of the RS approximation are to determine the settings of the factors or domain of the parameters that produce optimum (maximum or minimum) or

targeted value of the response. This can easily be achieved by graphical means in one- and two-variable cases. For higher dimensional problems numerical optimization techniques are usually applied. Here, two-variable response surfaces at each solvent mix ratio were obtained. In addition visual characterization of the samples provided further information on the morphology and applicability of the mats. SEM and conventional digital imaging documented the range of applicable process conditions.

5.4.2.2 Results for the Fiber Diameter

Experimental procedure described in the previous section was applied at the 9 settings for each 3 solvent mixing ratios. Following the fiber production and SEM imaging the statistics for fiber diameter sampled on the images of each non-woven mat were computed. Fiber diameters were measured from the SEM images using the Image Pro Plus software. The results of the measurements given in Table 9 show that, DMF-only PVDF solutions rarely produce fibers. It was impossible to make a measurement at some experimental points because beads or droplets were spun on the collector mostly as shown in Figure 37.

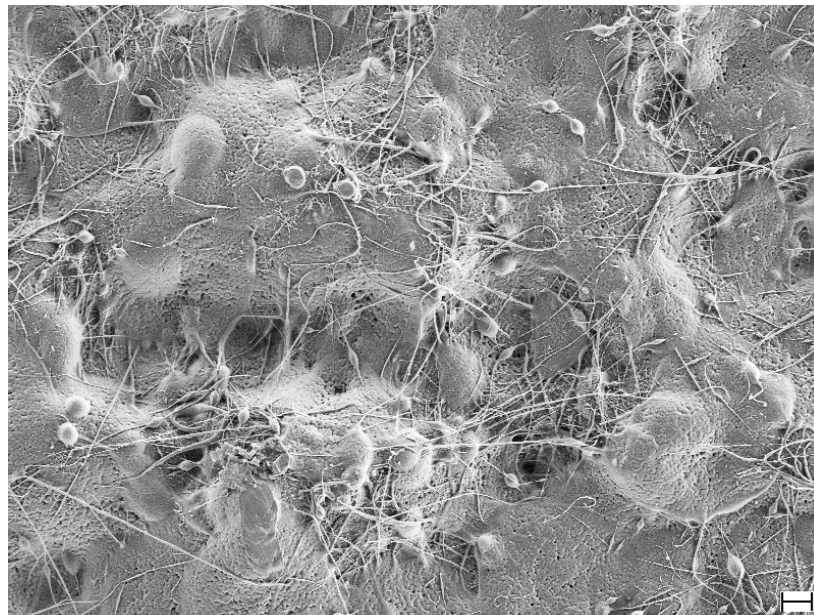


Figure 37 DMF only sample composed of beads and droplets, and very few fibers. Bar corresponds to 10 μ m.

Table 9 Fiber diameter measurements obtained from the DMF Only samples. As given in the graph, some samples do not have fiber structures hence it is not feasible to count them as fiber data.

DMF-only PVDF Solution			
Specimen ID	Voltage (kV)	Distance (cm)	Fiber Diameter (μm)
0_15cm8kV	8	15	0.615
0_15cm10kV	10	15	0.621
0_15cm12kV	12	15	NA
0_22.5cm8kV	8	22.5	0.687
0_22.5cm10kV	10	22.5	NA
0_22.5cm12kV	12	22.5	NA
0_30cm8kV	8	30	0.608
0_30cm10kV	10	30	0.538
0_30cm12kV	12	30	NA

Another solution prepared by a mixture of DMF and Acetone in 25% ratio, provided better results, yet, the mats were not composed of uniform fibers as shown in Figure 38. Fiber diameter investigation results for this sample groups are given in Table 10 below.

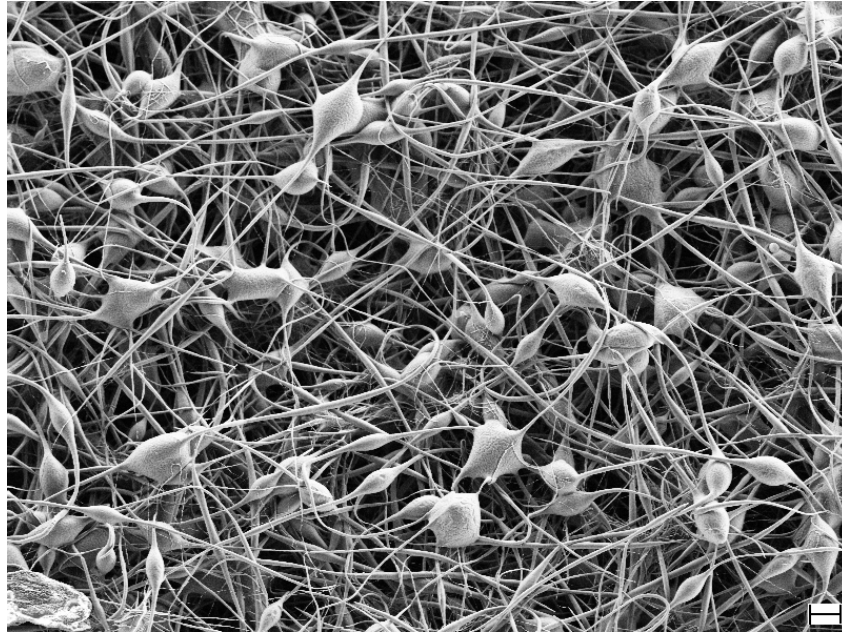


Figure 38 25% Acetone/DMFmixture sample. The mat is composed of fibers and beads, with few droplets. Bar corresponds to 10 μ m.

Table 10 Fiber diameter measurements obtained from the Acetone DMF mixture with a ratio of 0.25. These sample also included some non-fiber structures, yet, measurement could be obtained.

Acetone / DMF: 0.25 PVDF Solution			
Specimen ID	Voltage (kV)	Distance (cm)	Fiber Diameter (μ m)
0.25_15cm8kV	8	15	1.067
0.25_15cm10kV	10	15	0.964
0.25_15cm12kV	12	15	0.856
0.25_22.5cm8kV	8	22.5	1.111
0.25_22.5cm10kV	10	22.5	1.183
0.25_22.5cm12kV	12	22.5	1.514
0.25_30cm8kV	8	30	1.496
0.25_30cm10kV	10	30	1.299
0.25_30cm12kV	12	30	1.149

Final solution was prepared by a 50% Acetone/DMF mixture and gave the best results in terms of both mat morphology and fiber uniformity. Fibers diameters were in

the micron scale as tabulated in Table 11. Furthermore, a detailed road-map of fiber production for this sample group is given in Figure 39.

Table 11 Fiber diameter measurements obtained from the Acetone and DMF with 50% mixing ratio.

Acetone / DMF: 0.50 PVDF Solution			
Specimen ID	Voltage (kV)	Distance (cm)	Fiber Diameter (μm)
0.50_15cm8kV	8	15	0.876
0.50_15cm10kV	10	15	0.928
0.50_15cm12kV	12	15	0.861
0.50_22.5cm8kV	8	22.5	2.105
0.50_22.5cm10kV	10	22.5	1.535
0.50_22.5cm12kV	12	22.5	1.453
0.50_30cm8kV	8	30	2.153
0.50_30cm10kV	10	30	1.621
0.50_30cm12kV	12	30	1.384

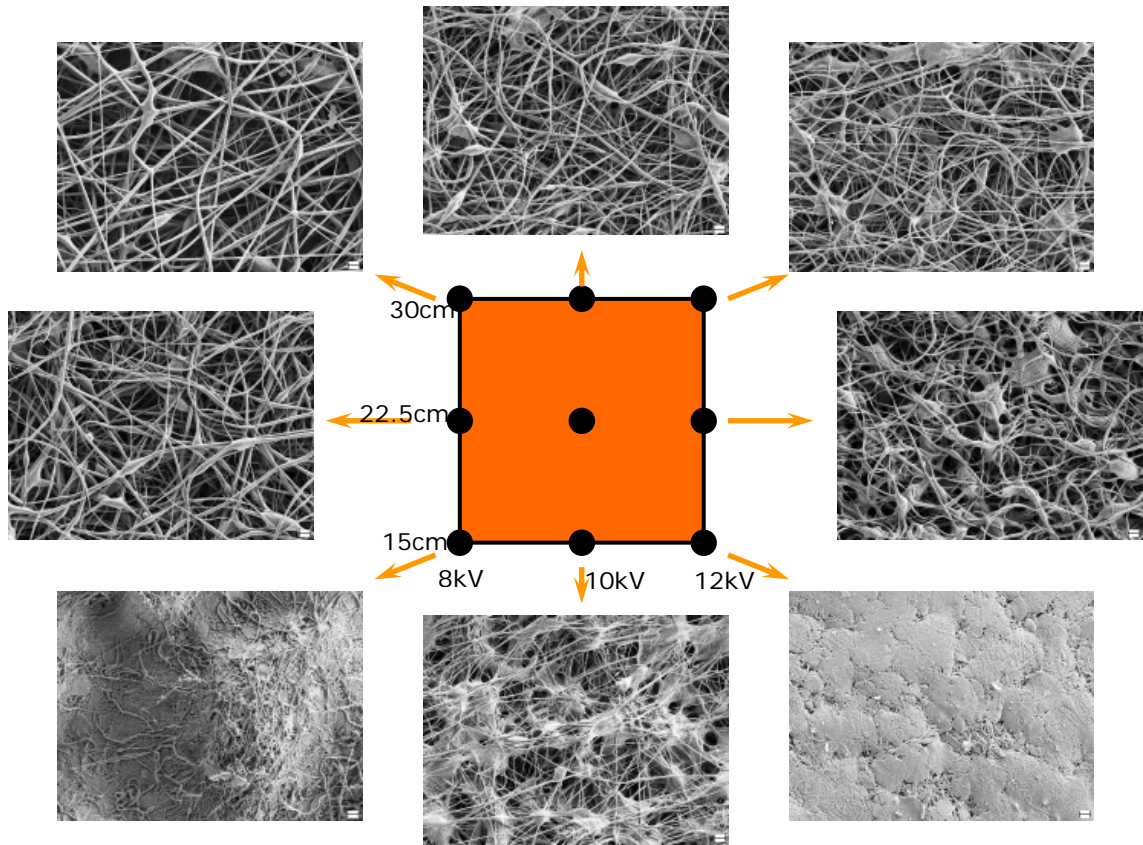


Figure 39 A detailed road-map of micrometer fiber fabrication scheme for 50% Acetone/DMF ratio mixture, PVDF solution.

After completing the diameter measurements, regression analysis was performed on 25% and 50% Acetone/DMF ratio samples to fit for the observed response y , the fiber diameter. Statistical analysis was not performed on the DMF-only sample due to the non-uniformity and lack of fiber formation on the sample mats. The fiber diameter was approximated by a quadratic polynomial response surfaces as function of applied voltage and collector distance for the two Acetone and DMF mixed PVDF solutions. Two variable case and the response function \hat{y} is related as,

$$\hat{y} = a_0 + a_1x_1 + a_2x_2 + a_3x_1x_2 + a_4x_1^2 + a_5x_2^2 \quad (5.5)$$

The unknown coefficients a_i in Equation (5.5) were found by JMP IN 5.0 which employs the least squares method as described in the Appendix B. Statistical results of

the quadratic model to predict the fiber diameter for 25% and 50% Acetone/DMF ratios are tabulated in Table 12 and Table 13.

Table 12 Statistical results for the quadratic fit on the 25% Acetone/DMF sample.

Summary of Fit	
R^2	0.592
R^2_{adj}	-0.088
RMSE	0.232
Mean	1.182

Table 13 Statistical results for the quadratic fit on the 50% Acetone/DMF sample.

Summary of Fit	
R^2	0.972
R^2_{adj}	0.924
RMSE	0.135
Mean	1.435

The second columns in Table 12 and Table 13 report the measures of goodness of the fits, R^2 and R^2_{adj} via Equation (A.8). 25% mixture sample did not yield as good results as the 50% one. R^2 and R^2_{adj} values of 25% sample are well below the typical significance limit 0.90, R^2 value is around 0.6 and R^2_{adj} is negative. The residuals and percent errors between predicted and actual fiber diameter are given in Table 14. Therefore, the model for 25% sample is not reliable. More data should be collected to try a higher order model in order to construct a prediction formula.

50% sample, on the other hand, gave R^2 and R^2_{adj} values close to 0.90 which is a statistical indication that the variation in the fiber diameter is explained reasonably well by the model. Residuals and percent errors are given in Table 15. Average percent error in the prediction formula of the 50% sample is approximately 5%, whereas that of 25% sample is around 10%.

Table 14 Residuals and percent errors in the quadratic model for the 25% sample.

Actual Fiber Diameter	Predicted Fiber Diameter	Residuals	% Error
1.067	0.971	0.096	9.02
0.964	0.929	0.035	3.61
0.856	0.987	0.131	15.31
1.111	1.312	0.201	18.08
1.183	1.236	0.053	4.47
1.514	1.260	0.254	16.76
1.496	1.391	0.105	6.99
1.299	1.282	0.018	1.39
1.149	1.272	0.123	10.68

Table 15 Residuals and percent errors of the 50% Acetone/DMF solution sample.

Actual Fiber Diameter	Predicted Fiber Diameter	Residuals	% Error
0.876	0.976	0.099	11.39
0.928	0.814	0.113	12.20
0.861	0.874	0.013	1.55
2.105	1.974	0.131	6.21
1.535	1.624	0.089	5.76
1.453	1.495	0.042	2.91
2.153	2.184	0.031	1.44
1.621	1.645	0.025	1.52
1.384	1.328	0.056	4.02

In short, DMF-only and 25% solvent mix ratio was found inapplicable regarding both the fiber uniformity and morphology (further confirmed by the pictures in 5.4.1.1). Hence, two-variable domain at 50% solvent mix ratio was chosen as the final design space and further predictions and analyses were conducted at this space. A 20 by 20 mesh is created in the experimental design space, voltage and collector distance being the design parameters. The fiber diameter prediction formula obtained from the response surface approximation over those 9 points is given in Equation (5.6).

$$\hat{y} = -1.205 + 0.498 \times x_1 - 0.536 \times x_2 - 0.007 \times x_1^2 - 0.012 \times x_1 \times x_2 + 0.034 \times x_2^2 \quad (5.6)$$

The formula is imported into the 20x20 mesh system to observe the variation in fiber diameter due to change in voltage and collector distance in that experimental space. Figure 40 and Figure 41 show the 3D surface plot and contour plot of the fiber diameter as a response to applied voltage and collector distance.

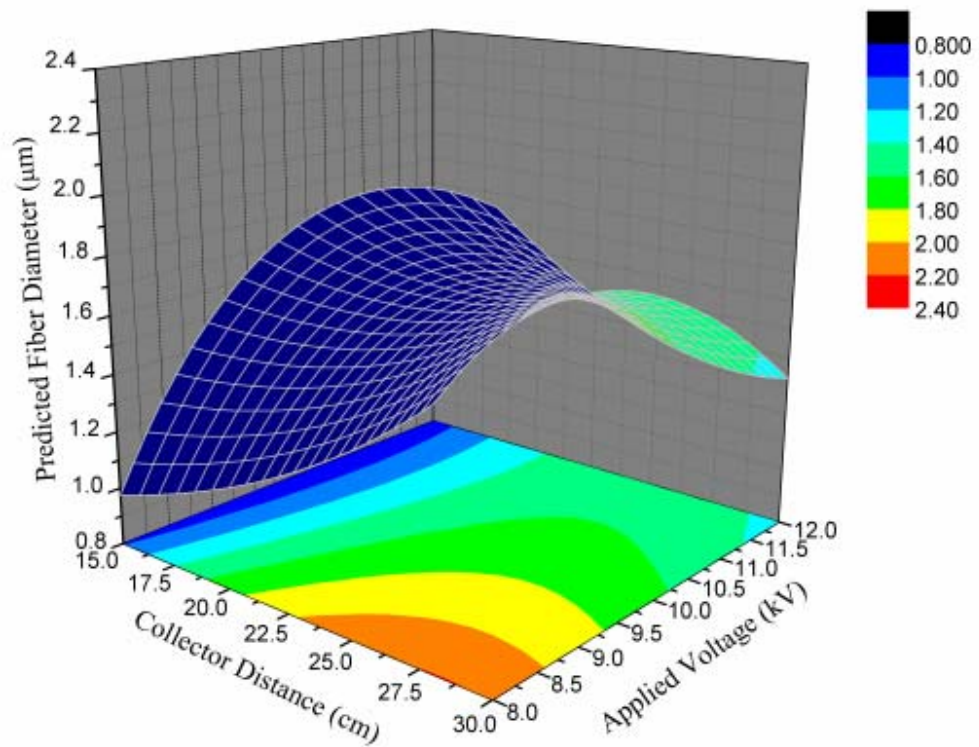


Figure 40 3D response surface plot generated via 441 data points calculated by the prediction formula given in Equation (5.6).

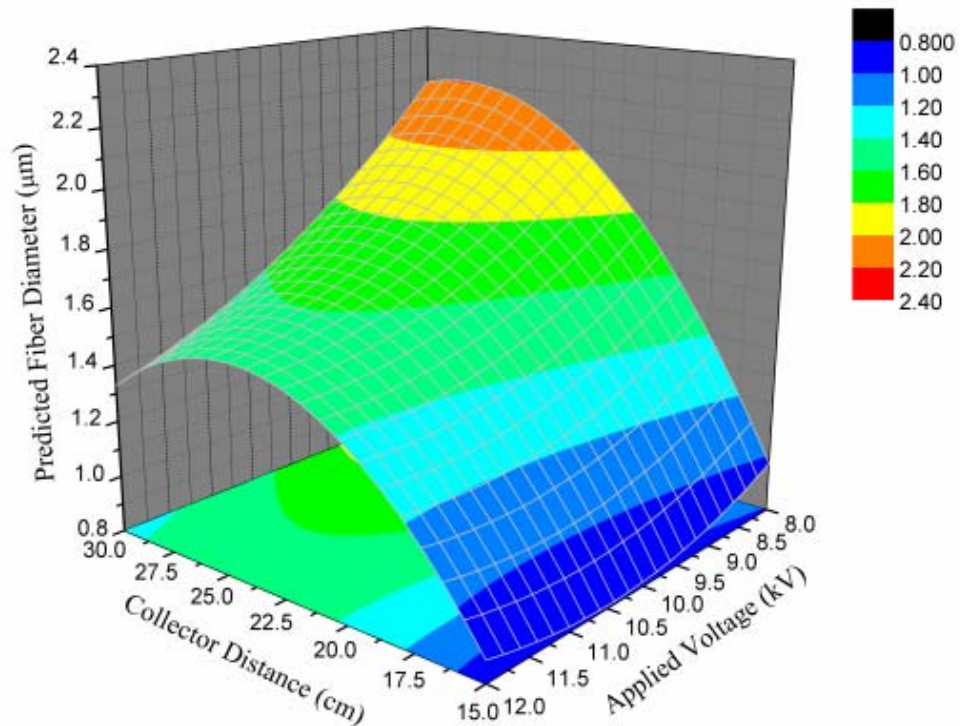


Figure 41 Same 3D surface plot given in Figure 40 with a view from opposite side of the surface plot.

The other reported statistics, t-ratio and p-values associated with the coefficient estimates are statistical measures of significance of the individual parameters in explaining the variability of the fiber diameter over the square domain of interest. Lower the p-value, more significant the parameter is.

Statistics given in Table 16 suggest that collector distance is more a significant factor than applied voltage in explaining the variation of the fiber diameter. Because, the p-value of collector distance is below the significance level of 0.05, which means that the probability of being wrong in accepting that a_1 and a_3 are different than zero (x_1 as significant factor) will be less than 0.05. Considering the p-values, applied voltage has no strong statistical evidence that the coefficients are different than zero as the p-values are relatively higher than that of collector distance. However, the effect of voltage is observed at the 30cm collector distance and the residuals among these set of points are good enough to state the existence of voltage effect.

Table 16 Parameter estimates and p-value statistics for the quadratic model fitted over 9 data.

Term	Estimate	P-Value
Intercept, a_0	-2.030	0.502
Collector Distance, a_1	0.496	0.011
Applied Voltage, a_2	-0.391	0.481
(Collector Distance) ² , a_3	-0.007	0.026
Collector Distance*Applied Voltage, a_4	-0.013	0.068
(Applied Voltage) ² , a_5	0.028	0.329

The significance of collector distance is not surprising since it affects the amount of solvent evaporation. Applied voltage; however, were also expected to play a role in fiber formation as demonstrated in our previous study with Poly(acrylonitrile) [102], by Demir for polyurethane fibers [38], and by Sukigara for nano-scale fiber production of Bombyx silk [38, 96]. In addition to affect of voltage on the fiber diameter, applied voltage is also expected to be vital in stretching of the electrospun fibers.

5.4.3 Characterization of As-Spun PVDF Mats

The PVDF mats were also characterized to observe their crystallinity and their crystal phase content as done for the solution cast films. Similar tests were conducted on the fiber mats such as FT-IR, XRD, and DSC. The fiber mats were characterized both “as spun” and after mechanical stretching. A comparison between the fiber mats and solution cast films is also introduced to monitor the differences between two processes. The characterized film and the mat to compare are picked from the optimized region of interest associated with each process.

5.4.3.1 XRD

XRD results were obtained from the same measurement scheme presented in 4.3.1.2. The data observed from the electrospun samples are shown in Figure 42. As plotted in Figure 42, electrospun samples have the characteristic strong α -phase peaks at

14.26, 17.06, and 18.86⁰ from the reflections of (100), (020), and (110) planes, and weak peaks at 25.88⁰. Mats also show the characteristic strong β -phase peak at 20.72⁰, which is a reflection of (200) and (110) planes.

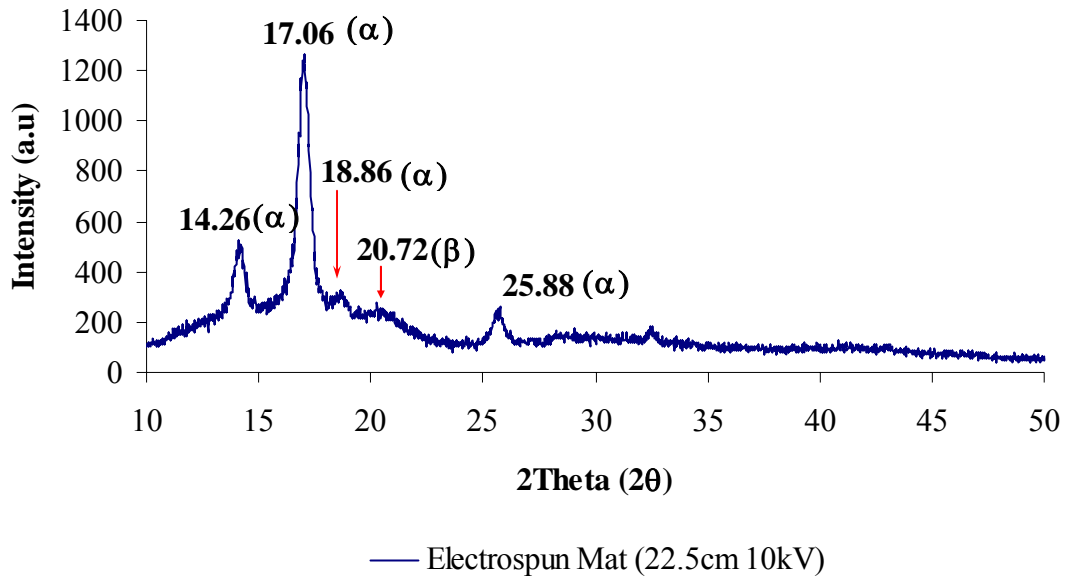


Figure 42 XRD measurement results of an electrospun sample. Sample ID:
Acetone/DMF:0.5 22.5cm 10kV)

Figure 42 indicates the characteristic α -phase peaks obtained from the electrospun samples are dominant over the β -phase ones. This result alone suggests stretching of electrospun mats is necessary for introducing piezoelectric features; however, the DSC measurements should also be analyzed for an accurate conclusion.

When multiple samples of several applied voltage were analyzed, correlation between the electrostatic force and β -phase formation was noted. For large collector distance values, it was observed that as the applied voltage is increased, the β -phase formation in the electrospun fiber crystal structures increases. This is an indication that an increase in the electrostatic force applied on the polymer solution, stretches the polymer from the tip of the needle until the polymer touches the collector screen. As Figure 43 suggests, when the voltage is increased from 8 kV to 12kV, the β -phase peak tends to increase while the α -phase peaks diminish. Nevertheless, the α -phase peaks

are still dominant over the β -phase ones; hence, DSC measurements are still critical in terms of stretching the mats.

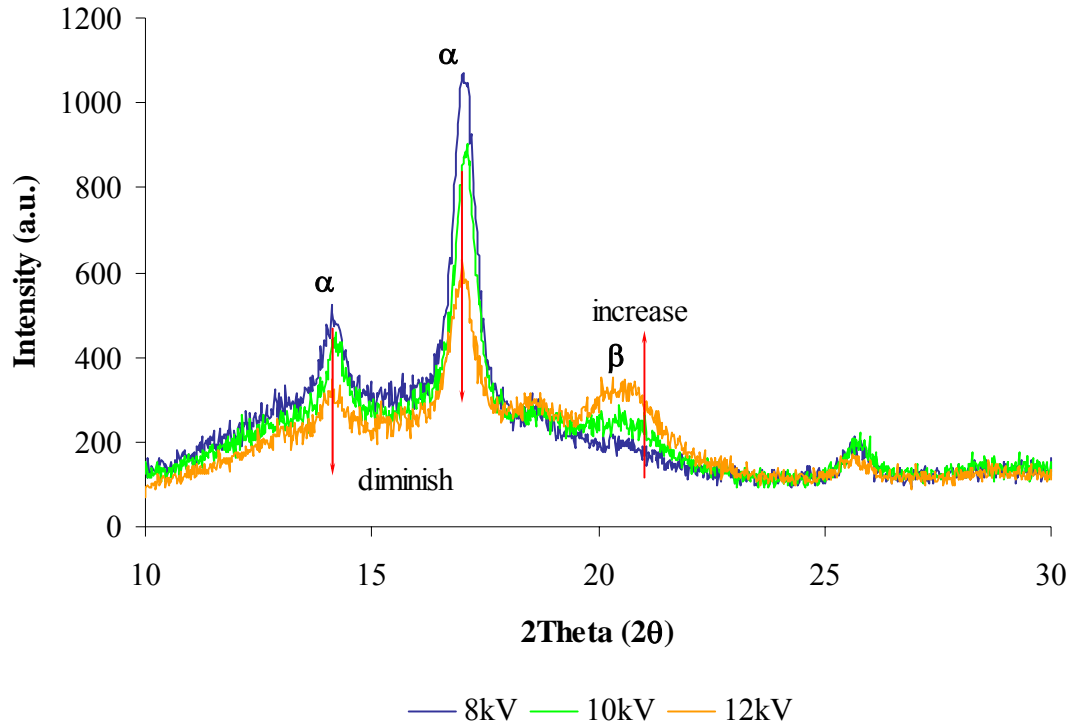


Figure 43 Effect of electrical force applied on the fiber crystal structure.

5.4.3.2 DSC Measurements

Although the XRD measurements of the electrospun samples were observed as α -phase dominant, the DSC results suggested a contradictory conclusion. The shift occurred on the DSC curve of the solution cast films due to stretching also appeared on the curves of electrospun samples. As Figure 44 shows, enthalpy plot of the electrospun sample perfectly fit onto that of the stretched solution cast film plot.

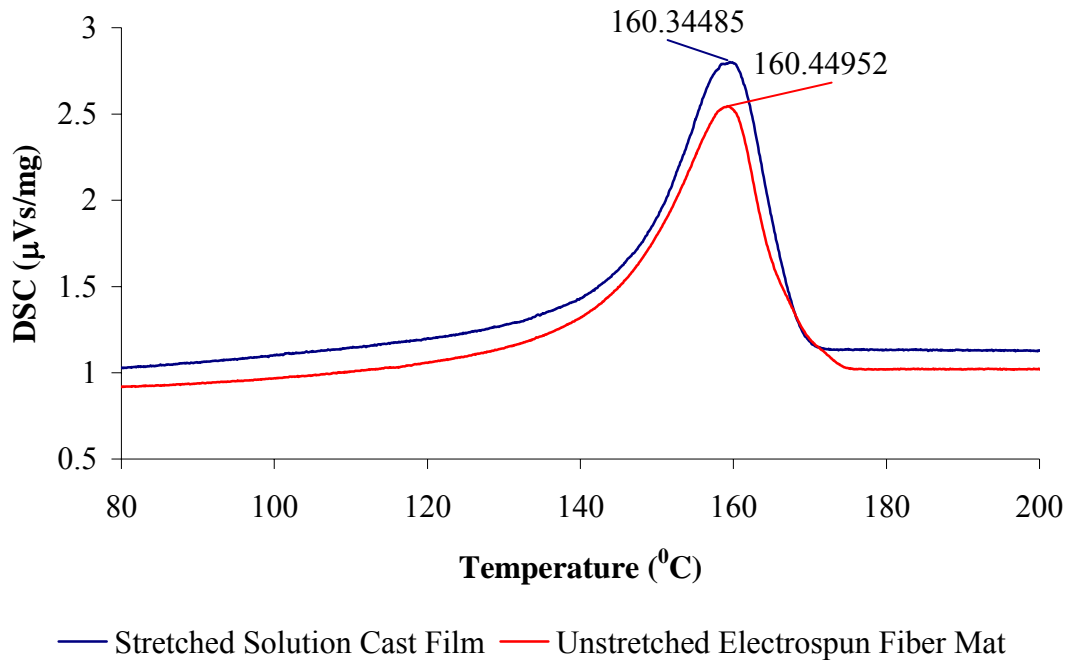


Figure 44 DSC results of un-stretched electrospun sample (Sample ID: ES_0.5_225cm12kVunstr) and its comparison with stretched solution cast sample (Sample ID: SC_45str).

Considering the DSC results monitor, coinciding melting points suggest that the electrospun fiber mats have dominant β -phase crystallinity even prior to stretching. Yet, the XRD measurements did not reveal a significant β -phase content, α -phase content was even observed to be dominant. The contradictory XRD result was attributed to the fact that fibers have large surface to volume ratio of the fiber geometries. Since the α -phase tends to form at the surface and since the surface to volume ratio of the fibers is large, it is reasonable to observe α -phase as the dominant phase. However, the content of β -phase inside the fiber structure is thought to be very high that the melting point of the electrospun mats reveals the same value with that of the stretched solution cast films. Hence, it is reasonable to state that the electrospun mats are rich in β -phase content. This adds a significant advantage of the electrospinning in potential application on MAV wing: it is easier and quicker to fabricate electroactive PVDF film via electrospinning since stretching process is not needed and thus canceled. It is also easier to coat 3D geometry by electrospinning since the solution is dried while spinning in air. For instance, regarding the previous MAV

case, electrospinning makes coating of skeletal structures easier as imaged in Figure 36 due to air drying property while spinning at air.

5.4.3.3 Mechanical Tests

Electrospun mats were also tested to determine their tensile limits. MTS Synergie 200 Tensile Testing Machine with its 100N load cell was used again. The tests were conducted on 50% DMF/Acetone mixture samples since they were chosen as having the optimum sample properties and desired applicability. 2mm by 60mm rectangular samples were prepared and tested. The results are tabulated in Table 17.

Table 17 Tensile test results of the electrospun samples obtained at the 50% DMF/Acetone experimental design space.

Sample ID	σ_u (MPa)	σ_b (MPa)	ϵ_b (%)	E (MPa)
ES15cm8kV	3.05±0.27	3.045	2.630	136.355
ES15cm10kV	0.53±0.09	0.530	7.110	21.270
ES15cm12kV	2.69±1.04	2.685	4.470	92.340
ES22.5cm8kV	0.47±0.06	0.470	21.370	10.085
ES22.5cm10kV	0.36±0.03	0.360	16.770	10.195
ES22.55cm12kV	NA	NA	NA	NA
ES30cm8kV	0.26±0.05	0.060	51.780	2.735
ES30cm10kV	0.22±0.02	0.165	39.010	3.635
ES30cm12kV	NA	NA	NA	NA

An analysis was conducted to see if there is a correlation between elastic modulus and fiber diameter. A simple plot in Figure 45 exhibits that the elastic modulus and ultimate force applied on the samples increase with decreasing fiber diameter. Increase in the ultimate force for finer fiber diameter values is expected since finer fibers have lower defect possibilities. On the other hand, the variation in the elastic modulus values is higher than expected. There is 10 fold modification in the modulus as the fibers get finer which cannot be explained by the defect probability and needs further investigation.

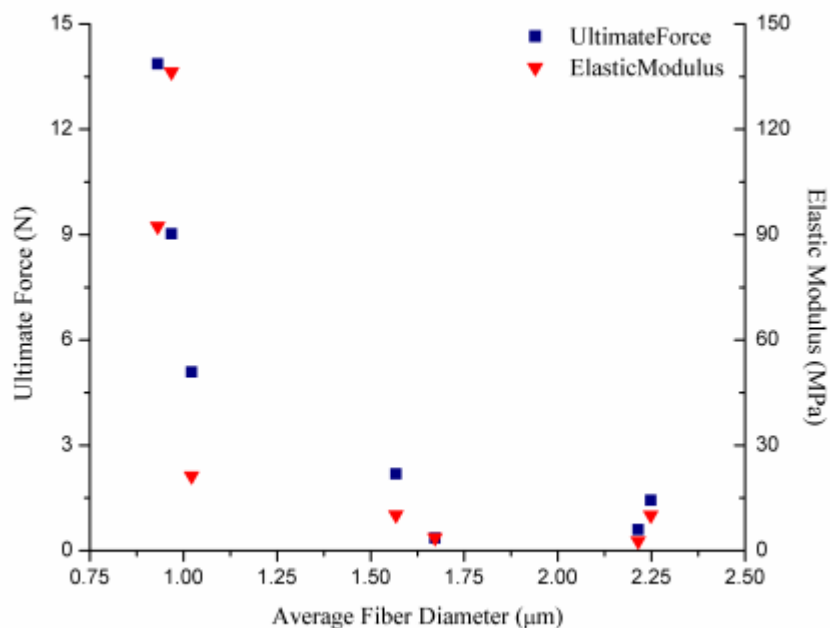


Figure 45 Correlation between elastic modulus and fiber diameter, and ultimate force and fiber diameter are plotted.

5.4.4 Characterization of Stretched Electrospun Mats

Electrospun mats were also stretched similar to solution cast films. The aim was similar: to observe the change in β -phase content in the stretched e-spin mats so that contradictory conclusions from XRD and DSC measurements on as spun mats can be further discussed.

5.4.4.1 XRD Results

Stretched electrospun mats were characterized by XRD to demonstrate the significance of stretching in change in the β -phase content and formation.

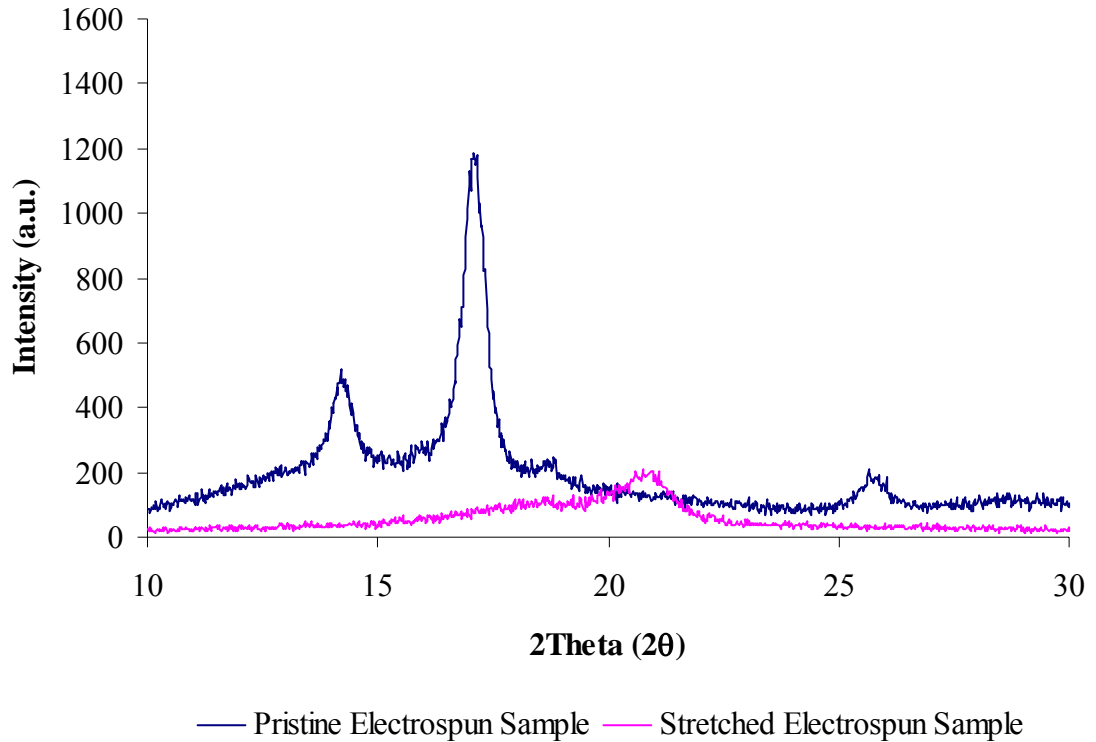


Figure 46 XRD result of pristine and stretched electrospun sample focusing at the critical region of interest (Sample ID: ES_22.5cm12kV).

The results plotted in Figure 46 reveal that there is a significant amount of decrease in β -phase content, yet there is a very slight modification in the β -phase amount. This measurement verifies the β -phase modification through stretching, yet, the increase is very slight when compared to the effect of stretching in the solution cast films.

5.4.4.2 DSC Results

Samples taken from each stretched electrospun sample in the final design domain were analyzed via DSC. Approximately 5mg of each sample was put in DSC. The results exhibit that stretching the e-spun mats had a minor effect on the β -phase content since the melting point values altered barely. This result is thought to be a consequence of the stretching occurring whilst spinning at air. Stretching is effective to some extent, that is, there is a limit after which β -phase content is not modified with further stretching.

Hence, the samples still have similar β -phase contents. Therefore the DSC measurements gave similar graphs with the pristine electrospun mats as given in Figure 47. To sum up, both the XRD and DSC results revealed a negligible change in the extent of β -phase crystallites.

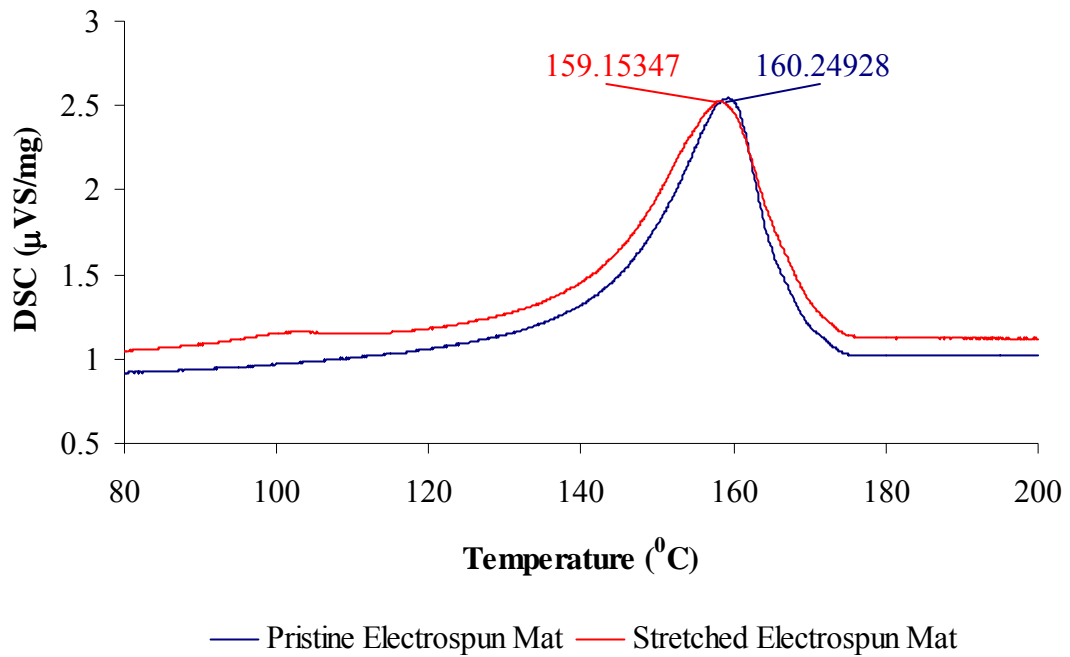


Figure 47 Stretched and pristine electrospun samples (Sample ID: ES_0.5_22.5cm12kV).

6. ZINC OXIDE FIBER MATS

6.1 Process: Electrospinning of Organo-Metallic Precursor Solutions

Electrospinning process is a very simple and versatile method to produce ceramic fibers with diameters as low as 30 nanometers. The process is very similar to the electrospinning of polymer fibers, that is, both of them arise from the electrospinning of polymer-based solutions in the same set-up given in Figure 27. Yet, an additional temperature treatment is applied to convert the precursor fiber mats into ceramic oxide fibrous structures. The goal of this part of the study is to fabricate and control the processing of nano-scale zinc oxide structures to be employed in a piezoelectric device.

In ceramic fiber formation, a polymer precursor solution is prepared by first choosing a polymer with a desired molecular architecture. Polymer is then dissolved in an appropriate solvent. The ceramic material or the salt which possesses the desired elements is also ideally solved in the same solvent. The solutions are mixed with each other at a specific temperature for a sol-gel reaction to occur. The resultant solution that is prepared by following these steps is called the precursor solution and this precursor organo-metallic solution is electrospun initially. When the precursor solution is electrospun, mats of randomly oriented polymer-based organo-metallic composite fibers are formed, which are called precursor fibers. Calcination of these precursor fiber mats is employed according to the thermal history obtained from TGA in the desired atmosphere. Temperature limits for burning out the organic materials and obtaining only a mat of oxide fibers are attained from this analysis. If oxygen is chosen as the desired calcination atmosphere, then the resultant material would be the metal oxide fibers.

Experimental procedure is as follows: Poly(vinyl alcohol) (PVA) obtained from Aldrich is dissolved in distilled water in 12% w/w concentration using an Erlenmeyer

flask. 12% concentration limit was chosen to maximize the viscosity of the solution to produce thicker fibers, without making the solution difficult to handle. That is, a 15% percent solution would produce thicker fibers, but the solution would be difficult to handle and electrospin. Following the determination of the polymer concentration, the polymer is very gently poured in the stirring water and the mixture is stirred until all of the PVA is dissolved in the solution. In another beaker, aqueous zinc acetate solution is prepared until its solubility limit, so that the zinc amount is kept at maximum. When both of the solutions are totally dissolved in water, they are heated up to 80⁰C. Following the heating process, the aqueous zinc acetate solution is poured slowly into the aqueous PVA solution and the mixture is kept and stirred at 80⁰C for 5 hours. After 5 hours of the sol-gel reaction, the precursor solution is ready for electrospinning.

In order to produce ZnO fibers with optimum geometry and morphology of interest, solution and calcination parameters were altered. The ingredients of the solutions are given in Table 18. Different solutions with different zinc contents were prepared and electrospun to observe the effect of zinc content in the final structure's morphology and geometry. In addition, two heating regimes were experimented with varying heating rate and calcination temperature: precursor fibers were calcinated at 500⁰C at a heating rate of 1⁰C/min and 0.5⁰C/min.

Table 18 Precursor solution and calcination parameters that were employed for the fabrication of ZnO fibers

Sample ID	PVA		Zinc Acetate	
	Mass (g)	Concentration %	Mass (g)	Concentration %
090306_24%	1.076	9.200	0.685	64
270306_50%	5.026	12.028	7.040	26
050406_37%	2.504	12.000	2.585	35.5
130406_78%	3.336	11.850	2.585	35

Each polymer-ceramic precursor solution was inserted into a syringe and the syringe was put in the computer controlled syringe pump set-up (Figure 27). The solution is electrospun under 9kV with a flow rate of 25 μ l/min and 8cm collector

distance, which was chosen arbitrary, yet, it is observed that these parameter limits continuously form fibers. For each sample mat, 4 milliliters of the solution was electrospun on the collector screen. Electrospun mat of organo-metallic fiber was then gently peeled off from the aluminum substrate and placed over two supports, as depicted in Figure 48, to further be put into the furnace. The supports were found to be necessary for the calcination process because when the fiber mat were to left touching the substrate, the fibers are broken into pieces due to friction force between the mat and the substrate as the mats shrink during calcination due to polymer burn-out. Therefore, samples were finally left in air (Figure 48) to be protected from the friction force introduced with the shrinkage of fibers during calcination.

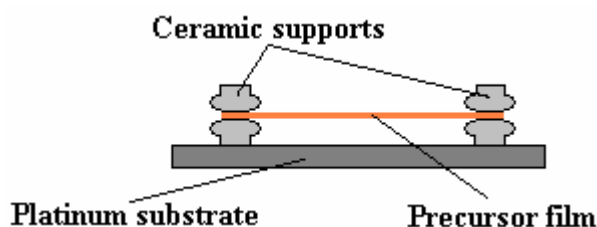


Figure 48 Schematic representation of sample preparation for calcination process.

The heating scheme for the calcination of the precursor fibers is critical in terms of the desired physical properties of the final structure. Following the sample preparation represented in Figure 48, a two step heating scheme as in Figure 49, is programmed in the box furnace (Protherm PLF Commander 100). The sample is placed into the box furnace which is at room temperature. Then, the furnace is initially heated to 120⁰C and kept for one hour at that temperature to dry the precursor mat and get rid of the moisture in the sample. Finally, the furnace is heated up to 500⁰C at a rate of 0.5⁰C/min to get rid of all organic compounds and be left with ZnO fiber mat.

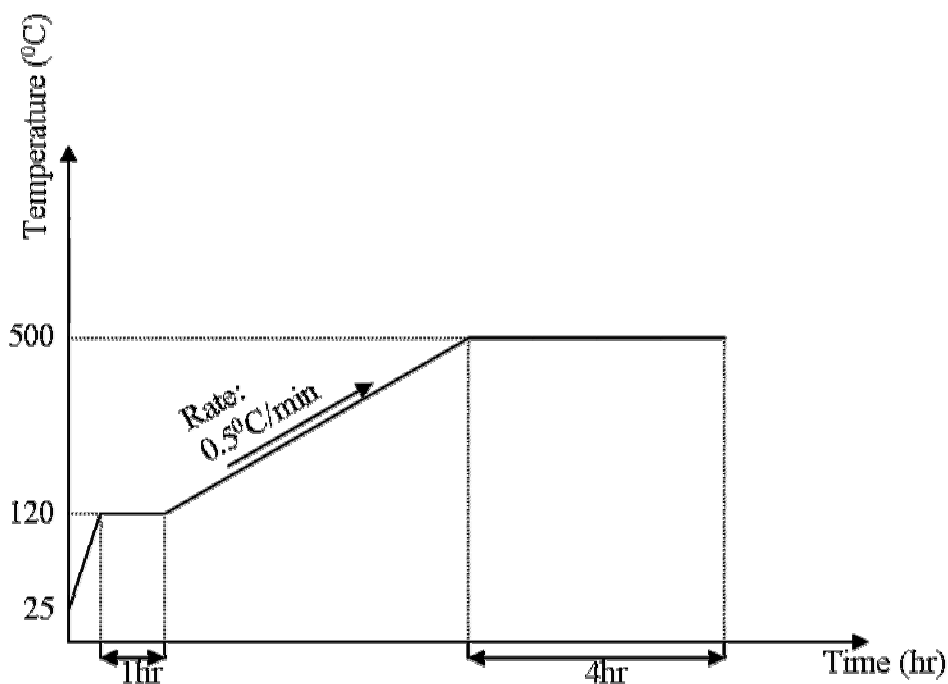


Figure 49 Heating scheme for the calcination of polymer/acetate precursor fibers to produce ZnO fibers.

6.2 Characterization Tools

Prior to oxide formation, the precursor fibers are needed to be analyzed via TGA (Netzsch STA 449C Jupiter) to determine the necessary temperature treatment procedure. Then the produced oxide fibers should first be analyzed by SEM and Energy Dispersive X-Ray Spectroscopy (EDXS) to observe their geometry and chemical content, respectively. If the EDXS measurements give a zinc and oxygen content, then the structure should further be characterized by XRD to determine the crystal structure of the oxide fiber.

6.3 Results and Discussions

6.3.1 Precursor Solution Concentration

Temperature treatment on the precursor fibers is vital to form organic material free oxide fibers. The TGA measurement given in Figure 50 revealed that any temperature higher than 425⁰C would end up with oxides.

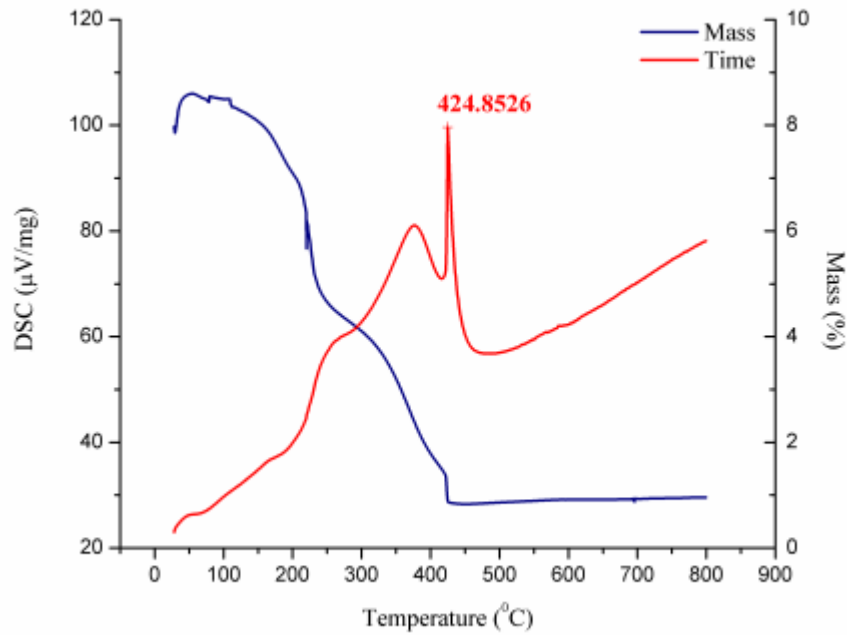


Figure 50 TGA measurement results of the precursor fiber mat.

As the figure suggests, variation in mass of the sample no longer alters after 425⁰C, which means that the sample holder in TGA was left with oxide material. Therefore, the calcination temperature of 500⁰C is a reasonable temperature to produce oxide fibers.

6.3.2 Calcined Zinc Oxide Mats

Ceramic fibers of zinc oxide were prepared as described in section 6.1. Resultant fibers were characterized by SEM, EDXS, and XRD to figure out the crystal structures

of the fabricated ZnO fibers. As previously mentioned in 3.2, the crystal structure of interest for the ZnO fiber mats is the wurtzite structure.

First of all, precursor solution properties and calcination scheme should be optimized to produce smooth continuous fibers. Four different solution concentrations with different zinc percentages were prepared as tabulated in Table 18. A calcination procedure was further utilized at two heating rates and two calcination temperatures. Zinc content was found to significantly affect the morphology of the resultant oxide fibers. *ID_090306_24%* and *ID_270306_50%* samples produced broken fibers, in other words, discontinuous fibers as given in Figure 51. As the figure suggests, although the precursor fibers are continuous, zinc oxide fibers were broken after calcination.

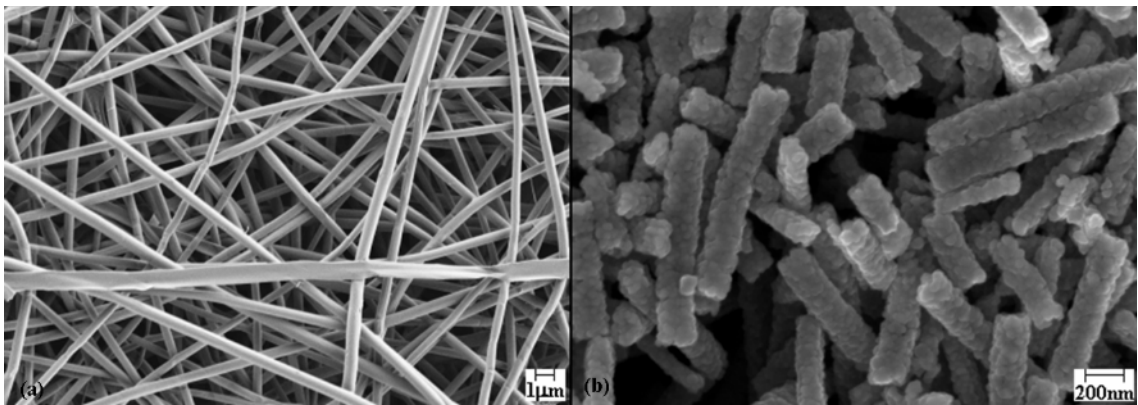


Figure 51 *ID_090306_24%Zn* is the precursor solution with the lowest zinc content. Although the precursor fibers are uniform and continuous (a), zinc oxide particles cannot always form continuous fibers, they mostly break into pieces due to small amount of zinc content (b).

Besides, when the zinc content is increased to 78% like in the sample *ID_130406_78%*, there exist a zinc abundance both on the precursor fibers and on the calcined zinc oxide fibers, as imaged in Figure 52. Therefore, optimum zinc content should be found to form uniform fibers, that is, uniform in terms of fiber morphology.

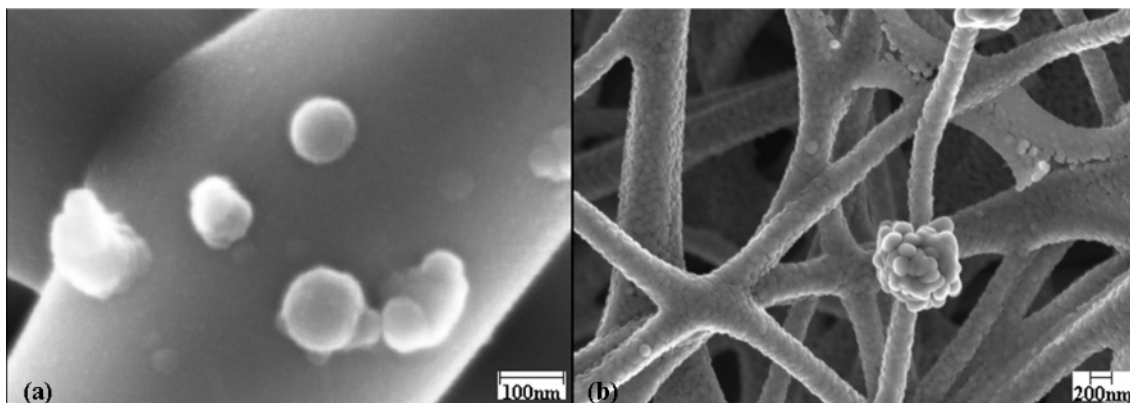


Figure 52 ID_270306_50%Zn is the precursor solution with the highest zinc content. As it is seen in these SEM images, excess amount of zinc precipitates over both the precursor fibers (a) and the ZnO fiber itself after calcination (b).

Regarding the SEM images, ID_050406_37%Zn gave fibers with highest uniformity in their morphology with a heating regime of $0.5^{\circ}\text{C}/\text{min}$ from room temperature to 500°C . The produced fibers are mostly precipitate-free, and uniform in diameter (Figure 53).

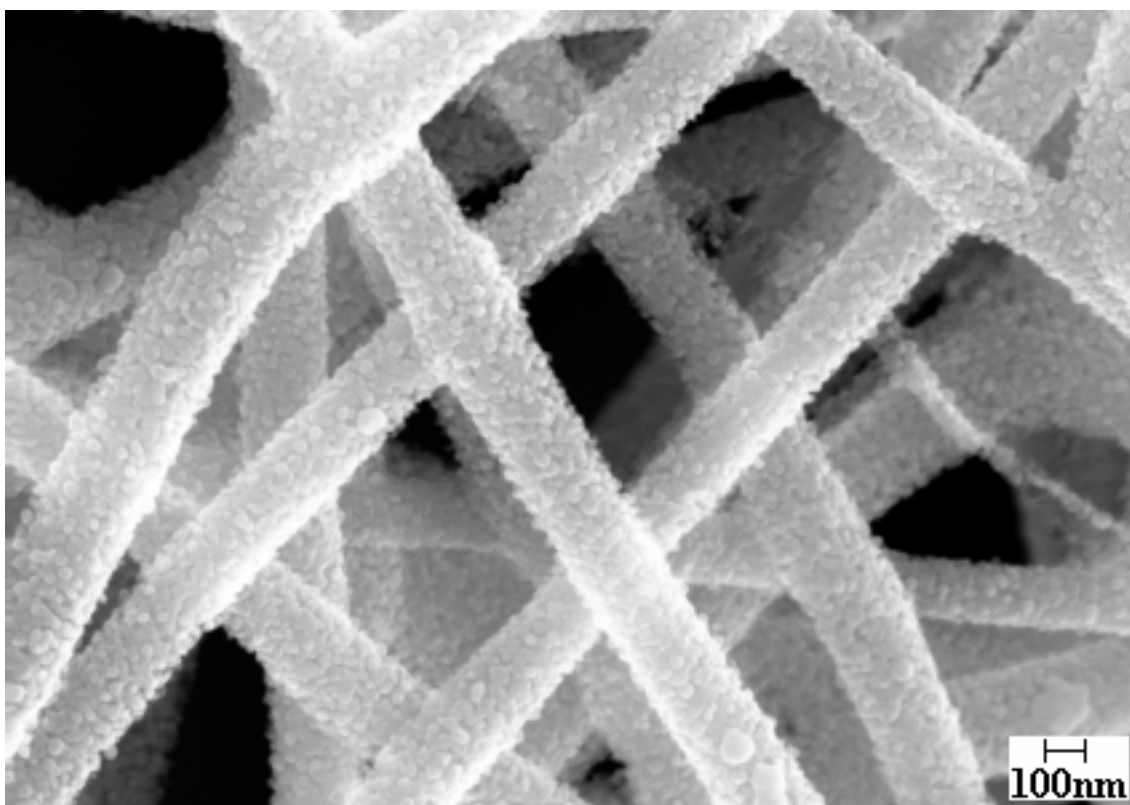


Figure 53 Optimized zinc content revealed uniform ZnO fibers.

Nevertheless, high magnification images reveal that the fibers are composed of smaller spherical-to-hexagonal balls instead of continuous smooth fibers, as given in Figure 54. As it is defined in Wikipedia Online Encyclopedia “*fiber is a class of materials that are continuous filaments or are in discrete elongated pieces, similar to lengths of thread*”² and as far as this definition is concerned, “fibers” of ZnO are formed via this process. Yet, the discrete particles in this elongated chain introduce physical drawbacks.

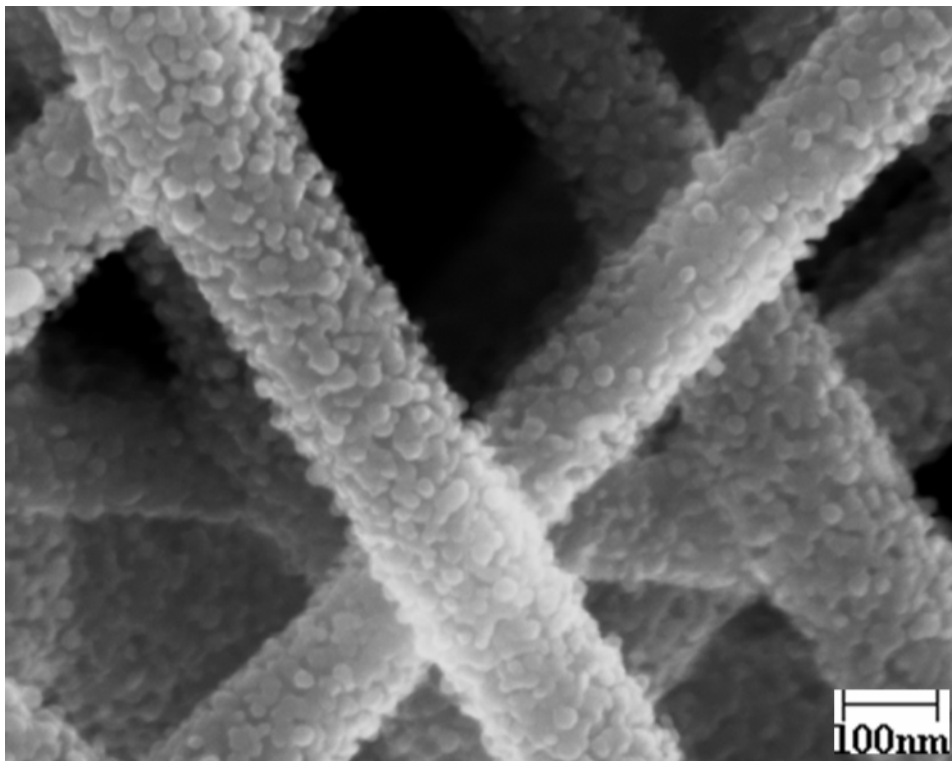


Figure 54 ZnO sample imaged by 200K magnified. Grains with an average diameter of 20nm can be easily seen on the fiber structure.

When the fabricated mats were taken out of the furnace, it is observed that the ZnO fibers are fragile and difficult to handle; yet, the produced mat can lift its own weight and stays connected. This mechanical weakness is thought to be caused by the grain boundaries in the structure. Since the grain boundaries on the fiber can be easily seen, those boundaries work as weak links and fracture occurs through these

² The definition is seized from the online source Wikipedia, The Free Encyclopedia. URL: www.wikipedia.org

boundaries. There are a lot of grain boundaries on the fiber surface; hence, they make the fibers weak.

6.3.2.1 EDXS Measurements

Following the solution optimization, ZnO mats should be analyzed with EDXS and XRD to spot the content of the mats and crystallographic property of the ZnO fibers. As Figure 55 suggests, the mats analyzed with EDXS under 15kV and 7mm working distance exhibit the zinc and oxygen content. There is a very small amount of carbon observed in the system which is coming from the coating to overcome charging in the sample while SEM imaging.

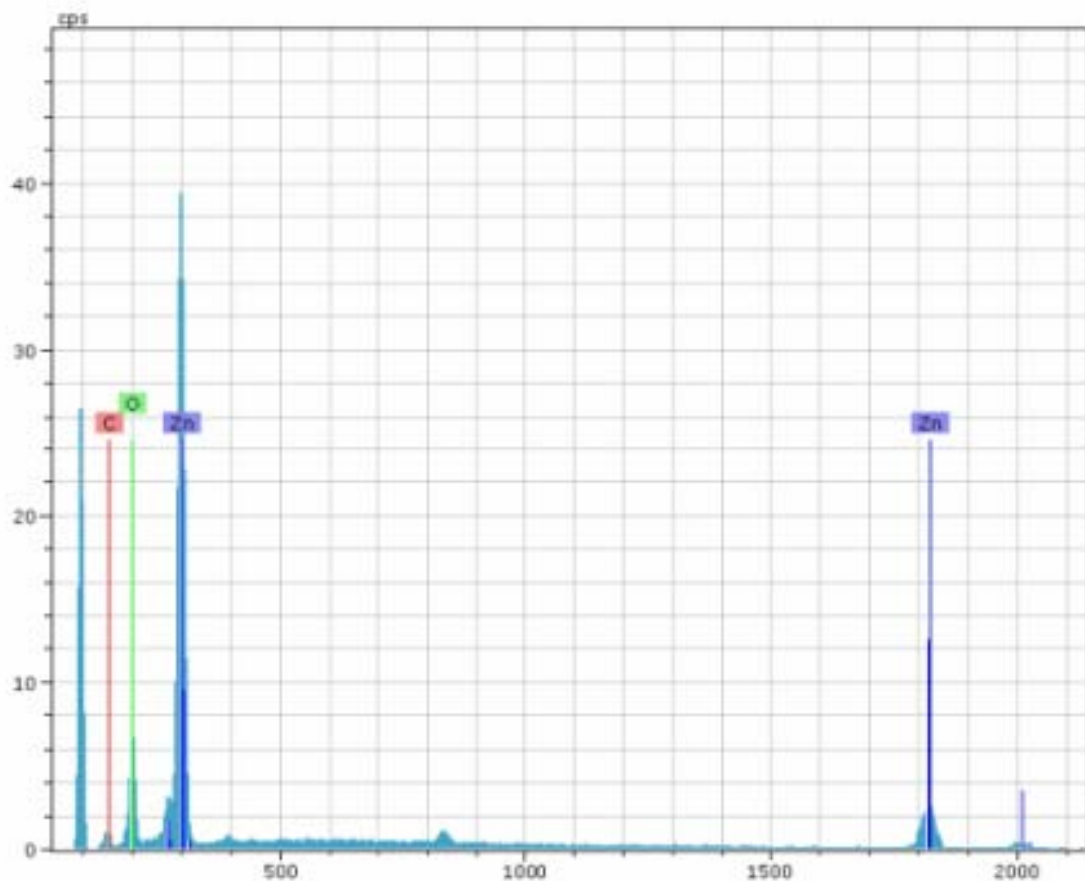


Figure 55 EDXS result showing the zinc and oxygen content of the fiber mat.

6.3.2.2 XRD Measurements

Furthermore, the XRD measurements gave exactly the desired crystallinity, wurtzite structure. The reflection angles coming from the specific crystal planes perfectly match with that of the zinc oxide in the software's library. It is significant to observe this crystal structure since the electroactive characteristic of ZnO comes from this crystal properties.

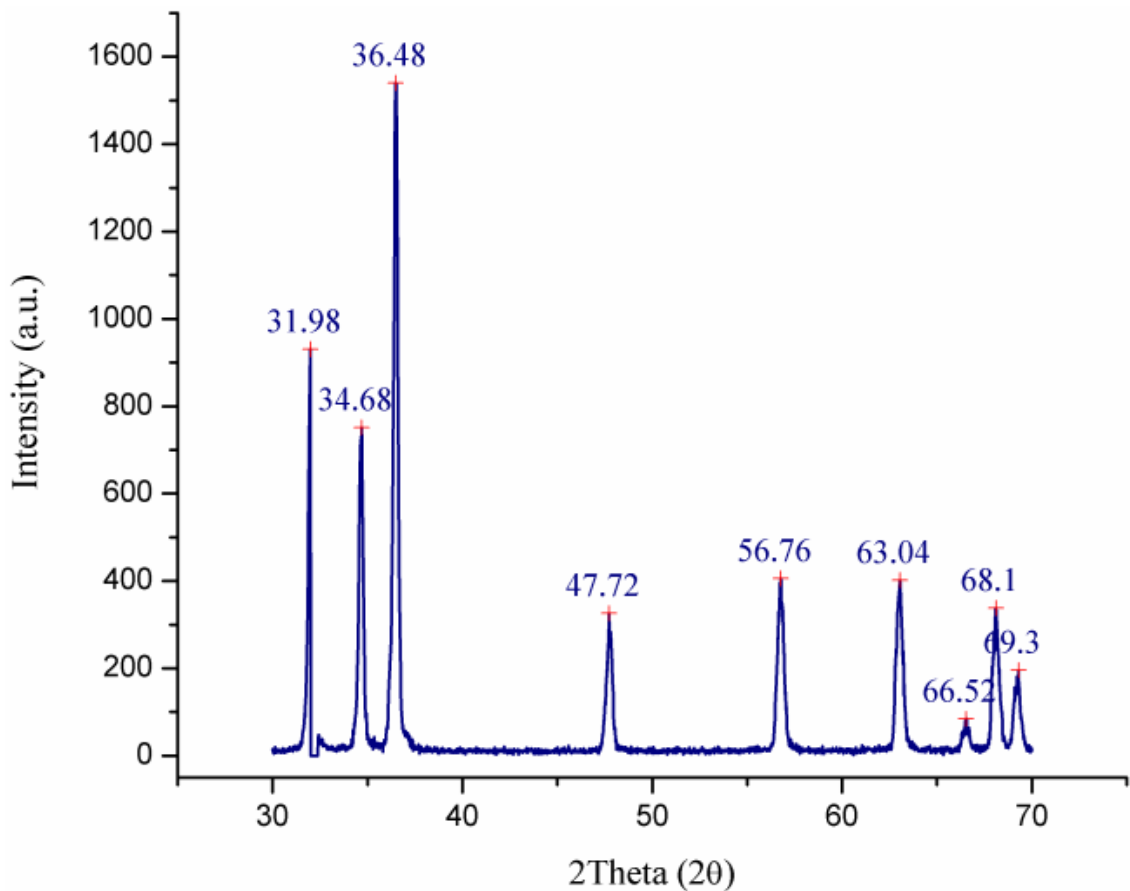


Figure 56 XRD data obtained from ZnO samples. The peaks are similar to the characteristic peaks of the wurtzite structure.

6.3.3 ZnO Whisker and Rod Formation

In addition to the ZnO fiber formation, it is given in Figure 57 and Figure 58 that whiskers and rods of ZnO structures grow in the structure without any thermal control

during calcination. To the author's knowledge, rod and whisker formation via electrospinning is documented for the first time.

Higher temperature sintering and longer periods of thermal process is applied on the sample, yet, control over these one-dimensional structures could not be obtained. However, the formation of these micrometer scale structures is significant in terms of the composites production. With the application of micro-gripping technology these micro-rods and –whiskers can be inserted in resins and the composite structure might be used as an actuator due to these ZnO rods and whiskers.

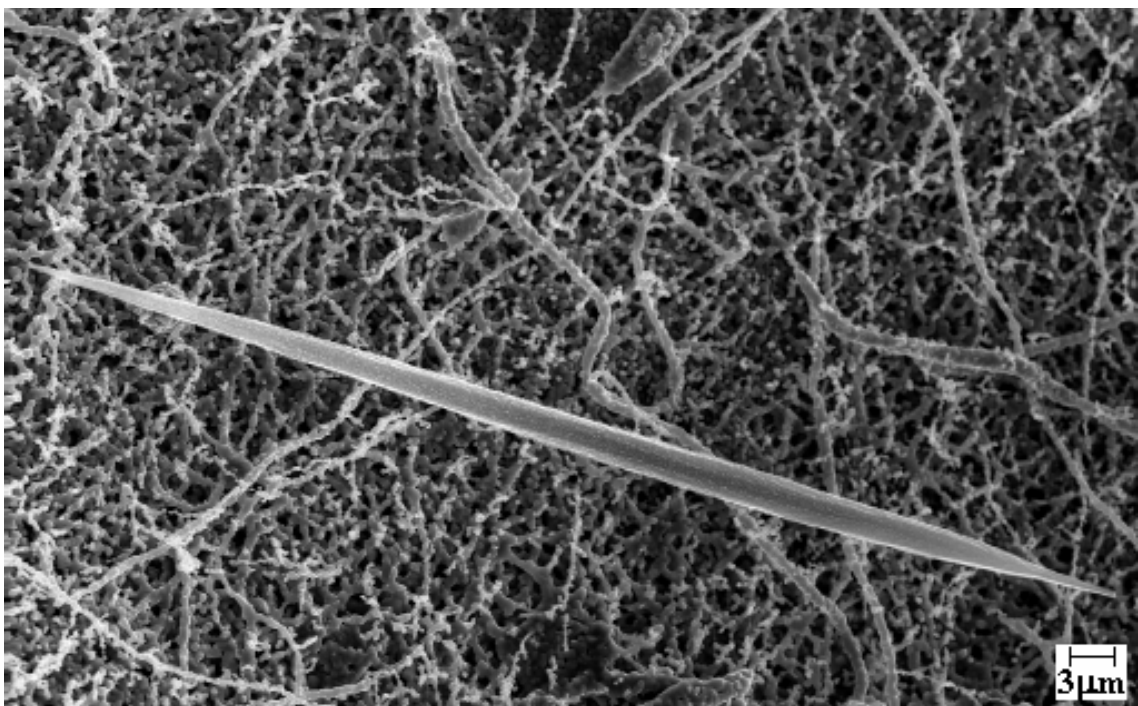


Figure 57 ZnO whisker formation during calcination.

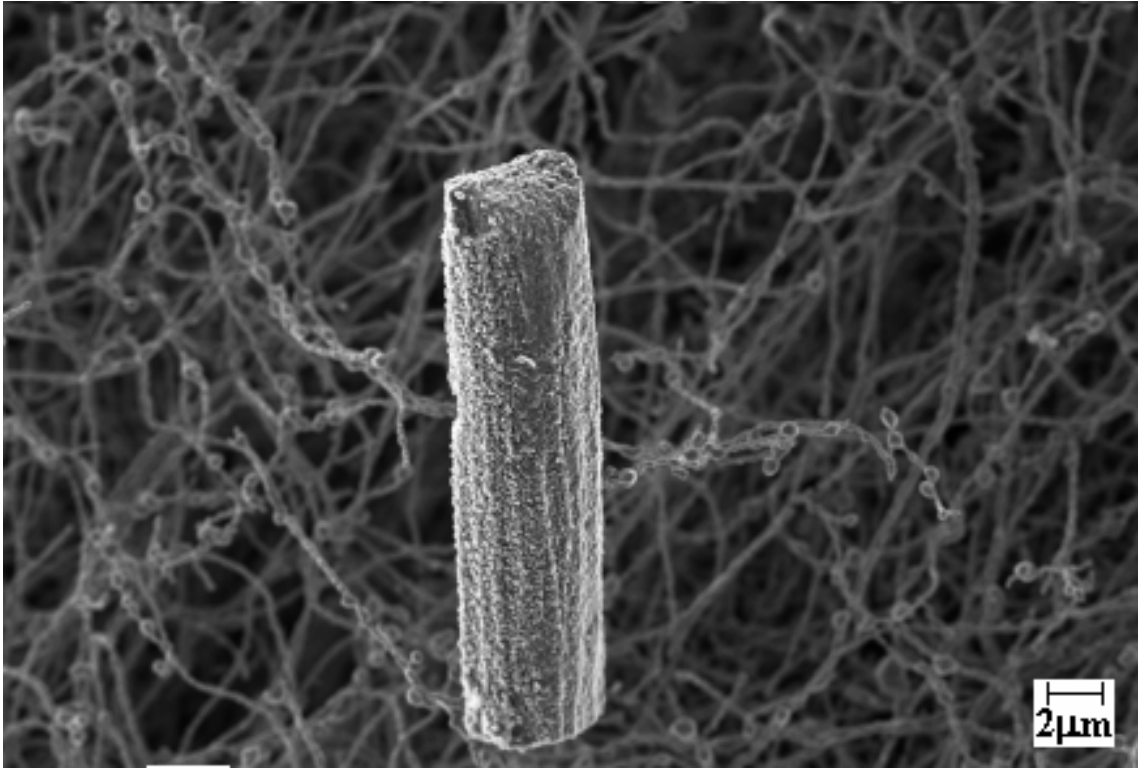


Figure 58 ZnO rod formation.

7. SUGGESTIONS AND FUTURE WORK

The major focus of this study was to understand the material properties and characterize the materials of interest towards an electroactive application. Following the characterization schemes, there has been a great amount of work in poling and measuring the piezoelectric coefficients of the materials. Yet, as Murphy suggests, “*new systems generate new problems*” and materials and systems in this study obeyed this rule!

Poling the solution cast films has been tried with the home-made set-up. Different electrodes, copper tapes, graphite sprays, carbon coating and gold coating was applied. Nevertheless, all generated some problems, yet gold has been concentrated on as electrode material, which has the least drawbacks. The problem with carbon and graphite is that when a voltage is generated on the electrode, carbon and graphite evaporates after 600 Volts. Copper tape has no material-induced problems, but, it is rather thick and resists the motion of the thin polymer film. Gold appears to be the best; however, it has a problem of thickness uniformity, thus a problem of current flow homogeneity. Efforts on poling the gold coated PVDF films are ongoing.

Electrospun PVDF mat is the new material system introduced in this study. The characterization results exhibit prominent outcomes. However, Murphy is at the scene again! Electrospun samples are porous by nature. The porosity introduced in the system is prone to serious problems in poling the samples, that is, the pores in the mat let current flow through one electrode to another as the dielectric breakdown of air occurs. Thus, it becomes difficult to apply high voltages on the sample.

Another material system, zinc oxide fiber mats, has a different type of problem. Due to the fiber structure discussed in 6, the mats are fragile. Fragility of the samples

has been tried to eliminate by sintering, yet, very low enhancement is gained. It is expected, though, the mat will hold itself when introduced into a composite structure.

This study should be followed by further piezoelectric characterization of PVDF and ZnO films beyond the crystalline structures that are signature of the piezoelectric potential. Then the two systems may be considered in making composite material to enhance the sensing and actuation properties of the individual materials. A final study might cover the modeling of these materials in different loading conditions.

8. CONCLUDING REMARKS

Two material systems that will be ingredients of a future piezo-composite film were investigated: piezoelectric polymer PVDF and ceramic ZnO. The process development and characterization of the material systems were reported. The polymer system PVDF was processed by solution casting and annealing to form active films. It was also processed by electrospinning and crystalline structures of the films and mats were compared for piezoelectricity.

Electrospinning of Poly(vinyl alcohol)-Zincacetate precursor solutions were also under investigation to produce randomly oriented polymer and ceramic fiber mats, respectively. The highlights and concluding remarks from this investigation are given as follows:

- Solution cast films were produced at different temperature and processing times to monitor the effect of annealing on the β -phase formation. Favorable processing range of temperature and time was found between temperatures 50⁰C and 60⁰C for two hours. Films transform better into β -phase when they were produced at this range.
- Un-stretched and stretched solution cast films were characterized by FT-IR, NMR, XRD, and DSC to exhibit the β -phase transformation due to stretching of the films. Stretched samples of the solution cast films display higher β -phase content.
- Process optimization of electrospinning of PVDF was carried out targeting for uniform fiber mat fabrication. Solution properties were initially adjusted by varying the solvent type, DMF and Acetone, and their mixing ratios. It was found and presented in 5.4.1 that 50% Acetone/DMF ratio produces fiber with uniform diameter and morphology resulting planar and uniform mats.

- A response surface approximation as a function of applied voltage and collector distance was constructed in order to predict the fiber diameter in the experimental design space as given in detail in 5.4.2.2.

- Electrospun samples were also characterized by XRD and DSC to monitor their β -phase content. It was observed as reported in section 5.4.3 that the samples were made of β -phase dominant semi-crystalline PVDF fibers resulting from the stretching effect during spinning. To the author's knowledge, a correlation between applied electric field and β -phase transformation was observed and reported for the first time.

- Tensile strength of the solution cast and electrospun films were also investigated. It is observed in sections 4.3.1.4, 4.3.2.3, and 5.4.3.3 that elastic moduli of electrospun samples are lower than that of solution cast ones. This finding is attributed to the random orientation of fibers and porous structure of mats, in which the cross-sections of the samples are misleading as opposed to uniform and homogeneous solution cast films.

- Process of zinc oxide nano-fiber production was also optimized by varying the precursor ingredients and thermal treatment on the mats. It was found that a lower heating rate and hanging the sample during the thermal process prevents the fibers to break. Moreover, precursor solution concentration significantly affects the final zinc content and zinc oxide fiber morphology as given in Chapter 6.

- Nano-scale zinc oxide fibers are composed of smaller zinc oxide ball-like structures in a continuous array. However, it was concluded that the boundaries created between the zinc oxide balls make the fiber fragile and difficult to handle. These boundaries act as cracks and eminently diminish the mechanical strength.

- Zinc oxide whiskers were manufactured by the electrospinning based process for the first time to the knowledge of the authors. ZnO rods were also formed during the calcination process. Efforts toward the whisker fabrication did not lead to control as it was observed that sintering temperature and duration did not affect the amount of whiskers and rods.

REFERENCES

1. Benz, M., Euler W. B. 2002. "Determination of the Crystalline Phases of PVDF Under Different Preparation Conditions Using Differential Scanning Calorimetry and Infrared Spectroscopy," *Journal of Applied Polymer Science*, 89(1093).
2. Lane, R., Craig B. *Materials that sense and respond*. The AMPTIAC Quarterly, US Department of Defense, 2003, 7, 2, 8-14.
3. Tung, S., Witherspoon S. 2005. "Electroactive-polymer actuators for controlling space inflatable structures," *Journal of Spacecraft and Rockets*, 42(4):607-612.
4. Dargaville, T. R., Celina M., Chaplya P. M. 2005. "Evaluation of Piezoelectric Poly(vinylidene fluoride) Polymer for Use In Space Environments. I. Temperature Limitations," *Journal of Polymer Science Part B: Polymer Physics*, 43(1310).
5. Mazzone, A., Zhang R., Kunz A. 2003. "Novel Actuators for Haptic Displays Based on Electroactive Polymers," *VRST*,
6. Bar-Cohen, Y. 2001. *Electroactive Polymer (EAP) Actuator as Artificial Muscles - Reality, Potential, and Challenges*. SPIE,
7. Bar-Cohen, Y. 2002. *Electroactive polymers and rapid prototyping*. Materials Research Society,
8. Bar-Cohen, Y. Year. *Biologically Inspired Intelligent Robots Using Artificial Muscles*. International Conference on MEMS, NANO, and Smart Systems 2003;
9. Japan, E. Year. 5th SPIE Conference - EAP Actuators & Devices 2003;
10. Liu, C. Year. *Scaling Laws of Microactuators and Potential Applications of Electroactive Polymers in MEMS*. SPIE's 6th Annual International Symposium on Smart Structures and Materials 1999;3669-33.
11. Choi, H. R., Jung K., Ryew S., Nam J. D., Jeon J., Koo J. C., Tanie K. 2005. "Biomimetic soft actuator: Design, modeling, control, and applications," *IEEE-Asme Transactions on Mechatronics*, 10(5):581-593.

12. Bauer, F. Year. *Ferroelectric Polymers for High Pressure and Shock Compression Sensors*. MRS November 26-27 2001;698: EE2.3.
13. Gu, H., Zhao Y., Wang M. L. 2005. "A wireless smart PVDF sensor for structural health monitoring," *Structural Control & Health Monitoring*, 12(3-4):329-343.
14. Kim, G. 2004. "Electroactive Polymer Composites as a Tactile Sensor for Biomedical Applications," *Macromolecular Research*, 12(6):564.
15. Kwon, O. Y., Dzenis Y. A. 2004. "Embedded PVDF film sensor for in-situ monitoring of structural integrity of laminated composites," *Advances in Nondestructive Evaluation, Pt 1-3*, 270-273(1929-1934).
16. Lee, Y. S. 2005. "A new position sensor using a triangularly shaped piezoelectric PVDF film," *Advances in Fracture and Strength, Pts 1- 4*, 297-300(2115-2121).
17. Moran, C. O. G., Ballesteros R. G., Guzman M. D. A. R., Gomez E. S. 2005. "Polyvinylidene fluoride polymer applied in an intraocular pressure sensor," *Japanese Journal of Applied Physics Part 2-Letters & Express Letters*, 44(24-27):L885-L887.
18. Ryu, J., Park J., Kim B., Park J. O. 2005. "Design and fabrication of a largely deformable sensorized polymer actuator," *Biosensors & Bioelectronics*, 21(5):822-826.
19. Bharti, V., Nath R. 2001. "Piezo-, pyro- and ferroelectric properties of simultaneously stretched and corona poled extruded poly(vinyl chloride) films," *Journal of Physics D-Applied Physics*, 34(5):667-672.
20. Sarkisov, S. S., Curley M. J., Huey L., Fields A., Sarkisov S. S., Adamovsky G. 2006. "Light-driven actuators based on polymer films," *Optical Engineering*, 45(3):-.
21. Fu, Y., Harvey E. C., Ghantasala M. K., Spinks G. M. 2006. "Design, fabrication and testing of piezoelectric polymer PVDF microactuators," *Smart Materials & Structures*, 15(1):S141-S146.
22. Kawai, H. 1969. "The Piezoelectricity of Poly(vinylidene fluoride)," *Japanese Journal of Applied Physics*, 8(975).
23. Sunar, M., Rao S. S. 1999. "Recent advances in sensing and control of flexible structure via piezoelectric materials technology," *Applied Mechanics Reviews*, 52(1-16).
24. Lee, C. S., Joo J., Han S., Koh S. K. 2004. "Multifunctional transducer using poly(vinylidene fluoride) active layer and highly conducting poly(3,4-

- ethylenedioxythiophene) electrode: Actuator and generator," *Applied Physics Letters*, 85(10):1841-1843.
25. Gao, P., Swei S. M. 2000. "Active actuation and control of a miniaturized suspension structure in hard-disk drives using a polyvinylidene-fluoride actuator and sensor," *Measurement Science & Technology*, 11(2):89-94.
 26. Lee, Y.-S., Elliott S. J., Gardonio P. 2003. "Matched piezoelectric double sensor/actuator pairs for beam motion control," *Smart Materials & Structures*, 12(541-548).
 27. Broadhurst, M. G., Davis G. T. 1980. *Electrets*. Springer-Verlag, pp283.
 28. Harrison, J. S., Ounias Z. 2001. *Piezoelectric Polymers*. NASA Langley Research Center, 2001-43, NASA/CR-2001-211422.
 29. Nalwa, H. S. 1995. *Ferroelectric polymers chemistry, Physics, and applications*. Marcel Dekker Inc.,
 30. Gregorio, R., Cestari M. 1994. "Effect of Crystallization Temperature on the Crystalline Phase Content and Morphology of Poly(Vinylidene Fluoride)," *Journal of Polymer Science Part B-Polymer Physics*, 32(5):859-870.
 31. Nakamura, K., Sawai D., Watanabe Y., Taguchi D., Takahashi Y., Furukawa T., Kanamoto T. 2003. "Effect of Annealing on the Structure and Properties of Poly(vinylidene fluoride) β -Form Films," *Journal of Polymer Science Part B: Polymer Physics*, 41(1701).
 32. Matsushige, K., Nagata K., Imada S., Takemura T. 1980. "The II-I crystal transformation of poly(vinylidene fluoride) under tensile and compressional stresses," *Polymer*, 21(1391-1397).
 33. Davis, G. T., McKinney J. E., Broadhurst M. G., Roth S. C. 1978. "Electric-field-induced phase changes in poly(vinylidene fluoride)," *Journal of Applied Physics*, 49(10):4998-5002.
 34. Bodhane, S. P., Shirodkar V. S. 1997. "Change in Crystallinity of Poly(vinylidene fluoride) Due to Thermal Evaporation," *Journal of Applied Polymer Science*, 64(2):225.
 35. Salimi, A., Yousefi A. A. 2004. "Conformational Changes and Phase Transformation Mechanisms in PVDF Solution-Cast Films," *Journal of Polymer Science Part B: Polymer Physics*, 42(18):3487.
 36. Reneker, D. H., Chun I. 1996. "Nanometre diameter fibres of polymer, produced by electrospinning," *Nanotechnology*, 7(216).

37. Baumgarten, P. K. 1971. "Electrostatic Spinning of Acrylic Fibers," *Journal of Colloid and Interface Science*, 36(1):71.
38. Demir, M. M., Yilgor I., Yilgor E., Erman B. 2002. "Electrospinning of Polyurethane fibers," *Polymer*, 43(3303).
39. Doshi, J., Reneker D. H. 1995. "Electrospinning Process And Applications Of Electrospun Fibers," *Journal of Electrostatics*, 35(2-3):151.
40. Grafe, T. H., Graham K. M. Year. *Nanofiber Webs from Electrospinning*. Nonwovens in Filtration - Fifth International Conference 2003;1.
41. Li, D., Xia Y. 2004. "Electrospinning of Nanofibers: Reinventing the Wheel?," *Advanced Materials*, 16(14):1151.
42. Matthews, J. A., Wnek G. E., Simpson D. G., Bowlin G. L. 2003. "Electrospinning of Collagen Nanofibers," *Biomacromolecules*, 3(2):232.
43. Pawlowski, K. J., Belvin H. L., Raney D. L., Su J., Harrison J. S., Siochi E. J. 2003. "Electrospinning of a micro-air vehicle wing skin," *Polymer*, 44(4):1309-1314.
44. Ramakrishna, S., Kujihara K., Teo W.-E., Lim T.-C., Ma Z. 2005. *An introduction to electrospinning and nanofibers*. World Scientific Publishing Co. Pte. Ltd.,
45. Subbiah, T., Bhat G. S., Tock R. W., Parameswaran S., Ramkumar S. S. 2005. "Electrospinning of Nanofibers," *Journal of Applied Polymer Science*, 96(557).
46. Zhao, Z. Z., Li J. Q., Yuan X. Y., Li X., Zhang Y. Y., Sheng J. 2005. "Preparation and properties of electrospun poly(vinylidene fluoride) membranes," *Journal of Applied Polymer Science*, 97(2):466-474.
47. Nasir, M., Matsumoto H., Danno T., Minagawa M., Irisawa T., Shioya M., Tanioka A. 2006. "Control of Diameter, Morphology, and Structure of PVDF Nanofiber Fabricated by Electro Spray Deposition," *Journal of Polymer Science Part B-Polymer Physics*, 44(779-786).
48. Choi, S. S., Lee Y. S., Joo C. W., Lee S. G., Park J. K., Han K. S. 2004. "Electrospun PVDF nanofiber web as polymer electrolyte or separator," *Electrochimica Acta*, 50(2-3):339-343.
49. Kim, J. R., Choi S. W., Jo S. M., Lee W. S., Kim B. C. 2004. "Electrospun PVdF-based fibrous polymer electrolytes for lithium ion polymer batteries," *Electrochimica Acta*, 50(1):69-75.
50. Seoul, C., Kim Y.-T., Baek C.-K. 2003. "Electrospinning of Poly(vinylidene fluoride)/Dimethylformamide Solution with Carbon Nanotubes," *Journal of Polymer Science Part B-Polymer Physics*, 41(1572-1577).

51. Wang, Z. L., Kong X. Y., Ding Y., Gao P. X., Hughes W. L., Yang R. S., Zhang Y. 2004. "Semiconducting and piezoelectric oxide nanostructures induced by polar surfaces," *Advanced Functional Materials*, 14(10):943-956.
52. Roy, S., Basu S. 2002. "Improved zinc oxide film for gas sensor applications," *Bulletin of Materials Science*, 25(6):513-515.
53. Pal, B., Sharon M. 2002. "Enhanced photocatalytic activity of highly porous ZnO thin films prepared by sol-gel process," *Materials Chemistry and Physics*, 76(82-87).
54. Xu, C. X., Sun X. W., Chen B. J., Shum P. 2004. "Nanostructural zinc oxide and its electrical and optical properties," *Journal of Applied Physics*, 95(2):661-666.
55. Viswanathamurthi, P., Bhattarai N., Kim H. Y., Lee D. R. 2004. "The photoluminescence properties of zinc oxide nanofibres prepared by electrospinning," *Nanotechnology*, 14(320-323).
56. Martin, P. M., Good M. S., Johnston J. W., Bond L. J., Lin J. D. 2000. "Piezoelectric films for 100MHz ultrasonic transducers," *Thin Solid Films*, 379(253-258).
57. Zhao, M. H., Wang Z. L., Mao S. X. 2004. "Piezoelectric characterization of individual zinc oxide nanobelt probed by piezoresponse force microscope," *Nano Letters*, 4(4):587-590.
58. Gao, P. X., Wang Z. L. 2005. "Nanoarchitectures of semiconducting and piezoelectric zinc oxide," *Journal of Applied Physics*, 97(4):-.
59. Fan, Z., Lu J. G. 2005. "Zinc Oxide Nanostructures: Synthesis and Properties," *Journal of Nanoscience and Nanotechnology*, 5(10):1561-1573.
60. Milosevic, I., Stevanovic V., Tronc P., Damnjanovic M. 2006. "Symmetry of zinc oxide nanostructures," *Journal of Physics-Condensed Matter*, 18(6):1939-1953.
61. Tian, Z. R. R., Voigt J. A., Liu J., McKenzie B., McDermott M. J., Rodriguez M. A., Konishi H., Xu H. F. 2003. "Complex and oriented ZnO nanostructures," *Nature Materials*, 2(12):821-826.
62. Dai, Y., Zhang Y., Bai Y. Q., Wang Z. L. 2003. "Bicrystalline zinc oxide nanowires," *Chemical Physics Letters*, 375(96-101).
63. Wang, Z. L., Song J. H. 2006. "Piezoelectric nanogenerators based on zinc oxide nanowire arrays," *Science*, 312(5771):242-246.

64. Shen, G. Z., Cho J. H., Yoo J. K., Yi G. C., Lee C. J. 2005. "Synthesis and optical properties of S-doped ZnO nanostructures: Nanonails and nanowires," *Journal of Physical Chemistry B*, 109(12):5491-5496.
65. Ding, Y., Kong X. Y., Wang Z. L. 2004. "Doping and planar defects in the formation of single-crystal ZnO nanorings," *Physical Review B*, 70(23):-.
66. Kong, X. Y., Ding Y., Yang R., Wang Z. L. 2004. "Single-crystal nanorings formed by epitaxial self-coiling of polar nanobelts," *Science*, 303(5662):1348-1351.
67. Xu, X. Y., Zhang H. Z., Zhao Q., Chen Y. F., Xu J., Yu D. P. 2005. "Patterned growth of ZnO nanorod arrays on a large-area stainless steel grid," *Journal of Physical Chemistry B*, 109(5):1699-1702.
68. Zhang, Y. S., Yu K., Jiang D. S., Zhu Z. Q., Geng H. R., Luo L. Q. 2005. "Zinc oxide nanorod and nanowire for humidity sensor," *Applied Surface Science*, 242(1-2):212-217.
69. Qi, X. Q., Tao D. L., Huang Y., Ling C., Xu Y. Z., Wei F., Wu J. G., Xu D. F. 2005. "The study on the growth process of ZnO nanorods," *Spectroscopy and Spectral Analysis*, 25(3):321-325.
70. Jie, J. S., Wang G. Z., Chen Y. M., Han X. H., Wang Q. T., Xu B., Hou J. G. 2005. "Synthesis and optical properties of well-aligned ZnO nanorod array on an undoped ZnO film," *Applied Physics Letters*, 86(3):-.
71. Yu, K., Zhang Y. S., Xu R. L., Jiang D. S., Luo L. Q., Li Q., Zhu Z. Q., Lu W. 2005. "Field emission behavior of cuboid zinc oxide nanorods on zinc-filled porous silicon," *Solid State Communications*, 133(1):43-47.
72. Chronakis, I. S. 2005. "Novel nanocomposites and nanoceramics based on polymer nanofibers using electrospinning process-A review," *Journal of Materials Processing Technology*, 167(283-293).
73. Dzenis, Y., Feng R., Larsen G., Turner J., Zeng X. Year. *Manufacturing of Novel Continuous Nanocrystalline Ceramic Nanofibers with Superior Mechanical Properties*. NSF Nanoscale Science and Engineering Grantees Conference 2003;
74. Sigmund, W., Yuh J., Park H., Maneeratana V., Pyrgiotakis G., Daga A., Taylor J., Nino J. C. 2006. "Processing and Structure Relationships in Electrospinning of Ceramic Fiber Systems," *Journal of American Ceramic Society*, 89(2):395-407.
75. Wu, H., Pan W. 2006. "Preparation of Zinc Oxide Nanofibers by Electrospinning," *Journal of American Ceramic Society*, 89(2):699-701.

76. Umar, A., Hahn Y. B. 2006. "Aligned hexagonal coaxial-shaped ZnO nanocolumns on steel alloy by thermal evaporation," *Applied Physics Letters*, 88(17):-.
77. Wang, Y. C., Leu I. C., Hon M. H. 2002. "Preparation of nanosized ZnO arrays by electrophoretic deposition," *Electrochemical Solid State Letters*, 5(C53-C55).
78. Li, Y., Meng G. W., Zhang L. D., Philipp F. 2001. "Ordered semiconductor ZnO nanowire arrays and their photoluminescence properties," *Applied Physics Letters*, 76(2011-2013).
79. Wang, Y., Aponte M., Leon N., Ramos I., Furlan R., Pinto N. 2005. "Synthesis and Characterization of Ultra-Fine Tin Oxide Fibers Using Electrospinning," *Journal of American Ceramic Society*, 88(8):2059-2063.
80. Wu, H., Pan W. 2006. "Preparation of Zinc Oxide Nanofibers by Electrospinning," *Journal of American Ceramic Society*, 89(699).
81. Yang, X., Shao C., Guan H., Li X., Gong J. 2004. "Preparation and characterization of ZnO nanofibers by using electrospun PVA/zinc acetate composite fiber as precursor," *Inorganic Chemistry Communications*, 7(176-178).
82. Brown, L. F. 2000. "Design Consideration of Piezoelectric Polymer Ultrasound Transducers," *IEEE Transactions and Ultrasonics, Ferroelectrics, and Frequency Control*, 47(1377-1396).
83. Brown, L. F. 1996. "Disposable PVDF Ultrasonic Transducers for Nondestructive Testing Applications," *ibid*, 43(560-567).
84. Stiffler, R., Henneke E. G. 1983. "The Application of Polyvinylidene Fluoride as an Acoustic Emission Transducer for Fibrous Composite Materials," *Materials Evaluation*, 41(956-960).
85. Omote, K., Ohigashi H. 1996. "Properties of Transverse Ultrasonic Transducers of Ferroelectric Polymers Working in Thickness Shear Modes," *ibid*, 43(312-317).
86. Poizat, C., Sester M. 1999. "Effective properties of composites with embedded piezoelectric fibers," *Computational Materials Science*, 16(89-97).
87. Su, J., Xu T.-B., Zhang S., Shrouf T. R., Zhang Q. 2004. "An electroactive polymer-ceramic hybrid actuation system for enhanced electromechanical performance," *Applied Physics Letters*, 85(6):1045-1047.
88. Wikipedia. 2006. "*dielectric materials*", 09 June 2006.
89. Priya, L., Jog J. P. 2003. "Polymorphism in Intercalated Poly(vinylidene fluoride)/Clay Nanocomposites," *Journal of Applied Polymer Science*, 89(2036-2040).

90. Pawlowski, K. J. 2004. *Electrospinning as a processing method for electroactive polymers and composites*. Virginia Commonwealth University, Richmond, Virginia;
91. Formhals, A. US Patent, 1975504; 1934.
92. Deitzel, J. M., Kleinmeyer J., Harris D., Tan N. C. B. 2001. "The effect of processing variables on the morphology of electrospun nanofibers and textiles," *Polymer*, 42(261).
93. Larrondo, L., Manley J. 1981. "Electrostatic Fiber Spinning from Polymer Melts. I. Experimental Observations on Fiber Formation and Properties," *Journal of Polymer Science, Part B: Polymer Physics*, 19(909).
94. Zacharides, A. E., Porter R. S., Doshi J., Srinivasan G., Reneker D. H. 1995. *Polymer News*, 20(206).
95. Kattamuri, N., Sung C. 2004. "Uniform Polycarbonate Nanofibres Produced By Electrospinning," *Macromolecules*, 3(425).
96. Sukigara, S., Gandhi M., Ayutsede J., Micklus M., Ko F. 2004. "Regeneration of Bombyx Mori silk by electrospinning. Part 2. Process Optimization and empirical modelling using response surface methodology," *Polymer*, 45(3701).
97. Mo, X. M., Xu C. Y., Kotaki M., Ramakrishna S. 2004. "Electrospun P(LLA-CL) nanofiber: a biomimetic extracellular matrix for smooth muscle cell and endothelial cell proliferation," *Biomaterials*, 25(1883).
98. Pawlowski, K. J., Belvin H. L., Raney D. L., Su J., Harrison J. S., Siochi E. J. 2003. "Electrospinning of a micro-air vehicle wing skin," *Polymer*, 44(1309–1314).
99. Walpole, R. E., Myers R. H., Myers S. L., Ye K. 2002. *Probability and statistics for engineers and scientists*. Prentice Hall,
100. Montgomery, D. C. 2001. *Design and Analysis of Experiments*. John Wiley,
101. Montgomery, M. a. 1997. *Response Surface Methodology*. Wiley,
102. Yördem, O. S., Papila M., Menceloğlu Y. Z. Year. *Prediction of Electrospinning Parameters for Targeted Nanofiber Diameter*. Nanocomposites 2005 2005;
103. Ifju, P., Jenkins D., Ettinger S., Lian Y., Shyy S. 2002. "Flexible-Wing-Based Micro Air Vehicles," *AIAA*, 0705(
104. Vinogradov, A., Su J., Jenkins C., Bar-Cohen Y. Year. *State-of-the-art Developments in the Field of Electroactive Polymers*. Materials Research Society 2006;889: 0889-W02-05.1 - 0889-W02-05.6.

105. Buchanan, R. C. 2004. *Ceramic Materials for Electronics*. Marcel Dekker, Inc, pp676.
106. Pohl, A., Rosenfeldt H., Wendt E., Buesing K. *Hydraulic displacement machine*. Germany, 6149391; 2000.
107. Gelbman, G. *System and method for controlling the flow of a gaseous medium through a fluid*. Germany, 6186176; 2001.
108. Elsayed, M. A., Raymond D. W. *Controllable magneto-rheological fluid-based dampers for drilling*. United State of America, 7036612; 2006.
109. Mukherjee, A., Chaudhuri A. S. 2005. "Active Control of Piezolaminated Columns - Exact Solutions and Experimental Validation," *Smart Materials & Structures*, 14(475).
110. Xu, T.-B., Su J. 2005. "Theoretical Modelling of electroactive polymer-ceramic hybrid actuation systems," *Kournal of Applied Physics*, 97(034908-1 - 034908-7).
111. Cui, C., Baughman R. H., Iqbal Z., Kazmar T. R., Dahlstrom D. K.
112. Huang, C., Zhang Q. M., Su J. 2003. "High-dielectric-constant all-polymer percolative composites," *Applied Physics Letters*, 82(20):3502-3504.
113. TeCCenter, N. L. T. a. 2006. "*Electroactive Polymers*", May 23 2006.
114. Berlincourt, D. 1964. *J Acoust Soc Am*, 36(3):515.
115. Stroyan, J. J. 2004. *Processing and Characterization of PVDF, PVDF-TrFE, and PVDF-TrFE-PZT Composites*. Washington State University, Washington;
116. Livingston, J. D. 1999. *Electronic Properties of Engineering Materials*. Wiley,
117. Khuri, A. I., Cornell J. A. 1996. *Response Surfaces: Designs and Analyses*. Marcel Dekker Inc.,

APPENDICES

Appendix A: Preparatory Information on Electro-mechanical Activity and Electroactive Materials

Overview of Electroactive Materials

The inspiration of many of the technological developments comes from nature, such as humming birds' wing motions and skeletal movements of animals conveyed to all-scale robotics systems. These simple to observe but difficult to achieve mechanical activities have also ignited substantial amount of research to engineer materials capable of active and controlled responses to stimuli. "On this basis, a new generation of smart structures has emerged that can detect changes in the loading or environmental conditions, decide rationally on a set of the respective actions, and carry out these actions in a controlled manner"[104]. Electrically stimulated materials working in various environments, for instance, have provided such capabilities to compete with and mimic the complexity of the natural mechanical processes, particularly in the last two decades. These intricate electroactive materials have been expected to provide solutions in numerous industries for all-scale applications such as micro air vehicles and artificial muscles.

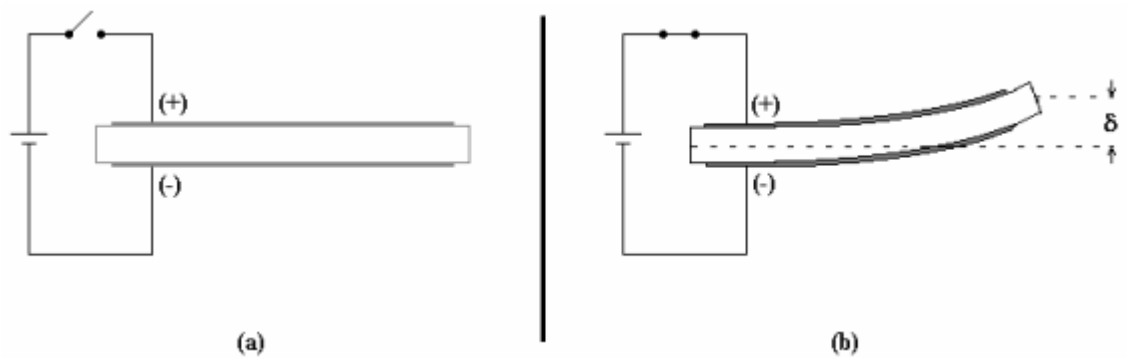


Figure 59 Schematically representation of electromechanical response of an electroactive material

There are number of materials, such as the electroactive ceramics, electro- or magneto-rheological and electroactive polymers (EAPs), offering active response, that is, they experience a significant change in their physical properties or spatial dimensions due to the applied electrical or thermal stimuli or vice versa, as schematically represented in Figure 59 and Figure 60.

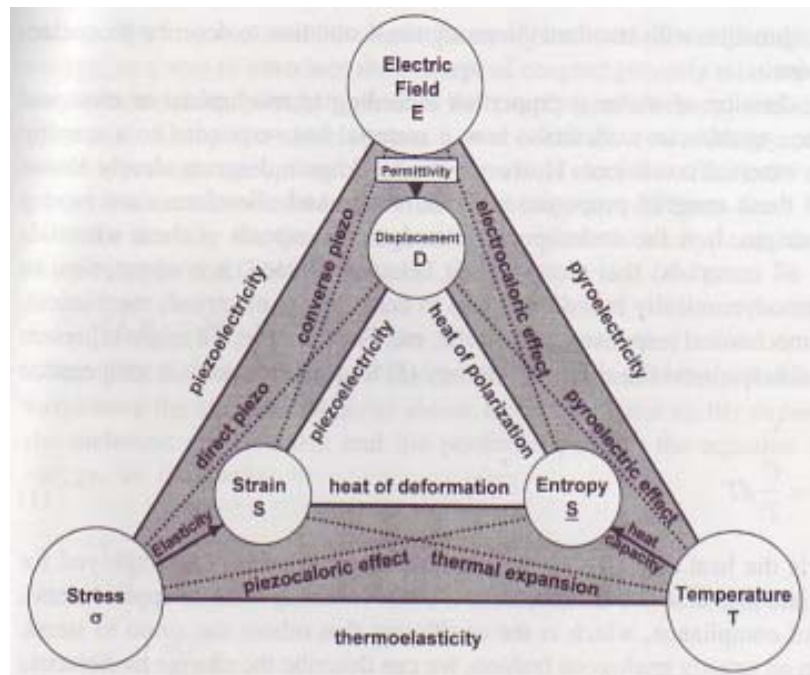


Figure 60 Heckman diagram showing the interrelationship among the mechanical, electrical, and thermal properties of materials. Coupled properties such as piezoelectric, pyroelectric, and thermal expansion are also given. Adapted from [105].

Ceramics have conventionally been admired for their mechanical and thermal stability, and several research fields of ceramics have become of increasing significance in many key technologies including communications, energy, automation, electronics, biology, and structures. One of the largest groups of ceramics, especially in the last two decades is the electroceramics. They have been under investigation due to their eminent applications in several industries such as computer hardware, microchips. A broad classification of electroceramics comprise piezoelectric, pyroelectric, ferroelectric, dielectric, semiconductor, electro-optic and electro-chromic ceramic materials. Piezoelectric ceramic materials have been under investigation for their active responses and their effective use in sensor and actuator applications. Piezoceramics most often have lead zirconate titanates (PZT), barium titanates (BT), strontium titanates (ST), and quartz based structures, which possess high strain response. Nevertheless, electroactive ceramics (EACs) are not easily malleable. Although there are studies on enhancing the mechanical properties of ceramic materials [73], they are generally fragile under plying.

Another type of electrically stimulated material, electro/magneto-rheological (ER-MR) fluid, is also defined as active/smart materials which perceive a drastic viscosity change under applied electric/magnetic field. These fluids have a very rapid response to an applied electric/magnetic field. The response time of electrorheological fluids is of the order of 1-10 ms, which, in principle enables the use of these liquids in applications such as electrically controlled clutches [106], valves [107] and active damping devices [108]. One of the most prominent applications of ER fluids is an artificial muscle made up of a suspension of polymer particles in a polymer gel. Besides their wide range of applicability for active response requirements, these structures are generally composed of a colloidal system in which a base fluid is reinforced with dielectric particles of sizes 0.1 – 100 μm with a volume fraction of 20 – 60% [104]. Although the physics behind their working principle is not clearly understood yet, the experimental outcomes exhibit a reversible change from a liquid state to a solid crystallized state due to an applied electric.

Another important branch of materials science comprises polymers, which have many attractive characteristics to various engineering and scientific applications. Their lightweight, low production costs, fracture tolerance, flexibility, and sometimes their biodegradability made polymers very alluring to several industries. Furthermore, they can be configured into almost any shape, and with the help of their superior physical properties, they can be modified to suit a broad range of functions. This capability of the electroactive polymers (EAPs) has become appealing to numerous industries for their inexpensive, lightweight and mechanically stable structures. They can undertake large amount of deformation while maintaining ample forces. They have expeditious response time, very low density, high strain output and eminent pliability when compared to electroactive ceramics and shape memory alloys. When the overall performance of the EAPs is investigated, the superior properties of EAPs among the piezoceramics and SMAs arise (Table 19). Their electroactive properties were investigated after the 1970s with the invention of the active property of a rubber band by Roentgen, and special consideration has been given ever since the 1990s [6].

Table 19 Comparison of properties of three active materials EAPs, SMAs, EACs
(adapted from [6])

Properties	EAPs	SMA	EACs
Actuation Strain	> 10%	< 8%	0.1 – 0.3%
Force (MPa)	0.1 - 3	About 700	30 – 40
Reaction Speed	µsec to min	sec to min	µsec to min
Density (g/cm ³)	1 – 2.5	5 -5	6 – 8
Drive Voltage	10 – 150 V/µm	not applicable	50 – 800 V
Consumed Power	m-watts	watts	watts
Fracture Toughness	resilient, elastic	elastic	fragile

Generally, the EAP materials can be classified in two parts according to their activation systems: ionic EAPs and electronic EAPs. Ionic polymers require low voltages with low frequencies to be activated (~5 V below 1Hz) but the ionic flow requires a high electrical power and the displacements produced in the structure due to the piezoelectric activity are not static at will, but alternating, that is, an energy is needed to keep the actuator at a given position (except for conductive polymers) [6]. In addition to this, the environment that the ionic polymers are working in should be kept wet, in order them to exert the desired properties efficiently. However, the electronic EAP materials, or the dielectric EAPs, can hold the induced displacement after an initial DC voltage, without requiring a continuous voltage generation to keep the actuator at some position. The response time is much faster than the ionic EAPs (in msec levels). Besides, the operation can be utilized in air without a further modification in the environment. They, however, may require large activation voltages, >150 V/µm [6]. Among the electronic EAP classes, the piezoelectric PVDF and its copolymers are the most widely applied materials in both actuation and sensing mechanisms. They can be utilized as fibers and films mostly in linear movement requirements in various engineering applications such as active micro air vehicle wings [43], piezolaminated columns [109], and shape correction films in space applications [3, 4].

Another type of smart material systems include the composite active materials, which are composed of two or more materials uniformly incorporated in one single system. A composite smart material, say composite actuator, comprises two distinct materials at minimum. One of the material systems is the active one, that is it responds

to the electrical or thermal stimuli applied, and the other one is generally used as a matrix material to hold the composite system as a whole.

Electroactive composite systems can be produced via several methods given in [105]. Many methods involve a polymeric inactive resin holding the active PZT in the desired spatial form. “This kind of technique improves the porosity volume and protects the active layer from mechanically or chemically corrosive environment” [105]. Besides the PZT induced polymeric resins as electroactive composites, there also have been hybrid smart structures which are composed of two or more active layers which can all be different PZT units, different polymeric parts or PZT-EAP hybrid systems. One EAP-ceramic hybrid actuation system was introduced by Xu et.al in which a uniaxially stretched and high-energy-irradiated PVDF-TrFE copolymer is joined with a rhombohedral oriented $\text{Pb}(\text{Zn}_{1/3}\text{Nb}_{2/3})\text{O}_3$ -4.5% PbTiO_3 crystal [110]. Another active hybrid system is introduced by Cui et al. which is composed of EDO EC-97 ceramic particles placed in the PVDF solution finally forming a piezoelectric ceramic particle/polymer composite [111]. There are also all polymer composites with dielectric constants introduced by Huang et al. which comprises PVDF-TrFE-CFTE mixed with PANI [112].

Piezoelectricity of Materials

Piezoelectricity is once succinctly defined by Caddy as “*electric polarization produced by mechanical strain in crystals belonging to certain classes, the polarization being proportional to the strain and changing sign with it*” [105].

The simplest definition of piezoelectric response is given as the development of an electrical charge under the application of a mechanical input. This characteristic is referred as the direct piezo electric effect, and the inverse action of this definition, development of a mechanical strain (deformation) due to an applied electric field, is referred as the converse piezoelectric effect. From an engineering point of view, the direct piezoelectric effect is classified in the sensor application of materials, whereas the converse piezoelectric effect is classified in the actuation mechanisms and energy harvesting in some applications (Table 2).

Table 20 Examples of piezoelectric devices and their applications (adapted and extended from [105] and [113])

Device Category	Typical Devices
Ultrasonic Generators	Ultrasonic cleaners, degreasers, sonar, pingers, atomizers, ultrasonic welding, intrusion alarms, pest control devices, flaw detectors, flow indicators, medical applications (imaging, therapy, insulin pumps, vaporizers)
Sensors	Phonograph pickups, accelometers, hydrophones, sonobuoys, depth sounders, auto diagnostic devices (knock sensors, tire pressure indicators, tread wear indicators, wheel balancers, keyless door entry, fuel automization), flaw detectors
Resonators	IF filters, surface wave filters, delay lines, piezo transformers, TV and radio resonators
Sounders	Loudspeakers, tweeters, tone generators, head sets, buzzers, alarms
Actuators	Tunable membrane structures (active wings), electromechanical transducers (MEMs applications), biomedical actuators (artificial muscle, implants to promote bone and tissue growth)
Miscellaneous	Relays, pumps, motors, fans, positioners, ink printers, alarm systems, smoke detectors, touch controls, power supplies, ignitors

The materials utilized for these applications are generally the ferroelectric ceramics, most often the PZTs, which have previously been discussed. In some applications, on the other hand, electroactive polymers have also been favored due to the mechanically and chemically resistive assets of polymers.

The fundamental deformations of a piezoelectric material, either a ceramic or polymer, are best illustrated in physical dimensions as a result of the application of a varying electric field on an electrode coated and poled plate or disk. It is essential to

know the direction of polarity and electric field for every material in order to predict the motion of the material. When an electric field in a direction same as the poling direction is applied, the expansion will occur in that direction; yet, when an opposite field is applied, opposite deformations will take place. As schematically represented by Buchanan, the typical examples of the deformations in plates and disks are given in Figure 61.

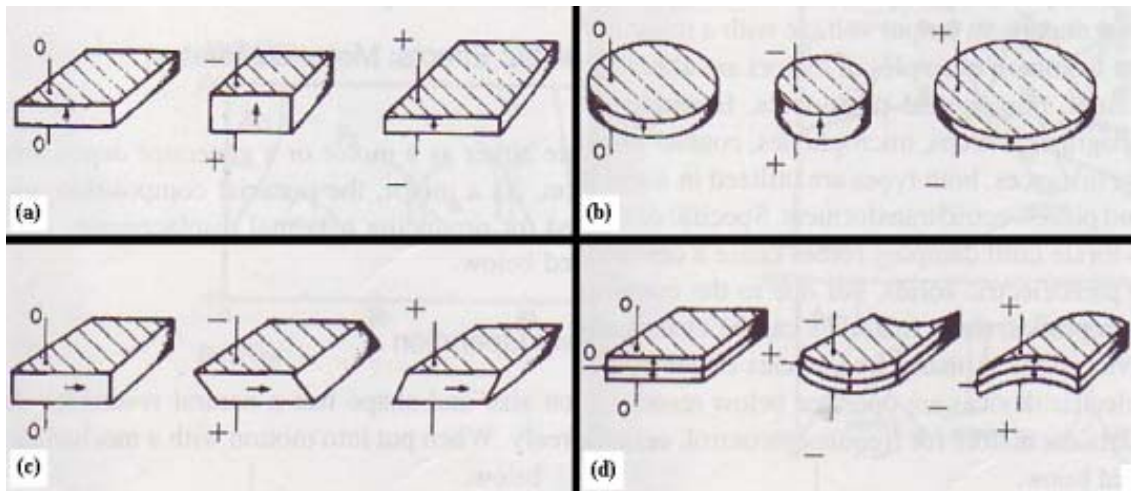


Figure 61 Typical mechanical deformations of poled piezoelectric plates when subjected to an electric field (a) thickness and length; (b) radial; (c) thickness shear; and (d) bender (e.g. bimorph structures). Adapted from [105].

Direct and Indirect Piezoelectric Effect

A piezoelectric material can operate either as an actuator or a sensor. The material type, configuration and composition of the actuators are optimized to gain the maximum displacement with a minimum voltage (converse piezoelectric effect) needed for a specific application. In the sensor applications on the other hand, the material composition and geometry is designed to achieve the maximum output voltage with a minimal input strain (direct effect).

Poling and Development of Electromechanical Response

Before the 1950s it was believed that only the single-crystal materials exhibit the piezoelectric property, however there are many ferroelectric materials which have

randomly distributed dipole moments in their molecular structure. When these dipole moment vectors are added up, the random orientation of the polarity cancels in the material and results in no electromechanical response. With the application of poling process, the ferroelectric materials exhibit an active electromechanical activity. Once the ferroelectric materials are poled, they act as a single entity characterized by the net macroscopic polarization that is induced by poling.

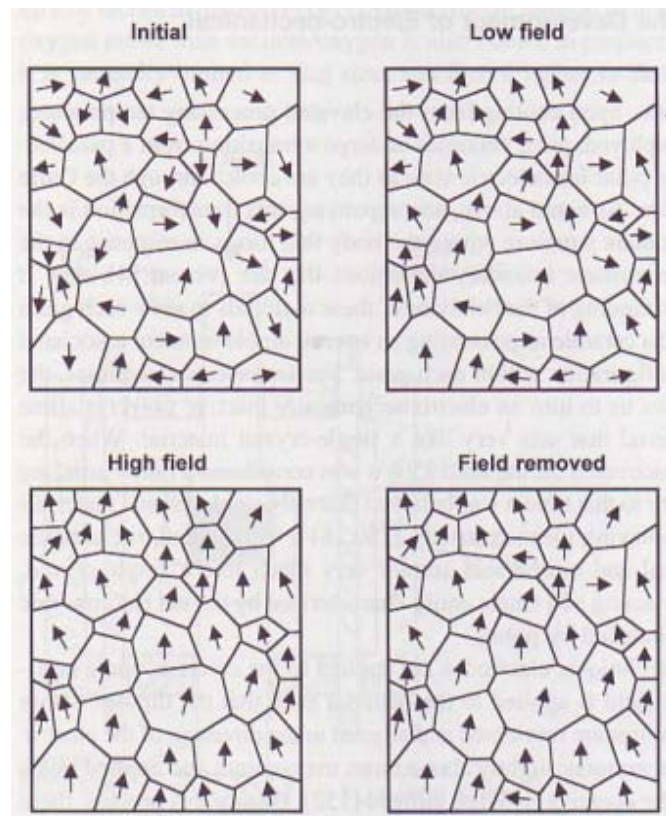


Figure 62 Schematically representation of microstructural changes during poling and after removal of poling.

There are several poling methods both for ceramics and polymers such as corona poling and vacuum poling. In the most common poling technique, electrodes are applied on each surface of the material such that the dipoles within the material are reoriented and aligned in the direction of the applied electric field (Figure 4). The poling medium, temperature and magnitude of voltage affect the quality of the poling process, and thus the resultant electromechanical response. Temperatures slightly above room temperature and applied fields three to four times the coercive field are typically employed on the material [114]. In reality, 100% reorientation or alignment is

ever complete due to the randomly oriented dipoles of original material, yet, some crystals (orthorhombic phase) present 91% conversion with this poling process.

Ferroelectric Effect and Ferroelectric Polymers

In order to understand the concept of ferroelectric effect and ferroelectric materials, one first needs to define the dielectric materials. *A dielectric, or an insulator, is a material that is highly resistant to the flow of electric current* [88]. Despite having no free electrons, dielectrics still contain a plenty of electric charge, and an applied electric field pushes the negative charges in one direction and positive charges in the opposite direction. The dielectric polarizes producing a net electric dipole moment per unit volume called polarization, which is a vector quantity, defined as pointing from negative to positive charge.

Ferroelectric effect is an electrical phenomenon where certain ionic crystals and piezoelectric polymers have symmetries that allow them to exhibit a spontaneous dipole moment in an absence of electric field, which can be reoriented by the application of an electric field. The most commercially available ferroelectric materials are based on the titania compounds with perovskite structure, such as BaTiO_3 and PbTiO_3 . In some limited temperature ranges these ceramic materials can have dielectric constants of several thousands due to the motion of ferroelectric domain walls. And these ferroelectric domain walls are one of the other significant properties of the ferroelectric materials. A domain is a microscopic region of a crystal the polarization is homogeneous. These domains are naturally un-aligned, yet they can be aligned in a desired direction by applying a DC electric field for an extended period of time by the method of poling (Figure 62) [115, 116].

Appendix B: Response Surface Methodology

Response surface methodology [101, 117] assumes that the RS expression is exact and that the differences (called residuals) between the data and the RS are due to uncorrelated, normally distributed random noise of magnitude ϵ in the experiments. Based on this assumption, if the true response is given in terms of n_b coefficients, β_i s and assumed shape functions f_i (usually monomials) as

$$y(\mathbf{x}) = \sum_{i=1}^{n_b} \beta_i f_i(\mathbf{x}) + \epsilon \quad (\text{A.1})$$

then the RS approximation \hat{y} is written as

$$\hat{y}(\mathbf{x}) = \sum_{i=1}^{n_b} b_i f_i(\mathbf{x}) \quad (\text{A.2})$$

where b_i s are unbiased estimates of the β_i s.

The difference (residual) e_j between the data y_j for the j^{th} point \mathbf{x}_j and the estimate defined in Equation (A.2) is given in matrix form for n_d data points as

$$\mathbf{e} = \mathbf{y} - \mathbf{X}\mathbf{b} \quad (\text{A.3})$$

where \mathbf{X} is the matrix whose component (j,i) is . The coefficient vector \mathbf{b} in Equation (A.3) is solved for the minimum residual vector in a least-square sense, to obtain

$$\mathbf{b} = (\mathbf{X}^T \mathbf{X})^{-1} \mathbf{X}^T \mathbf{y} \quad (\text{A.4})$$

where superscript \mathbf{T} denotes the transpose operation. An unbiased estimate of the noise s (the root mean square error estimator, RMSE) in the data is given as

$$s = \sqrt{\frac{\mathbf{y}^T \mathbf{y} - \mathbf{b}^T \mathbf{X}^T \mathbf{y}}{n_d - n_b}} \quad (\text{A.5})$$

In addition to s , the quality of the approximation is often measured by the coefficient of multiple determination, R^2 . An R^2 value larger than 0.9 is typically required for an adequate approximation. R^2 is a measure of the proportion of total variation of the values of y_i about the mean value of the response \bar{y} explained by the fitted model [101]. This coefficient is given as

$$R^2 = \frac{\sum_{j=1}^{n_d} (\hat{y}_j - \bar{y})^2}{\sum_{j=1}^{n_d} (y_j - \bar{y})^2} \quad (\text{A.6})$$

The variance-covariance matrix of the vector of estimates \mathbf{b} is estimated as

$$\text{Var}(\mathbf{b}) = (\mathbf{X}^T \mathbf{X})^{-1} s^2 \quad (\text{A.7})$$

The estimated standard deviation of i^{th} coefficient b_i (called standard error) is denoted by s_i , and is obtained as the positive square root of the i^{th} term of the diagonal of $\text{Var}(\mathbf{b})$. The hypothesis about the individual coefficients in the model can be tested by comparing the coefficient estimates to their respective estimated standard errors. Student's t-statistic

$$t = \frac{b_i}{s_i} \quad (\text{A.8})$$

is used to test the null hypothesis $H_0: \beta_i = 0$. This is a two-tailed test against the alternatives in each direction.

The p-value is the smallest significance level for which any of the tests would have rejected the null hypothesis. It represents an index of the reliability of a result. In

case of a null hypothesis $H_0: \beta_i = 0$ it is likely that the coefficient of a particular term is actually zero rather than the value calculated. The smaller *p-value* gets, the smaller is the chance of being wrong in accepting that the coefficient is different than zero, and that there is a relation between the response and the associated regression terms. The *p-value* for $H_0: \beta_i = 0$ can be determined by comparing the t-statistic obtained by (10) with the values in statistical tables of the Student distribution [117]. Probabilities of less than 0.05 are considered as significant evidence that the coefficient is not zero.

Appendix C: Effects of Electrospinning Parameters on Polyacrylonitrile Nanofiber Diameter: An Investigation by Response Surface Methodology

Abstract

Effects of material and process parameters on the diameter of electrospun Polyacrylonitrile fibers were experimentally investigated. Response surface methodology (RSM) was utilized to design the experiments at the settings of solution concentration, voltage and the collector distance. It also imparted the evaluation of the significance of each parameter on the resultant fiber diameter. The investigations were carried out in the two-variable process domains of several collector distances as applied voltage and the solution concentration were varied at a fixed polymer molecular weight. The mean diameter and coefficient of variation were modeled by polynomial response surfaces as functions of solution concentration and voltage at each collector distance. Effect of applied voltage in micron-scale fiber diameter was observed to be almost negligible when solution concentration and collector distance were high. However, all three factors were found statistically significant in the production of nano-scale fibers. The response surface predictions revealed the parameter interactions for the resultant fiber diameter, and showed that there is a negative correlation between the mean diameter and coefficient of variation for the fiber diameter. A sub-domain of the parameter space consisting of the solution concentration, applied voltage and collector distance, was suggested for the potential nano-scale fiber production.

Keywords: Nanofiber; Electrospinning; Response Surface Methodology

Introduction

Nanomaterials have become a research priority as biotechnology, defense and semiconductor industries in particular, are interested in potential applications of nanotechnology. Specifically, a substantial amount of research on nano-scale fibers is being conducted to meet the demands of their prospective application areas such as tissue engineering [1, 2], membranes [3], nano resonators [4], micro air vehicles [5], and hydrophobic thin films [6].

Electrospinning (also called electrostatic fiber spinning) has been one of the promising processes to produce continuous nano-scale fibers from both synthetic and natural polymers. Electric forces are used to form fibers from material solutions or melts in the electrospinning process. Studies on electrically driven liquid jets were

initially started in 19th century, and electrospinning of polymer fibers was first patented by Formhals in 1934 [7]. The main principle in electrospinning as defined by Doshi and Reneker is to generate a charged jet of polymeric solution by applying an electric field [8, 9]. As the jet travels in the air, the solvent evaporates and a charged fiber is left behind which can be collected on a grounded plate (collector). Through this process, mostly mats of randomly oriented fibers with large surface to volume ratio as well as various fiber morphologies and geometries are fabricated from various polymer solutions, as noted in Deitzel et al. [10]. Theoretical simulation of the process, fiber formation mechanism, parameters influencing the fiber dimension and morphology have been under extensive investigation for the last decade [8, 10-18]. Up-to-date achievements in fiber production via electrospinning were well summarized by Dzenis [19]. He highlighted, for instance, highly aligned fibers and their assemblies made possible by understanding and controlling the bending instabilities. He also addressed new challenges such as analysis of the effects of solvent evaporation that may help to develop robust methods for manufacturing extremely small nanofibers.

The resultant fiber diameter determines properties of the electrospun fiber mats such as mechanical, electrical, and optical properties. It was previously shown that both the strength and the conductivity of the film/mat of fibers produced by electrospinning are sensitive to fiber diameter [20, 21]. Moreover, size of the fibers along with morphology influences the hydrophobic behavior of polymers. Açıatay et al. [6] illustrated the effect of morphology of the electrospun mat of crosslinked polyacrylonitrile (PAN) fibers on the resultant hydrophobic behavior. They observed three different morphologies: beads only, beads-on-fibers and fibers only. Following their work, Şimşek et al. [22] concluded that water contact angles (hydrophobic surface) are affected by the size of fibers. Filtering application is also affected by the fiber size [23, 24]. Therefore, it is important to have control over the fiber diameter which is a function of material and process parameters. Despite relatively early introduction of the electrospinning process, the effects of the process and material parameters on the fiber formation are still under investigation theoretically and experimentally. Fridrikh et al. [14] derived an expression for the diameter of the jet, generated as a function of material properties such as conductivity, dielectric permittivity, dynamic viscosity, surface tension, and density; as well as process characteristics (e.g. flow rate, applied electric field, and electric current). Their predictions correlated very well with the experimental results for polyethyleneoxide (PEO) and moderately with the results for

PAN. Sukigara et al. [17] have reported an experimental work via response surface methodology (RSM), and shown that the effect of the applied voltage creating the electric field may be surprisingly small or expectedly significant depending on the solution concentration in electrospinning of Bombyx Mori silk. Their work sets a good example of the possible interactions between the parameters of the process that may also be expected for other polymers. Gu et al. [25] who also employed RSM, reported no significant effect of voltage on the processing of commercially available PAN for nanofibers. Their experiments, however, were at a constant collector distance whose possible interaction with the other parameters may not have surfaced in their results.

The objective of this study was to investigate the electrospinning related material and process parameters, solution concentration, applied voltage and collector distance, and their individual and interactive effects on the PAN fiber diameter. Another aim was to predict the domain of the parameters where targeted PAN fiber diameter can be achieved. In this experiment-oriented work, PAN polymer solution was electrospun to produce nano-scale fibers, and emphasis was given to the effect of polymer solution concentration, applied voltage, and the collector distance. Their effects were investigated within the context of Response Surface Methodology (RSM) that incorporates Design of Experiments (DOE) and linear regression [26-28]. This approach enables experimental investigation of the individual factors and the interactions of the factors (variables or parameters) simultaneously [13, 17, 25] as opposed to one factor at-a-time approach [10, 29-31]. A surrogate model of fiber diameter that is a response surface approximation was constructed. Such an empirical model allows the evaluation of significance of the parameters based on experimental results for the fiber diameter and provides prediction capability for the process domain of targeted fiber diameter.

Experimental Procedure

Description of “experiment” for the present work

In this experiment-oriented study an “experiment” has the following set of actions: i) polymer preparation, ii) electrospinning of the polymer, and iii) Scanning Electron Microscopy (SEM) imaging of the collected mat of fibers and image processing to determine fiber diameter statistics. The experiment parameters or variables are considered as material related variables (e.g., molecular weight and

solution concentration) and process related variables (e.g., applied voltage and collector distance) and the result of the experiment is the electrospun fiber diameter.

i) Nano-scale fiber material: Preparation of PAN-DMF Polymer Solution

Polyacrylonitrile was the polymer of interest in this work. It was synthesized by solution polymerization at Sabancı University Polymer Synthesis Laboratory. The acrylonitrile (AN, Merck) was used after purification by double distillation over CaH_2 under nitrogen. N,N-Dimethylformamide (DMF, Labscan) and azo-bis-isobutyronitrile (AIBN, Fluka) were used as received. Molecular weight of PAN was adjusted by changing AIBN concentration and fixing the amount of AN concentration. The syntheses of the two polymers having different molecular weights labeled as high (HMW) and low (LMW) are summarized in

Table 1. Reported viscosity average molecular weights were measured with Ubbelohde Viscometer, by preparing solutions in DMF at 25°C and calculated by the Mark-Houwink Equation with K' and a constants 0.052 and 0.690, respectively [32].

After fixing the molecular weight of the PAN as described in

Table 1, the polymer was dissolved in DMF and stirring for 24 hours. As a result, homogenous HMW PAN-DMF and LMW PAN-DMF solutions in different concentrations ranging between 8–16% (w/w- weight-by-weight basis) were prepared.

ii) Nano-scale fiber production by Electrospinning: Process Description

Polymer fibers of nano and sub-micron scale were manufactured by electrospinning process, the setup for which is schematically represented in Figure 1. The polymer solution was placed into a syringe/capillary tube connected to a high voltage source. An electric field is formed between the grounded collector and the tip of the syringe/capillary tube (1.13mm in diameter). A syringe pump (Univentor 801 Syringe Pump) was utilized to form a constant amount of solution on the tip. The resultant electrostatic forces cause the ejection of the polymer solution to air forming a jet. As the polymer solution jet travels in the air, the solvent evaporates, and the polymer is collected on the grounded conductive target as fine fibers [8]. This stationary collection procedure results in non-woven fiber mats as seen in Figure 1.

iii) Measurements: Dimensional characterization of non-woven fiber mats

Primary focus was on the effects of material and process parameters on the fiber diameter and its statistics over each non-woven fiber mat. After formation the non-woven mat of fibers on the aluminum collector, several images from each mat sample were taken by SEM (LEO 1530VP). Images taken relatively apart from each other were

considered, and diameter measurements of about a total of 50 fibers, each with multiple sampling, were carried out. An image processing software (MediaCybernetics, Image Pro Plus 5.1) is used to make the measurements. This sampling scheme was to catch the scattering of the fiber dimensional characteristics over the whole non-woven fiber mat. It enabled the determination of statistics for fiber diameter, (mean, standard deviation and distribution) on each SEM sample image. A typical distribution of measured fiber diameters is shown in Figure 2.

Planning and analysis of experiments: Response Surface Methodology

Investigation of the electrospinning process and its effects on the PAN fiber diameter requires a number of experiments described in the previous section. The planning and analysis of these experiments were performed within the context of Response Surface methodology. Response surfaces (RS) are in fact used to approximate numerical or physical experimental data by an expression that is usually a low-order polynomial. The three key steps of the methodology as noted in [27] are the following:

Design of experiments

Parameter or factor settings at which the experiments are conducted were pre-selected. The selection represents the design/parameter space so that the experiments will yield adequate and reliable measurements/calculations of the response of interest. Two-level and three-level factorial experimental designs were used in this study for four and two variable/parameter cases, respectively, as described in the following sections.

Regression analysis

A mathematical approximation model was determined, which was fit to the data that was generated from the set of experiment points of the previous step. The fundamentals for the least squares fitting procedure can be found in number of sources [27], but are also briefly introduced here as an appendix. The regression analysis was performed using a statistical software JMP IN 5.1 by SAS Institute. The software also conducts appropriate statistical test of hypotheses (see appendix) concerning the parameters in the mathematical model that is the RS approximation.

Prediction of experiment settings for specified response

The response was predicted at a given set of the experimental factors/variables by using the RS approximation. The specific settings or domain of the factors/parameters that produce extremums (maximum or minimum) or targeted value of the response can be determined. This can be easily achieved by graphical means in one-variable and two-variable cases. For higher dimensional problems, numerical optimization techniques are usually applied.

Screening for significant parameters in electrospinning of polymer fibers

A preliminary screening study was first carried out in order to rank the significance of four major parameters on the resultant mean diameter of the polymer fibers collected by electrospinning. The total of four parameters consists of two material and two process related factors: molecular weight and solution concentration of the polymer, and applied DC voltage and the collector distance, respectively. The selected experimental design was two-level factorial experimental design and provided 16 experiment settings for 4 variables. The experiment settings were the vertices of a four-dimensional cuboidal region formed by the combinations of lower and upper limits of each parameter, as summarized in Table 2.

Experimental procedure described in the previous section was applied at each of the 16 settings, $(x_1^L, x_2^L, x_3^L, x_4^L)$, $(x_1^L, x_2^L, x_3^L, x_4^U)$, $(x_1^L, x_2^L, x_3^U, x_4^L)$, ..., $(x_1^U, x_2^U, x_3^U, x_4^U)$. Following the fiber production, statistics of the fiber diameter sampled on SEM images from each non-woven mat were computed. Among the mats of the 16 settings sampled, the minimum fiber diameter was observed at the parameter settings of $(x_1^L, x_2^U, x_3^U, x_4^L)$ as $0.434 \pm 0.188 \mu\text{m}$ and the maximum was at $(x_1^U, x_2^L, x_3^U, x_4^U)$ as $2.946 \pm 1,320 \mu\text{m}$.

Next, regression analysis was performed to fit the observed response y , the mean fiber diameter. The true, but unknown relation between the mean fiber diameter and the parameters $\eta = f(x_1, x_2, x_3, x_4)$ is approximated by a first-order polynomial model in four variables and denoted as \hat{y} ,

$$\hat{y} = b_0 + b_1x_1 + b_2x_2 + b_3x_3 + b_4x_4 \quad (1)$$

The unknown coefficients in Eq. (1) were found by JMP IN, which employs the least squares method described in the appendix.

Table 3 presents the summary of the statistics from the data and first-order polynomial model. The second column reports the estimates of the coefficients in Eq. (1). Measure of goodness of the fit, R^2 , is about 0.9, which is a statistical indication that the variation in the fiber diameter is explained reasonably well by the model in Eq. (1).

The other reported statistics, p -values associated with the coefficient estimates are statistical measures of significance of the individual parameters in explaining the variability of the fiber diameter over the cuboidal domain. The lower the p -value, the more significant the parameter is.

The p -values of the parameter estimates are below the significance level of 0.05¹; therefore,

Table 3 suggests that molecular weight x_1 and applied voltage x_3 are significant factors for the variation of the fiber diameter. For the other two factors, solution concentration and the collector distance, there is no strong statistical evidence that the coefficients are different than zero as the p -values are substantially high.

The significance of the molecular weight and voltage is not surprising [13, 15, 29]. Other variables, however, were also expected to play a role in fiber formation as demonstrated by Demir et al. [18] for polyurethane fibers, and by Sukigara et al. [17] for Bombyx silk fibers of fixed molecular weight. The varied molecular weight, however, seems to be a dominant factor and explains most of the variation around the mean of the 16 measured mean-fiber diameters, \bar{y} in the studied ranges of Table 2. Dominancy of the molecular weight was expected because it is the molecular weight which affects the entanglement of the polymer chains and it is the stretching of the polymer solution that preserves a continuous solution jet to form fibers [33].

¹ P -value below 0.05 means that the probability of being wrong in accepting that b_1 and b_3 coefficients are different than zero will be less than 5%. This shows x_1 and x_3 as the significant factors.

Note that the first-order model was not intended to predict the fiber diameter within the four dimensional cuboidal domain. This is firstly because of the fact that the given domain where the model is valid does not seem to provide nano-scale fiber diameter contrary to the objective of this study. And secondly, higher order model is usually necessary to make more precise predictions; therefore, additional experiments at other levels of parameters are also required.

Prediction of domain of experimental settings for nano-scale fibers

The screening experiments demonstrated that fiber diameter in the selected range of the parameters is mostly in micron scale. Extending the ranges of the parameters was expected to help achieve the goal of nano-scale fiber production. Because of its dominant effect, the adjustment of molecular weight only, was expected to allow reduced fiber diameters. It was fixed, however, at its original lower limit for further investigation here, because fixing the molecular weight of PAN was expected to surface the effect of the other parameters, x_2 , x_3 and x_4 and possibly to provide finer tuning for the resultant fiber diameter.

Among the remaining three variables, three different collector distances, x_4 were considered, at 8, 12 and 16 cm. At each collector distance, experiments in x_2 and x_3 domain (solution concentration and applied voltage, respectively) were carried out. Thirteen experiments of 2-D evaluations at each collector distance are shown schematically in Figure 3. Nine of them marked by filled circles are the experimental settings defined by standard two-variable Face-centered Central Composite Design (FCCD). The other four marked by squares are to provide additional levels for the variables. The experimental settings are summarized in Table 4. Note that the lower limits for the variables were lowered compared to the limits reported in Table 2.

Results from Response Surface for mean fiber diameter

The data of 13 experiments represented in Figure 3a were obtained by following the experimental procedure described in Section 2. At each collector distance, a total of 13 experiments, including 5 levels of both parameters, allow to fit a cubic RS model as a function of solution concentration and applied voltage, at fixed molecular weight,

$$\hat{y} = b_0 + b_1x_2 + b_2x_3 + b_3x_2^2 + b_4x_2x_3 + b_5x_3^2 + b_6x_2^3 + b_7x_2^2x_3 + b_8x_2x_3^2 + b_9x_3^3 \quad (2)$$

Response surfaces of the mean fiber diameter fitted to data of each collector distance are summarized in Table 5. The R^2 values, roughly around 0.98, illustrate that the models are able to explain 98% of the variability in the mean fiber diameter over the two-variable domain, at each collector distance. Furthermore, the p -values of concentration related terms in Eq. (2) suggest now the concentration, as well as the voltage, is a significant parameter as expected.

In addition to the statistical results, goodness of the cubic RS models can be graphically represented by the predicted versus the actual diameter plots, as illustrated in Figure 4.

Relying on the goodness of the fit, mean fiber diameter was predicted on a 21x21 grid of the concentration versus voltage domain. For each collector distance associated cubic RS presented in Table 5 was utilized to prepare contour plots of the predicted mean fiber diameter as illustrated in Figure 5. Each contour visualizes the effects of concentration and voltage at the corresponding collector distance. In addition, comparison of the three contour plots shows the effect of the collector distance.

The contour plots indicate that the resultant fiber diameter is very responsive to the changes in concentration as expected and previously mentioned in several other studies [13, 17, 21, 25, 30, 34, 35]. It is also responsive to changes in voltage, but its effect depends on the level of solution concentration and collector distance. Similar outcomes consistent with our results were reported by Baumgarten [29] and Fenessey [36] for PAN; and Sukigara [17] for Bombyx silk fibers. However, these contradict with the observations by Gu et al [25]. In their experiments, diameter of the fibers did not change as they altered the voltage, at the collector distance where all of their experiments were carried out. This contradiction is attributed to the fact that the extent of the interaction of any two variables may depend on the third, as observed in this study. As we adjusted the collector distance, the contribution of voltage in fiber diameter formation was observed. For instance, at collector distance of 8 cm (Figure 5a), fiber diameter is more sensitive to the changes in voltage up to 14% solution concentration, and its effect becomes negligible as level of concentration increases up to 16%. Moreover, at 12cm and 16cm collector distances (Figure 5b and 5c), contour plots suggest that voltage has almost no and very little effect on fiber diameter formation,

respectively. Therefore, voltage is a factor for fiber diameter, but at a different level of significance depending on the concentration and collector distance.

Results from Response Surface for coefficient of variation of fiber diameter

Recall that the measurement procedure uses SEM images over locations remote from each other on a non-woven mat of fibers. The image processing revealed that fibers produced at a given parameter settings exhibit scatter of the fiber diameter and the amount of scatter may also vary as a function of the parameters within the domain. For instance, at experimental condition of $x_2 = 8\%$, $x_3 = 10$ kV coefficient of variation (CV = standard deviation normalized with the experiment's mean fiber diameter) was $CV = 0.609$, while at experimental condition of $x_2 = 14\%$, $x_3 = 25$ kV, was $CV = 0.362$. The distributions of the fiber diameter normalized by the mean value at these settings are shown in Figure 6. Based on the data collected at 13 experiments carried out on each collector distance, prediction of the scatter dependence on parameters was also investigated. Coefficient of variation at each experiment was first computed by normalizing the standard deviation with the experiment's mean fiber diameter. Then cubic RS model of Eq. (2) was fit to the coefficient of variation data of 13 experiments at each collector distance. The accuracy of the RS approximations is reasonable with R^2 values of about 0.93. Contours of the coefficient of variation (CV) were also plotted as shown in Figure 7. Contour plots of the mean fiber diameter and the CV together provide information on the correlation between the scatter and the fiber diameter. It appears that there is a negative correlation between the mean fiber diameter and the relative scatter (CV), that is the lower the mean fiber diameter, the higher is the scatter around it. This appears to be contradictory with the results by Gu et al. [25]. The major reason of this contradiction is attributed to the fact that the polymers synthesized differently, which yield polymers with different molecular weights. Difference in the molecular weight of these polymers exhibit a variation in the chain entanglement of the two polymers. Chain entanglements have a significant impact on the electrospinning process, deciding whether the jet breaks up into droplets, beads, or fibers, and they affect the geometry of these formations.

Coefficient of correlation based on the 21x21 grid predictions is about -0.89. As for the CV dependence on the parameters, the plots suggest that scattering increases at low concentrations and it becomes less as the concentration increases. In addition to

this, scattering is affected by both concentration and voltage at lower edges and voltage has less effect in high concentration edge. Furthermore, three contour plots conjointly suggest that scattering is also affected by variations in the collector distance.

Parameter space narrowed down by RS for nano-scale PAN fiber production

At 8 cm collector distance, the mean fiber diameter predictions on the solution concentration of 8% at low voltage values are negative. This is attributed to RMSE being about 0.150, which is substantially high compared to low fiber diameter regions. The RMSE is, in fact, quite reasonable considering the fact that least squares procedure provides a global approximation over a range from nano-scale to micro-scale, and it is about 15% of the mean of the whole domain. This is an indication that the cubic RS constructed in this domain is not sufficient to make precise predictions for the nano-scale fibers. It is quite useful, however to determine potential regions/windows of parameter domain in production of nano-scale fibers. Such a windowing may be further investigated for finer predictions of nano-scale ranges. Overall, it was observed that mean fiber diameter decreases with concentration. As the concentration is decreased as does the viscosity. As the number of solvent molecules increase, the lesser amount of polymer chains make the surface tension dominate the electrospun jet that results in thinner fibers or bead formation along the fibers [33]. Yet, as the concentration increases charges on the electrospinning jet will be able to stretch the polymer solution; thus, the polymer chain; hence, thicker fibers are formed. The contour plots further suggest the possible concentration and voltage ranges as 8–10% and 10–20 kV, respectively, for nano-scale fiber production. It is also observed that as collector distance is increased, nano-scale fiber formation range also increases.

Concluding Remarks

An experimental investigation of electrospinning process and material parameters to produce PAN fibers was carried out. The goal was to investigate the interactive effects of the parameters on the resultant fiber and to establish a prediction scheme for the domain/window of the parameters where targeted PAN fiber diameter can be achieved. The planning of the experiments, the analyses of the results and the predictions were performed within the context of Response Surface Methodology featuring Design of Experiments and linear regression analysis.

Sets of experiments were performed at three collector distances each allowing evaluation of solution concentration and applied voltage two-variable domain associated with the collector distances. Contour plots of mean and coefficient of variation of the formed fiber diameter, on the solution concentration and applied voltage parameter domain, were created by the cubic polynomial response surface models. The predictions of the empirical models and contour plots suggest the following conclusions in electrospinning of Polyacrylonitrile/DMF system studied here:

Applied voltage was found to be an insignificant factor when the concentration level was high. That is, control of fiber diameter in micrometer scale may be provided by concentration alone. However, voltage was found to be an eminent parameter, depending on the concentration and collector distance levels, and this observation demonstrates the interactive effects of the parameters.

Collector distance, as well as both voltage and concentration were found to be significant in nano-scale fiber production. The collector distance may be increased in favor of reducing the fiber diameter.

The fiber diameter and the coefficient of variation are negatively correlated. Scatter of the diameter of nano-scale fiber mats is predicted to be high

The domain of potential nano-scale fiber was predicted to be in low concentration and voltage ranges (8-10% and 10-20kV, respectively, for PAN/DMF with molecular weight of about 75,000 g/mol due to Mark-Houwink Equation).

Acknowledgement

The authors would like to thank Eren Simsek from Sabanci University, for his contributions in arranging the electrospinning set up.

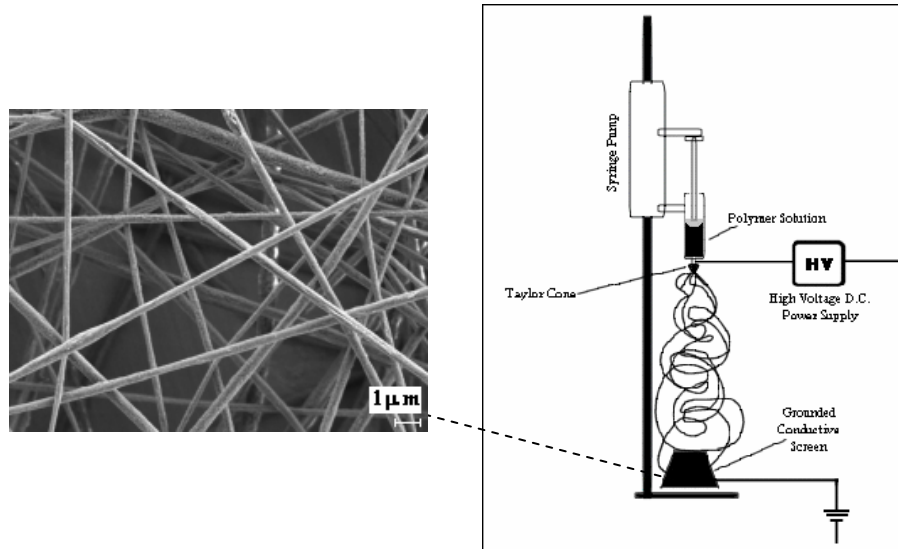


Figure 1 Electrospinning setup and its product: non-woven fiber mat

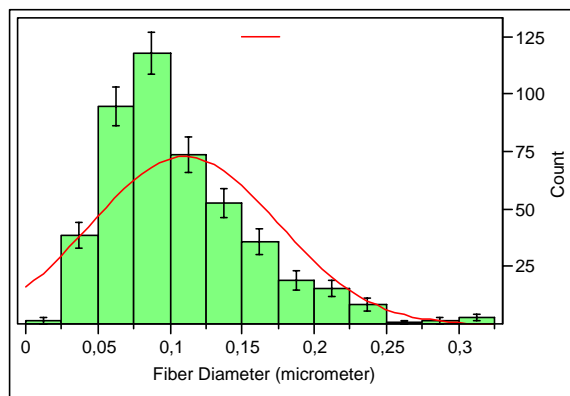


Figure 2 Fiber diameter distribution for HMW, 8% solution concentration, 20kV voltage and 8 cm collector distance

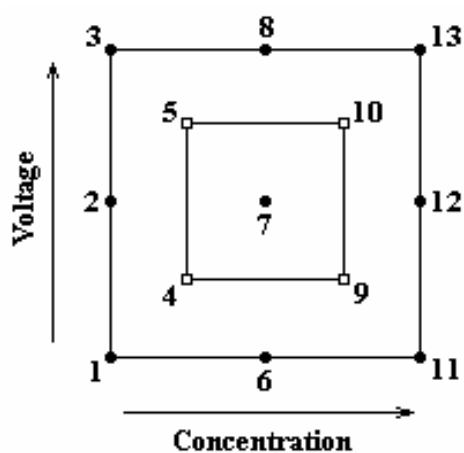
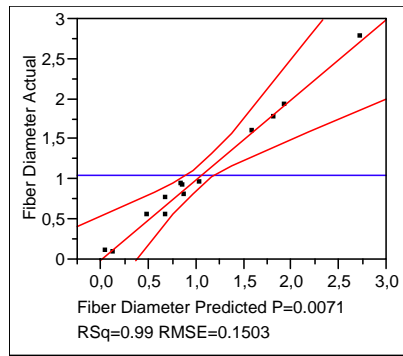
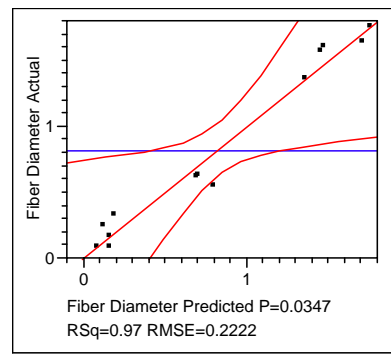


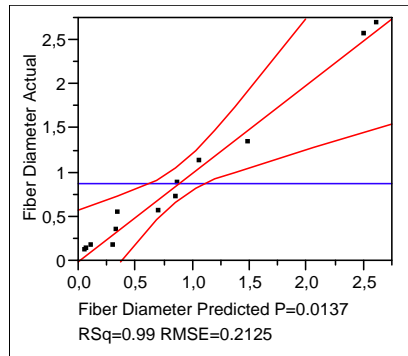
Figure 3 Design of experiments of two-variables, solution concentration x_2 and applied voltage x_3 , at fixed collector distances x_4



(a)

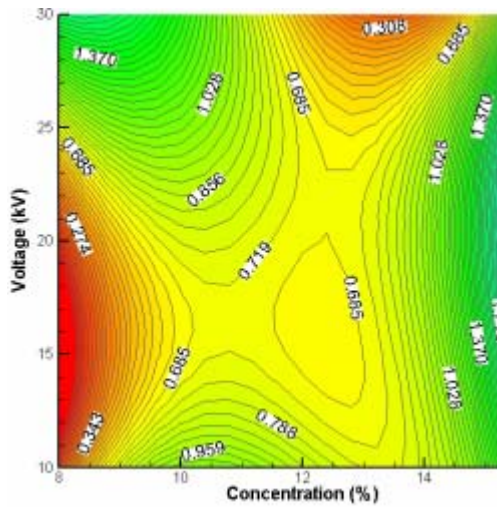


(b)

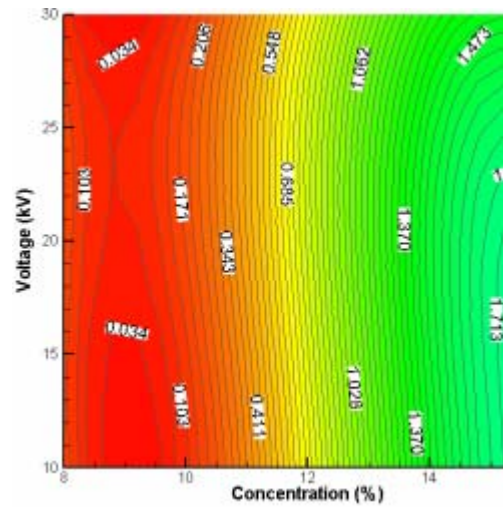


(c)

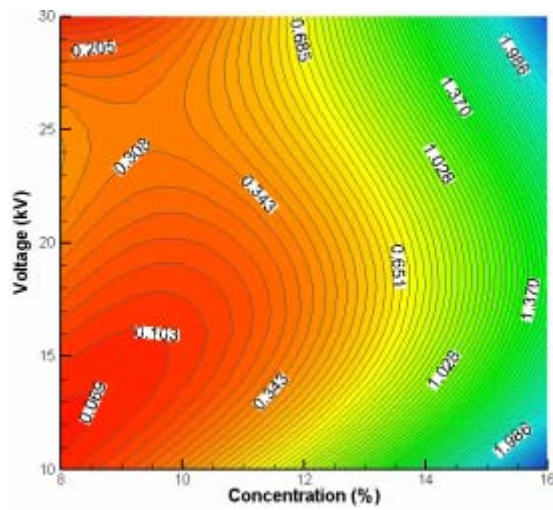
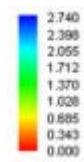
Figure 4 Predicted versus Actual Mean Fiber Diameter Plots (a) 8cm collector distance (b) 12cm collector distance (c) 16cm collector distance



(a)

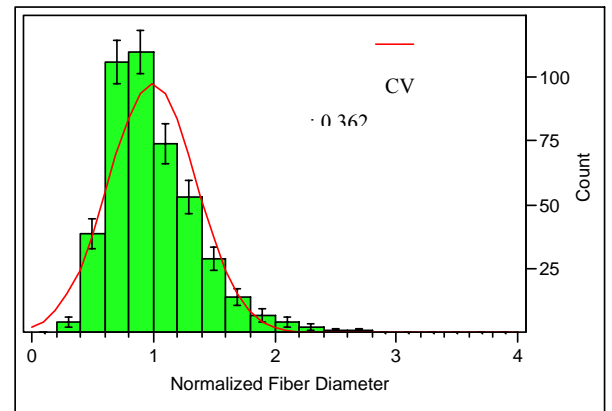
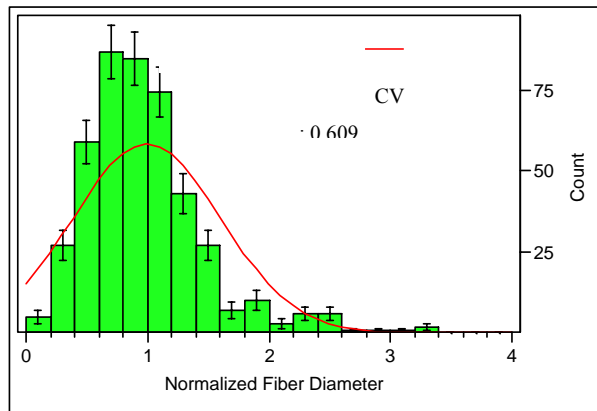
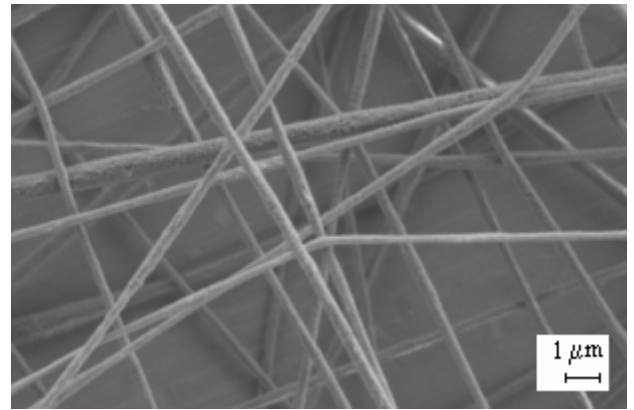
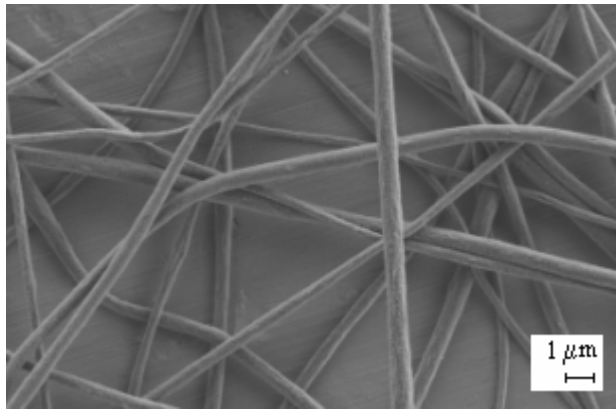


(b)



(c)

Figure 5 Mean fiber diameter contour plots by predictions using RS approximations summarized in Table 5, (a) 8cm collector distance (b) 12cm collector distance (c) 16cm collector distance



Process Conditions: 8% - 10kV

Process Conditions: 14% - 25kV

Figure 6 Scatter of diameter of fibers and its dependence on the process and material parameters (e.g. at collector distance 8 cm)

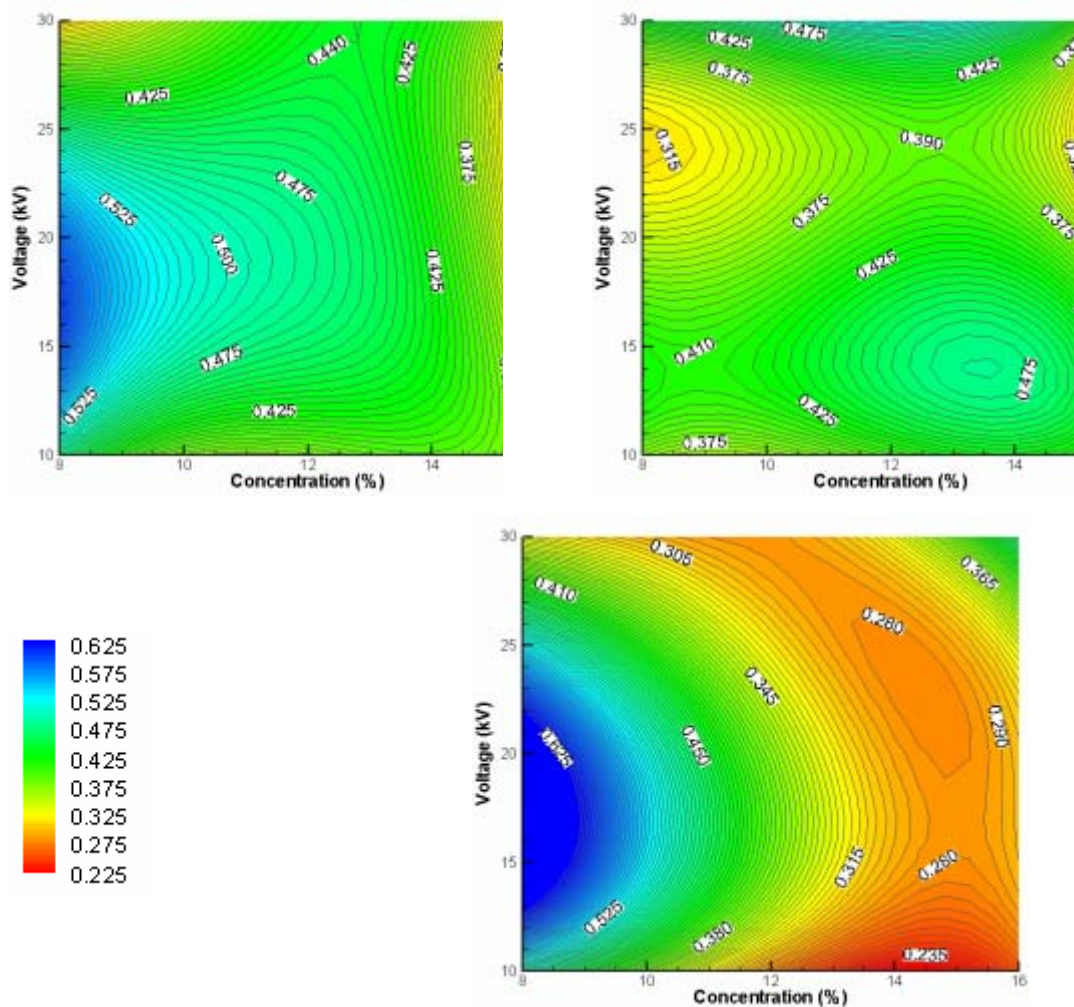


Figure 7 Contour plots for coefficient of variation by predictions using cubic RS approximations, (a) 8cm collector distance (b) 12cm collector distance (c) 16cm collector distance

Table 1 Synthesis of PAN, and viscosity average molecular weight of each sample

S	Amount of			MW _v (g)
	AN (g)	AIBN	DMF	
H	10	0.0019	20	121000
L	10	0.0087	20	73400

Table 2 Material and process parameters for significance screening and upper and lower limits used in the two-level factorial experimental design

Variable	Variable	Lower	Upper
x_1	Molecular	73,400	121,000
x_2	Solution	12	16
x_3	Applied Voltage	12	16
x_4	Collector	12	16

Table 3 Statistics of first order polynomial approximation Eq. (1), fit to mean fiber diameter data after screening tests for four parameters

Term	Estimate	Prob	Summary of Fit	
Intercept, b0	-	0.016	Mean,	1.388
Molecular	$3.13 \times 10^{-}$	<	RMSE	0.311
Concentration,	-	0.451	R ²	0.899
Voltage, b3	$9.20 \times 10^{-}$	0.038		
Distance, b4	$2.34 \times 10^{-}$	0.560		

² Computed HMW and LMW values for the polymer synthesis summarized in

Table 1

Table 4 Experiments at each collector distance, in the extended two-variable, solution concentration and applied voltage domain (The molecular weight is fixed, $x_1=73413$)

Experiment	Collector Distance, x_d : 8, 12, 16 cm	
	Solution Concentration,	Applied Voltage,
1	8	8
2	8	12
3	8	16
4	10	10
5	10	14
6	12	8
7	12	12
8	12	16
9	14	10
10	14	14
11	16	8
12	16	12
13	16	16

Table 5 Parameter estimates and the statistical results of each cubic RS approximation at three different collector distances³

Collector Distance: 8 cm				
Term	Estimate	p-value	Summary of Fit	
Intercept,	-32.69	0.011	Mean	1.059
x_2, b_1	9.94	0.007	RMSE	0.150
x_3, b_2	-0.74	0.086	R ²	0.990
x_2^2, b_3	-0.86	0.007		
x_2x_3, b_4	-0.01	0.834		
x_3^2, b_5	0.04	0.061		
x_2^3, b_6	0.02	0.007		
$x_2^2 * x_3, b_7$	0.003	0.028		
$x_2 * x_3^2, b_8$	-0.002	0.008		
x_3^3, b_9	-0.0003	0.0297		
Collector Distance: 12 cm				
Term	Estimate	p-value	Summary of Fit	
Intercept,	19.53	0.107	Mean	0.820
x_2, b_1	-5.11	0.107	RMSE	0.222
x_3, b_2	-0.19	0.693	R ²	0.972
x_2^2, b_3	0.43	0.110		
x_2x_3, b_4	0.02	0.565		
x_3^2, b_5	0.01	0.843		
x_2^3, b_6	-0.01	0.121		
$x_2^2 * x_3, b_7$	-0.001	0.565		
$x_2 * x_3^2, b_8$	-0.0001	0.781		
x_3^3, b_9	-0.0001	0.864		
Collector Distance: 16 cm				
Term	Estimate	p-value	Summary of Fit	
Intercept,	-1.55	0.862	Mean	0.874
x_2, b_1	0.20	0.931	RMSE	0.213
x_3, b_2	0.25	0.582	R ²	0.985
x_2^2, b_3	0.02	0.910		
x_2x_3, b_4	-0.07	0.118		
x_3^2, b_5	0.01	0.772		
x_2^3, b_6	0.0002	0.975		
$x_2^2 * x_3, b_7$	0.0003	0.840		
$x_2 * x_3^2, b_8$	0.002	0.038		
x_3^3, b_9	-0.0004	0.341		

³ x_2 : Solution concentration, x_3 : Applied Voltage

References

1. Li, W.-J., Laurencin C. T., Caterson E. J., Tuan R. S., Ko F. K. 2001. "Electrospun nanofibrous structure: A novel scaffold for tissue engineering," *Journal of Biomedical Materials Research*, 60(4):613-621.
2. Bölgen, N., Menceloglu Y. Z., Acatay K., Vargel I., PisJournal of Biomaterials Science P. E., E. 2005. "In vitro and in vivo degradation of non-woven materials made of poly(ϵ -caprolactone) nanofibers prepared by electrospinning under different conditions.," *Journal of Biomaterials Science, Polymer Edition*, 16(12):1537-1555.
3. Gibson, P. W., Schreuder-Gibson H. L., Rivin D. 1999. "Electrospun fiber mats: Transport properties," *AIChE Journal*, 45(1):190-195.
4. Kameoka, J., Verbridge S. S., Liu H., Czaplewski D. A., Craighead H. G. 2004. "Fabrication of Suspended Silica Glass Nanofibers from Polymeric Materials Using a Scanned Electrospinning Source," *Nano Letters*, 4(11):2105-2108.
5. Pawlowski, K. J., Belvin H. L., Raney D. L., Su J., Harrison J. S., Siochi E. J. 2003. "Electrospinning of a micro-air vehicle wing skin," *Polymer*, 44(1309–1314).
6. Acatay, K., Simsek E., Ow-Yang C., Menceloglu Y. Z. 2004. "Tunable, Superhydrophobically Stable Polymeric Surfaces by Electrospinning," *Angewandte Chemie, International Edition in English*, 43(39):5210.
7. Formhals, A. US Patent, 1975504; 1934.
8. Doshi, J., Reneker D. H. 1995. "Electrospinning Process And Applications Of Electrospun Fibers," *Journal of Electrostatics*, 35(2-3):151.
9. Reneker, D. H., Chun I. 1996. "Nanometre diameter fibres of polymer, produced by electrospinning," *Nanotechnology*, 7(216).
10. Deitzel, J. M., Kleinmeyer J., Harris D., Tan N. C. B. 2001. "The effect of processing variables on the morphology of electrospun nanofibers and textiles," *Polymer*, 42(261).
11. Reneker, D. H., Fong H., Y. A. L., Koombhongse S. 2000. "Bending instability of electrically charged liquid jets of polymer solutions in electrospinning," *Journal of Applied Physics*, 87(4531).
12. Li, D., Xia Y. 2004. "Electrospinning of Nanofibers: Reinventing the Wheel?," *Advanced Materials*, 16(14):1151.
13. Kattamuri, N., Sung C. 2004. "Uniform Polycarbonate Nanofibres Produced By Electrospinning," *Macromolecules*, 3(425).

14. Fridrikh, S. V., Yu J. H., Brenner M. P., Rutledge G. C. 2003. "Controlling the Fiber Diameter during Electrospinning," *Physical Review Letters*, 90(14):1445502-1-1445502-4.
15. Larrondo, L., Manley J. 1981. "Electrostatic Fiber Spinning from Polymer Melts. I. Experimental Observations on Fiber Formation and Properties," *Journal of Polymer Science, Part B: Polymer Physics*, 19(909).
16. Rutledge, G. C., Li Y., Fridrikh S., Warner S. B., Kalayci V. E., Patra P. 2001. *Electrostatic Spinning and Properties of Ultrafine Fibers*. National Textile Center Annual Report, M01, D22.
17. Sukigara, S., Gandhi M., Ayutsede J., Micklus M., Ko F. 2004. "Regeneration of Bombyx Mori silk by electrospinning. Part 2. Process Optimization and empirical modelling using response surface methodology," *Polymer*, 45(3701).
18. Demir, M. M., Yilgor I., Yilgor E., Erman B. 2002. "Electrospinning of Polyurethane fibers," *Polymer*, 43(3303).
19. Dzenis, Y. 2004. "Spinning Continuous Fibers for Nanotechnology," *Science*, 304(1917).
20. Kwon, I. K., Kidoaki S., Matsuda T. 2004. "Electrospun nano- to microfiber fabrics made of biodegradable copolyesters: structural characteristics, mechanical properties and cell adhesion potential," *Biomaterials*, 26(3929).
21. El-Aufy, A. K. 2004. *Nanofibers and nanocomposites of poly(3,4-ethylene dioxythiophene)/poly(styrene sulfonate) by electrospinning*. Drexel University, Philadelphia; <http://dspace.library.drexel.edu/handle/1860/282>, April 2004.
22. Simsek, E., Acatay K., Menceloglu Y. Z. Year. *Effect of perfluoroacrylate ratio on the generation of stable superhydrophobic surfaces displaying low contact angle hysteresis*. *Polymer Preprints* 2005;46(1): 385.
23. Reneker, D. H., Shin C., Chase G. G. 2005. "Recycled expanded polystyrene nanofibers applied in filter media," *Colloids and Surfaces A: Physicochemistry Engineering Aspects*, 262(211).
24. Grafe, T. H., Graham K. M. Year. *Nanofiber Webs from Electrospinning*. *Nonwovens in Filtration - Fifth International Conference 2003*;1.
25. Gu, S. Y., Ren J., Vansco G. J. 2005. "Process optimization and empirical modeling for electrospun polyacrylonitrile (PAN) nanofiber precursor of carbon nanofibers," *European Polymer Journal*, 41(11):2559.

26. Papila, M., Haftka R. T. 2000. "Response Surface Approximations: Noise, Error Repair, and Modelling Errors," *AIAA Journal*, 38(2336).
27. Khuri, A. I., Cornell J. A. 1996. *Response Surfaces: Designs and Analyses*. Marcel Dekker Inc.,
28. Montgomery, M. a. 1997. *Response Surface Methodology*. Wiley,
29. Baumgarten, P. K. 1971. "Electrostatic Spinning of Acrylic Fibers," *Journal of Colloid and Interface Science*, 36(1):71.
30. Mo, X. M., Xu C. Y., Kotaki M., Ramakrishna S. 2004. "Electrospun P(LLA-CL) nanofiber: a biomimetic extracellular matrix for smooth muscle cell and endothelial cell proliferation," *Biomaterials*, 25(1883).
31. Katti, D. S., Robinson K. W., Ko F. K., Laurencin C. T. 2004. "Bioresorbable nanofiber-based systems for wound healing and drug delivery: Optimization of fabrication parameters," *Journal of Biomedical Materials Research Part B: Applied Biomaterials*, 70B(2):286-296.
32. Brandrup, J., Immergut E. H., Grulke E. A. 1999. *Polymer Handbook*. Wiley,
33. Ramakrishna, S., Kujihara K., Teo W.-E., Lim T.-C., Ma Z. 2005. *An introduction to electrospinning and nanofibers*. World Scientific Publishing Co. Pte. Ltd.,
34. Matthews, J. A., Wnek G. E., Simpson D. G., Bowlin G. L. 2003. "Electrospinning of Collagen Nanofibers," *Biomacromolecules*, 3(2):232.
35. Ryu, Y. J., Kim H. Y., Lee K. H., Park H. C., Lee D. R. 2003. "Transport properties of electrospun nylon 6 nonwoven mats," *European Polymer Journal*, 39(1883).
36. Fennessey, S. F., Farris R. J. 2004. "Fabrication of aligned and molecularly oriented electrospun polyacrylonitrile nanofibers and the mechanical behavior of their twisted yarns," *Polymer*, 45(4217).